J. Indian Inst. Sci., Mar.–Apr. 1992, **72**, 139–215.

IISc THESES ABSTRACTS

Thesis Abstract (Ph.D.)

A dynamical system that mimics shear flow turbulence by Ganapati S. Bhat.
Research supervisors: R. Narasimha and V. H. Arakeri.
Department: Aerospace Engineering.

1. Introduction

Recent developments in the theory of dynamical systems exhibiting chaotic behaviour (*e.g.*, ref. 1) have raised the question whether turbulence in fluid flows could be understood as dynamical chaos. Several proposals on routes to chaos have been made[2–4], and these have found some support from observations in bounded flows such as convection in a box[5] or Taylor-Couette flow[6]. However, the existence of any connection between the 'dynamical chaos' exhibited by such systems and turbulence in open flows like boundary layers has often been questioned[7,8]. It is generally felt that the chaotic phenomena observed in low-dimensional nonlinear systems may, at best, be relevant to 'weak' turbulence, *i.e.*, to stages preceding onset of fully turbulent behaviour[4]. There are three basic issues that need to be addressed[9].

(i) Chaotic dynamical systems do not exhibit a strong cascade process of the kind generally considered an essential feature of flow turbulence, where energy put in at low wave numbers produces strong fluctuations at high wave numbers[10].

(ii) In fluid flows, especially those that are open (*e.g.*, boundary layers), the critical value of a control parameter like the Reynolds number at onset of turbulence is not unique and depends strongly on environmental disturbance levels[11]. However, in dynamical systems considered to date to model flow turbulence, the role of external noise is not explicitly considered.

(iii) Though chaos has been observed in most dynamical systems in some range of the control parameter, chaos eventually vanishes in almost all systems as the control parameter increases further, while turbulence invariably persists in the flow after its onset.

The work is an attempt to answer the above criticism; it is shown that a simple dynamical system can be constructed with properties that can provide considerable insight into what happens in more complex fluid-flow situations.

2. Model

The idea underlying the present model is to treat turbulent flow as interaction between motions at different scales: the emphasis is not on any particular flow as such but rather on general physical arguments valid for a wide class of flows. For this purpose, we divide the wave number space into two regions, one where nonlinearity and external disturbances play the major role, representing the so-called large scale or large eddy motion and the other where the viscous dissipation is dominant, representing small or Kolmogorov-scale motion. These two scales are coupled by a nonlinear energy-transfer mechanism, often called the cascade process (Fig. 1).

The model has two independent variables U, u both considered functions only of time t, and a specified external forcing $q(t)$. U and u may be thought of as representing the amplitudes of large and small eddy motions, respectively, the actual velocity being a combination like

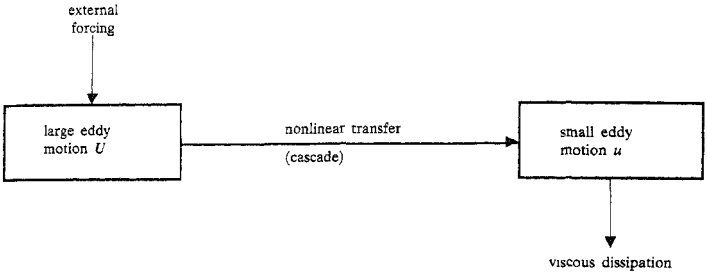

FIG 1. Schematic diagram of energy processes.

$$a\ U(t)\ \exp\ i\omega_1 t + b\ u(t)\ \exp\ i(\omega_2 t + \phi), \tag{1}$$

where ω_1, ω_2 are characteristic large and small eddy frequencies and a and b are weighting functions that are a measure of the bandwidth covered by the respective motions in frequency space.

The importance of including a forcing term $q(t)$ is evident from experimental data on boundary layers[8] It is our premise here that in boundary layers certainly, and possibly in most open flows, there is no transition if there is no forcing: the flow is seen as a (somewhat peculiar) driven nonlinear oscillator.

Here model equations are reproduced below and the considerations that have led to the model are described elsewhere[12]. The model consists of two coupled nonlinear ordinary differential equations subject to a forcing as given below:

$$dU/dt = U(1-\nu-U^2) - K\ u\ |\ u\ | + q(t) \tag{2}$$

$$du/dt = k\ U\ (\ |\ u\ | + \sigma) - \vartheta u \tag{3}$$

with the forcing term to be the sum

$$q(t) = \bar{q}\ \cos\ \omega t + q_n\ \zeta\ (t) \tag{4}$$

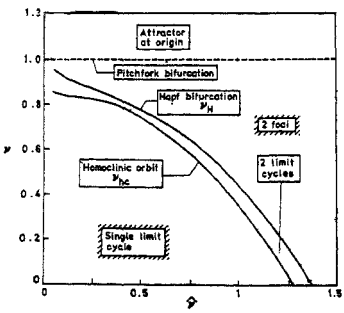

FIG 2. Attractors in the unforced system at $k=K=2{\cdot}3$.

where $\bar{q}$ is the amplitude of a periodic component at frequency ω and ζ (t) is a stochastic term with zero mean and unit mean square.

In (2), ν is a parameter that represents the effect of viscosity on the large-scale motion and $\nu \rightarrow > 0$ is like Reynolds number tending to infinity in a flow. K and k are nonlinear interaction coefficients, $\hat{\nu}$ is the viscous term at the small scale and since dissipation is dominant at these scales, $\hat{\nu} = 0(1)$ is assumed. The ensure that the small eddy variable u will always be excited in the presence of large eddy motion, a small multiple of U is included in (3) through the parameter σ. The forcing (4) permits us to mimic experimental studies undertaken to elucidate the mechanism underlying transition, where free-stream turbulence and other stochastic disturbances have often been reduced and artificial periodic forcing introduced.

3. Nature of solutions

Apart from the forcing, the model has five unspecified parameters. For simplicity it is assumed that $K = k = 2{\cdot}3$ and $\sigma = 0{\cdot}05$. The choice of the parameter $\hat{\nu}$ will follow from a study of the unforced system and the requirement that as ν tends to zero, the forcing amplitude required to induce chaos also goes to zero.

The unforced system has three fixed points (*i.e.*, steady solutions) of which the origin (*i.e.*, $U = 0 = u$) is a saddle node (has real eigenvalues). Figure 2 shows the bifurcations and attractors in the unforced system in $\nu - \hat{\nu}$ plane. Of particular interest is the homoclinic orbit (an orbit that connects a saddle point to itself), and $\hat{\nu}$ is so chosen that at ν is so chosen that at $\nu = 0$ a homoclinic orbit results in the unforced system. This gives $\hat{\nu} = 1{\cdot}27956$ and with this choice all parameters, except ν and q(t), are fixed.

It can be shown using the Melnikov method[1] that for small values of ν ($<<1$), the model indeed possesses chaotic solutions under a periodic forcing. Using the positive Lyapunov characteristic exponent (LCE) as an indicator of chaotic behaviour[13], the region in the $\bar{q}-\nu$ plane where chaotic solutions are present under a periodic forcing is shown in Fig. 3. It is seen that there is a value of ν above which chaotic solutions are not possible, and also that as $\nu \rightarrow 0$ the amplitude of the forcing needed for chaotic behaviour tends to zero.

Time series at parameter values marked in Fig. 3 are shown in Fig. 4. It is seen that within the chaotic region, time series appears to be nonrepeating.

4. Routes to chaos

One of the main reasons for constructing the model was the hope that this model may have some properties common with actual flow turbulence, in particular with the process of transition to turbulence.

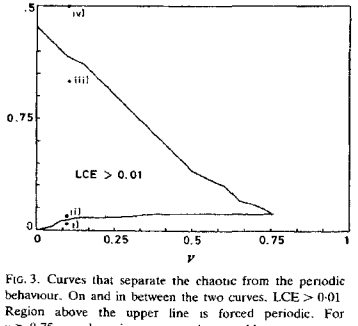

FIG. 3. Curves that separate the chaotic from the periodic behaviour. On and in between the two curves, LCE > 0·01 Region above the upper line is forced periodic. For $\nu > 0{\cdot}75$, no chaos is seen according to this criterion.

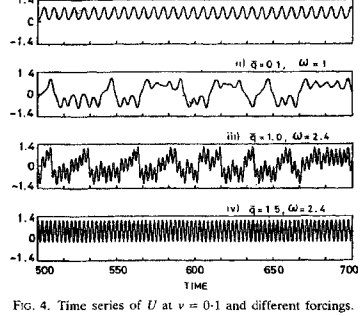

FIG. 4. Time series of U at $\nu = 0{\cdot}1$ and different forcings. The numbers correspond to points marked in Fig. 3.

Therefore, the routes to chaos in the model have been explored in detail under different external forcings. The findings may be summarized as follows.

4.1. *Periodic forcing*

(a) With forcing frequency near the natural frequency of the model, a cascade of period-doubling bifurcations precedes chaos as the forcing amplitude increases at a fixed Reynolds number; the scenario with constant forcing amplitude and increasing Reynolds number is more complicated and period-doubling bifurcations are possible in this case too. In both the cases, the results are in reasonably good agreement with the Feigenbaum scenario[5].

(b) With much higher forcing frequency, when the Reynolds number increases at a fixed forcing amplitude, the onset of chaos is sudden, and quasi-periodicity and frequency locking precede it.

4.2. *Stochastic forcing*

(a) For a Gaussian pink noise with a spectral density maximum in the neighbourhood of the natural frequency of the model, either quasi-periodicity or higher states of frequency locking (*i.e.*, frequencies related in the ratio of large integers) precede chaos.

(b) For an amplitude-limited white noise, random bursts of large amplitude oscillations, *i.e.*, intermittency, precede chaos.

5. Conclusions

1. Based on physical arguments that are valid for turbulent flows in general, it is possible to construct simple dynamical models that possess many features characteristic of transition and turbulence in open flows.
2. The studies on the routes to chaos suggest that the transition is strongly influenced by the nature of external disturbances.
3. Comparison model results and observed behaviour from boundary-layer studies suggests that the Navier–Stokes equations may contain homoclinic orbits in the limit of infinite Reynolds number.

References

1. Guckenheimer, J. and Holmes, P. — *Nonlinear oscillations, dynamical systems and bifurcations of vector fields*, 1983, Springer Verlag
2. Eckmann, J.-P. — Roads to turbulence in dissipative dynamical systems, *Rev. Mod. Phys.*, 1981, **53**, 643–654.
3. Feigenbaum, M. J. — Quantitative universality for a class of nonlinear transformations, *J. Stat. Phys.*, 1978, **19**, 25–52.
4. Hao, B. L. — *Chaos*, 1984, World Scientific.
5. Gollub, J. P. and Benson, S. V. — Many routes to turbulent convection, *J. Fluid Mech*, 1980, **100**, 449–470.
6. Gollub, J. P. and Swinney, H. L. — Onset of turbulence in a rotating fluid, *Phys Rev. Lett.*, 1975, **35**, 927–930.
7. Monin, A. S. — On the nature of turbulence, *Sov. Phys. Uspekhi*, 1978, **21**, 429–442.
8. Morkovin, M — *ICASE Report No. 88–44*, NASA Contractor Report 181693, 1988.
9. Narasimha, R. — Order and chaos in fluid flows, *Curr. Sci.*, 1987, **56**, 629–645.
10. Batchelor, G. K. — *The theory of homogeneous turbulence*, 1953, Cambridge University Press.
11. Schubauer, G. B. and Skramstad, H. K. — *NACA Report 909*, 1948.
12. Narasimha, R. and Bhat, G. S. — Dynamical systems that mimic flow turbulence, *Curr. Sci.*, 1988, **57**, 697–702.
13. Wolf, A., Swift, J. B., Swinney, H. L. and Vastano, J. A. — Determining Lyapunov exponents from a time series, *Physica D*, 1985, **16**, 285–317.

Thesis Abstract (Ph.D.)

Sensitivity studies on the structure of the monsoon desert heat low by T. Venugopal.
Research supervisor: M. Sankar Rao.
Department: Aerospace Engineering.

1. Introduction

The Asian summer monsoon is characterised by seasonal reversal of winds from easterlies to westerlies. The reversal is due to strong pressure gradients developed by the strong land–sea surface–heating contrasts. The persistent seasonal surface low over the entire Afro-Asian land mass in the desert regions during the northern hemispheric summer and the associated lowest surface pressure over the north-west Rajasthan in the Indian subcontinent is of primary importance in the studies of monsoon dynamics.

2. Model

The sensitivity of the atmospheric response to the large-scale summer continental sensible heat sources such as those prevailing over the great deserts of the Afro–Asian land mass is studied using a linear steady-state quasi-geotrophic model with basic barotropic and baroclinic mean winds. A heating profile represented by Gaussian distribution in the lat–long directions and an exponentially decaying function in the vertical is considered. At the centre of the source, a heating rate of the order of 2°C day^{-1} is prescribed[1,2].

3. Results and discussion

The vertical structure of the monsoon desert low is found to depend on the horizontal extent of the heat source, the vertical extent of heating over the source and the mean zonal wind.

With basic barotropic mean state, the pressure perturbation oscillates rapidly in the vertical for very weak mean zonal winds. Shallow heating gives rise to stronger surface lowest pressure but the low is not deep. For mean zonal winds of the order of 2 ms^{-1}, maximum surface lowest pressure occurs with moderately deep heating irrespective of the lateral extent of the source. But the extension of the low from surface to 900 mb is seen with shallow heating. For winds of the order of 5 ms^{-1} with moderately deep heating, the surface low extended up to 900 mb and a high above it is noticed. For winds of 10 ms^{-1}, with moderately deep heating, the surface low is extended up to 800 mb.

Vertical velocities are found to depend on the vertical extent of heating. For mean winds of the order of >1 ms^{-1}, descending motions occur over the source and over the surface low between the surface and 800 mb when the vertical heating is moderately deep. With deep heating, however, ascending motions occur. Weak vertical velocities are noticed with stronger mean winds. In such cases, there are descending motions occurring between the surface and 600 mb. Stronger ascending motions occur with deep heating in the vertical over the source and over the surface low for mean winds of the order of 2 ms^{-1}.

When surface Ekman friction is introduced, the pressure perturbation depends on the depth of heating in the vertical and the strength of the mean zonal wind.

When wind shear is introduced, the features of the vertical structure differ from the barotropic case. For surface mean winds of the order of 0·2, 1·0 and 2·0 ms^{-1}, the extent of the low in the vertical depends on the extent of the heating in the vertical. For U_0=0·2 ms^{-1}, the extent of low is up to 800 mb with shallow heating and up to 700 mb with moderately deep heating for all lateral extents of the heat source. The surface lowest pressure is the strongest for the widest source.

In general, the surface low pressure occurs to the east of the sensible heat source. For the widest source it is about 5000 km to the east. If the Afro–Asian heat source is put at (27°N, 30°E), then the surface low will be around (27°N, 75°E) which is close to reality.

The general nature of these results indicates the overwhelming importance of the vertical structure and intensity of the mean wind and the vertical structure and the extent of the heating profile. In general,

stronger the mean wind, the weaker the perturbations. This implies that if the westerlies over the desert regions are slightly stronger than usual, the monsoon development could be weaker. Wider the source width, the stronger the monsoon. But the source width in the real nature remains almost the same constituting the Afro–Asian desert region. However, deeper heating can give rise to stronger monsoon according to these computations.

References

1. DAS, P. K. AND JULKA, M. L. *Beitr. zur. Atmos.*, 1967, **40**, 168–178

2. BLAKE, D W., KRISHNAMURTI, T. N. AND LOW-NAM, S. V. *Mon. Weath. Rev.*, 1983, **111**, 1759–1775

Thesis Abstract (Ph.D.)

Analysis of two-dimensional downstream-mixing 16-μm CO_2 gasdynamic laser by Purandar Chakravarty.
Research supervisors: N. M. Reddy and K. P. J. Reddy.
Department: Aerospace Engineering.

1. Introduction

In recent years, realization of the effective use of a 16-μm laser beam for enrichment of uranium, through the process of laser isotope separation involving UF_6, has motivated considerable research efforts to obtain a high-gain, high-performance 16-μm laser source. Theoretical studies[2] have shown that the premixed, conventional CO_2 gasdynamic laser (GDL) is a superior device among the various existing lasers for generation of 16 μm. However, the scope of even such systems, in terms of attainment of high small-signal gain and power at 16 μm are limited. A possible alternative solution is to use the 'downstream-mixing' scheme, where a cold CO_2–H_2 stream is mixed with a vibrationally excited N_2 stream at the nozzle exits, which may lead to higher small-signal gain and power. The work reported contributes towards confirming this possibility by numerically investigating a CO_2 downstream-mixing GDL for the generation of 16-μm lasing.

The main intent of this investigation is to study the detailed characteristics and performance potential of a CO_2 downstream-mixing GDL as a high-power laser device for 16-μm lasing operation, and also to obtain a generalized, two-dimensional flow-radiation-coupled power extraction modeling to evaluate the power of GDLs. Generation of 16 μm has been studied through both the processes, *i.e.*, by using an external 9·4-μm stimulation, and also by generating 9·4 μm from the system itself to obtain 16-μm lasing through intracavity cascading process. A brief review of these investigations with results is presented here.

2. Profile of investigations

As a first step a detailed two-dimensional numerical simulation of the non-equilibrium supersonic flow in a 16-μm CO_2 downstream-mixing GDL has been done, using an explicit, time-dependent, second-order accurate, finite difference numerical technique based on the predictor-corrector approach of MacCormack. For this purpose, a complete two-dimensional unsteady, laminar, viscous, and compressible flow model for the analysis of such a system with external injection of 9·4 μm has been used[3]. Further, this approach is adopted to carry out a complete parametric analysis of such a laser and optimization of 16-μm small-signal gain[4]. The effects of N_2 reservoir temperature[5] and line shape function through Voigt function[8], *i.e.*, considering the combined effect of Lorentzian and Doppler broadening, on 16-μm small-signal gain have also been investigated. The results of 16-μm small-signal gain are found to be as high as 16·7 m^{-1} for Lorentzian broadening and 11·0 m^{-1} considering Voigt function.

In the next step, to eliminate the need for external injection of 9·4-μm laser, the possibility of generation of 9·4-μm laser from within such a system is investigated[7]. The 9·4-μm small-signal gain of the order of

10·0 m^{-1} and 3·91 m^{-1} considering Lorentzian broadening and Voigt function, respectively, have been obtained.

Having accomplished this, a generalized two-dimensional flow-radiation-coupled model to extract power from a GDL has been developed[8] by coupling the non-lasing numerical solution technique of the first step with radiation. This modeling has been used for the evaluation of power extraction at 9·4 μm. The 9·4-μm intensity along with actual gain and population inversion across the mirror length has been investigated in detail. The role of H_2 catalyst in power extraction has also been investigated. The steady-state value of intensity as high as $5{\cdot}0 \times 10^7$ Watt/m^2 has been obtained from this analysis.

This high value of 9·4 μm intensity has given impetus to extend this analysis for power generation at 16 μm through cascade process, *i.e.*, simultaneous lasing at 9·4 and 16 μm. However, due to inherent limitations of the existing vibrational kinetic models, it was realized that none of them is capable of modeling such a process. Therefore, a new 4-mode vibrational kinetic model for CO_2–N_2 system has been proposed. Using this model, along with the power extraction model developed earlier, 16-μm laser generation through cascading process has been investigated[9]. The 16-μm laser intensity along with the actual gain and population inversion are also computed across the mirror length. The role of H_2 catalyst which is very prominent in this case is also investigated in detail[2]. The intensities for 16 and 9·4 μm as high as $1{\cdot}0 \times 10^6$ Watt/m^2 and $5{\cdot}0 \times 10^7$ Watt/m^2, respectively, have been obtained with the presence of 10% of H_2 in the laser gas mixture.

3. Conclusions

Major conclusions drawn from this analysis are:

1. Two-dimensional simulation of 16-μm CO_2 downstream-mixing GDL giving deeper insight of the complete flow field, gain, and intensity characteristics highlights the potential of such a laser for industrial applications, especially for enrichment of uranium through the process of laser isotope separation.
2. The two-dimensional flow-radiation-coupled power-extraction model developed in this analysis is a generalized one and can be used for any kind of GDLs or chemical lasers or similar laser devices.
3. The new vibrational kinetic model for CO_2–N_2 system proposed here is the most advanced among the existing ones.
4. Generation of 9·4 μm and also cascade generation of 16-μm lasing is possible from such a laser device with encouraging results.

References

1. Eerkens, J. W. — Spectral consideration in the laser isotope separation of uranium hexafluride, *Appl. Phys.*, 1976, **10**, 15–31.
2. Suzuki, K., Saito, S, Obara, M. and Fujioka, T. — Theoretical study for a 16-μm CO_2 gasdynamic laser, *J. Appl. Phys.*, 1980, **51**, 4003–4009
3. Chakravarty, P and Reddy, N. M — Theoretical study of a 16-μm CO_2 downstream-mixing gasdynamic laser : A two-dimensional approach. *Appl. Phys Lett.*, 1986, **48**, 263–265
4. Chakravarty, P., Reddy, N. M and Reddy, K. P. J. — Two-dimensional analysis of a 16-μm CO_2 downstream-mixing gasdynamic laser, *AIAA J*, 1987, **25**, 713–720
5. Chakravarty, P., Reddy, N. M. and Reddy, K. P. J. — A study of the effect of N_2 reservoir temperature on a 16-μm CO_2–N_2 downstream-mixing gasdynamic laser, *Opt. Commun*, 1986, **58**, 130–132
6. Chakravarty, P., Reddy, N. M. and Reddy, K. P. J. — Performance characteristics of a 16-μm CO_2 downstream-mixing gasdynamic laser, *J. Aero. Soc. India*, 1988, **40**, 243–246
7. Chakravarty, P, Reddy, N. M. and Reddy, K. P J. — Evaluation of downstream-mixing scheme for 9·4-μm CO_2 gasdynamic laser, *Pramana*, 1990, **34**, 333–345.
8. Chakravarty, P., Reddy, N. M. and Reddy, K. P. J. — A flow-radiation coupled power extraction model for a gasdynamic laser, presented at the *IEEE National Seminar on Lasers in Engineering and Medicine (LasEM–89)*, Trivandrum, India, Nov. 30–Dec 02, 1989.
9. Chakravarty, P., Reddy, N. M. and Reddy, K. P. J. — Analysis of a cascade pumped 16-μm CO_2–N_2 downstream-mixing gasdynamic laser, *Appl. Phys Lett.*, 1990, **57**, 852–854.

Thesis Abstract (Ph.D.)

Role of subsurface flows in the ignition of liquid fuel pools—A theoretical study by T. Venkateswara Rao.
Research supervisor: V. K. Jain.
Department: Aerospace Engineering.

1. Introduction

The work is a theoretical study on the ignition of a pool of liquid fuel at subflash temperatures under the action of localized ignition sources.

While a few experimental results are available in literature, no theoretical study exists to explain the observed effects and elucidate the factors that influence the ignition. Of particular importance is the fact that ignition delay times in the case of liquid fuel pools are substantially larger (sometimes as much as 3 to 4 orders of magnitude) than the corresponding values for solid fuels under similar conditions. Experimental evidence indicates strong sub-surface currents preceding the ignition event, resulting in a large body of liquid being heated before the critical conditions for ignition are achieved. Two probable mechanisms for the observed liquid motions have been advanced, viz., a surface tension drive due to the variation of surface tension with temperature along the liquid surface and a buoyancy drive due to density differences in the bulk of the liquid. Other important observations include the effect on ignition delay of i) geometric factors such as the depth and extent of the pool, ii) nature of the substrate on which the fuel rests, iii) additives which modify the physical properties of the liquid, and iv) the magnitude and distribution of heat flux, etc. The present work is undertaken to clarify the role of various factors that influence ignition, thereby substantiating experimental observations and predict possible new effects. The work particularly aims to clarify the relative roles of surface tension and buoyancy.

2. Model

The mathematical model employed for the theoretical study is essentially a condensed-phase heat-up model and comprises Navier–Stokes and energy equations, as specialized to a liquid pool exchanging heat at its free surface with a localized heat source. The problem is set up as an initial boundary-value problem for the laminar motion of a Boussinesq fluid in an open cavity and the transient thermal history of the pool is studied until ignition. The ignition event itself is judged on the basis of first attainment of a specified temperature (the fire-point of the liquid) at some location on the surface. The model takes into account all the relevant variables such as buoyancy, surface tension variation with temperature, incident heat flux distribution, and appropriate thermal exchange conditions at the boundaries including heat losses due to vapourization at the surface. The model is quite general in the sense that both two-dimensional and axi-symmetric cases are included. The equations are appropriately non-dimensionalized and important non-dimensional groupings such as the Marangoni, Rayleigh, and Prandtl numbers are identified. The non-dimensionalized equations are finally cast into a stream function-vorticity form to facilitate their solution by numerical methods.

3. Numerical solutions

Solutions are sought by numerical means and, in view of the large computational times involved, a comparative study is undertaken to evolve a computationally economical, time-accurate numerical scheme. Specifically, the following two schemes were tried: i) an implicit Hopscotch scheme, and ii) an alternating direction implicit (ADI) scheme.

For both the schemes, the spatial discretization is kept similar and has the following features: a) Conservative differencing over variable meshes in both spatial directions, and b) an option for upwind, central, or hybrid upwind/central scheme for the convective terms. Studies performed on a model set of parameters reveal a number of interesting features. The Hopscotch method is prone to nonlinear instability when the wall vorticity is lagged by one time step and performs very poorly, even though on an operation count

basis it is the most attractive The instability is readily cured by iterative improvement of the solution but in the process, the method loses its competetiveness. ADI method performs quite well and results in smooth and accurate solutions. Contrary to what is generally believed, this method gives time-accurate solutions up to a Courant Number of 5·0, even though economical computations are obtained around Courant Number 3·0. In addition to evaluating the two differencing schemes, the influence of factors like artificial viscocity, the type of treatment of energy boundary conditions, and the stretching of the numerical grid on the accuracy of the numerical solutions is brought out

4. Results and discussion

Fairly extensive numerical results are presented for the case of a plane two-dimensional pool with a strip source of heating for a range of physical parameters representative of alcohols. The geometry and heating conditions closely correspond to the situation obtained in the experiments of Burgoyne, wherein the ignition of a two-dimensional liquid pool was effected by means of a flame stabilized on a wick. The numerical results on ignition delays and the details of the fluid flow compare quite favourably with the experimental results. Although a fairly broad-based coverage in the non-dimensional parametric space is not possible due to the large computational times (some parameter sets take more than 4 hours of CPU time on DEC–1090 system), sufficient results are obtained to clarify the role of various parameters like buoyancy, liquid depth, initial temperature, lateral extent of the channel, and heat-exchange conditions at the bottom of the pool.

References

1 SRIGNANO, W A AND GLASSMAN, I — Flame spreading above liquid fuels, surface-tension-driven flows, *Combust. Sci. Technol.*, 1970, **1**, 307–312

2. TORRANCE, K.E — Subsurface flows preceding flame spread over a liquid fuel, *Combust Sci. Technol* , 1975, **3**, 133–143.

3. TORRANCE, K E. AND MAHAJAN, R L — Fire spread over liquid fuels, Liquid-phase parameters; *XVth Symp. (Inter.) on Combustion*, 1975, 281–287

Thesis Abstract (Ph.D.)

Vibration of cables under deterministic and random excitations by G. Visweswara Rao.
Research supervisor: R. N. Iyengar.
Department: Civil Engineering.

1. Introduction

Cables form structurally efficient and economical load-carrying members in many engineering applications. The study of cables is of primary interest to structural, offshore and power engineers. The taut string which is the limiting case of a sagged cable has received much attention in literature. Even though cables also have been studied since a long time, certain important aspects like extensibility have been studied recently. Influence of nonlinearity is another topic which is currently receiving much interest. Since cables are by their very nature displacement sensitive and possess low damping, consideration of nonlinear effects in the analysis assumes importance. Uncertainties in the input forces such as earthquake and wind excitation introduce additional complicating effects which may have significant influence on the cable behaviour.

2. Present work

The work reported covers some aspects of both linear and nonlinear behaviour of cables. The scope of the investigation is as follows:

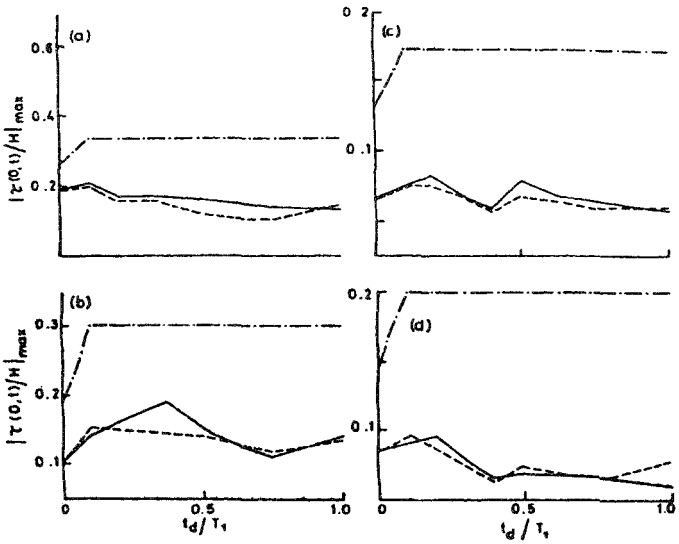

FIG. 1. Peak additional cable tension *vs* time lag, t_d ——— Time history analysis, ------ modified SRSS method, ·····ABS method.

a) To examine the complicating effect of a lateral load on the eigensolution of the cable and instability of the inplane oscillations.

b) To estimate the effect of seismic support excitations and their transmission time between the two ends, on the additional cable tension.

c) To analyse the effect of nonlinearities and associated internal and external resonance phenomena on the coupled inplane out-of-plane oscillations of a cable.

d) To study the effect of random excitation forces on the nonlinear behaviour of a cable.

3. Results and discussion

3.1. *Linear behaviour of cables*

In the absence of a lateral load, the out-of-plane oscillations of a cable get uncoupled from the inplane oscillations[1]. However, an oscillating lateral load could induce strong coupling between the lateral and the inplane oscillations. There is continuous exchange of energy between the corresponding modes of oscillation. It may be expected that due to this coupling, cables could exhibit beat oscillations. For certain combination of cable parameters defining its sag and extensibility, the frequency crossover of the symmetric modes over the anti-symmetric ones is possible. In addition, the presence of a periodic component in the lateral load, even though uniform, could lead to parametric instability in the cable.

For long span cables under support motion due to earthquakes, the transmission time between the two ends has strong influence on the cable response. A cable experiences substantial increase in the dynamic tension when compared to the uniform excitation case[2], even for a short transmission time, equivalent to half of its first natural period. A response spectrum method, suitably modified to incorporate the effect of the transmission time, is developed to estimate the cable tension. Results obtained for a typical long span cable under the action of El centro 1940 and Taft 1952 earthquakes are shown in Fig 1. In this figure, τ is the additional cable tension, H the static tension, T_1 the first natural period of the cable, and

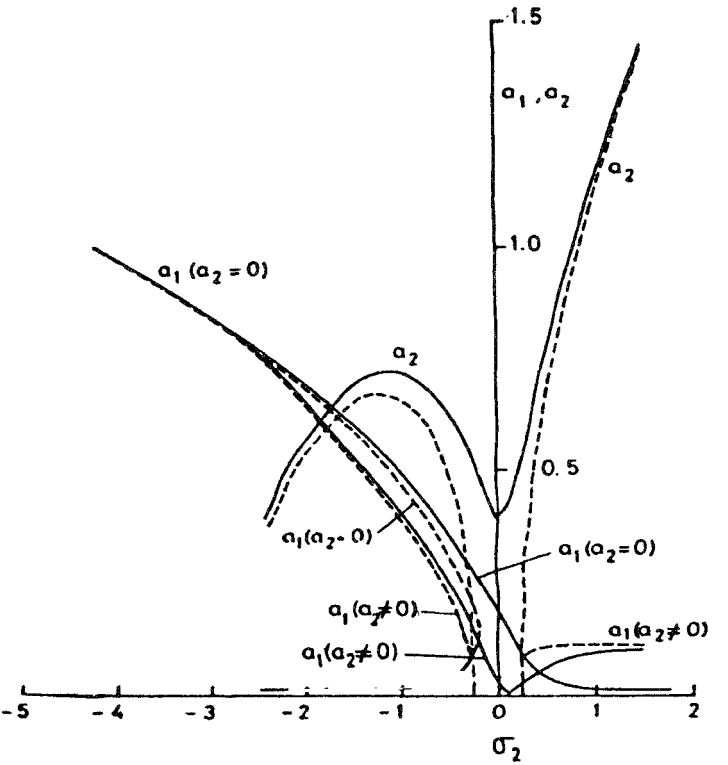

FIG. 2. Effect of internal resonance in cables. Planar and non-planar motions. ——— stable, ------ unstable.

t_d the time delay between the excitations at the two supports. The analysis includes longitudinal inertia effects and thus the significant participation of elastic modes in the response contribution is highlighted. It may also be necessary to include the supporting tower stiffness for a more realistic analysis.

3.2. *Nonlinear behaviour of cables*

The nonlinear analysis of cable is characterized by the presence of quadratic nonlinearities in the equation of motion, in addition to the cubic nonlinearities. In the case of a taut cable[3], the cubic nonlinear terms dominate resulting in a predominantly hardening behaviour. On the other hand, for cables even with moderate sag-to-span ratio, the quadratic nonlinearity terms predominate. It results in an internal resonance condition of 2:1 relation between the inplane and out-of-plane frequencies. Under inplane harmonic excitation, the internal resonance combined with an external resonance induces nonplanar motion to develop within a certain region of external-forcing frequency. The stability pattern of the possible steady-state solutions of the non-planar motion significantly changes with the internal resonance parameter and thus with variation of cable sag. Results on the frequency response behaviour of a typical cable are shown in Fig. 2. In the figure, a_1 and a_2 represent the amplitudes of vertical and lateral displacements, and σ_1 and σ_2 the internal and external resonance–detuning parameters. The presence of a uniform lateral load acting along with the inplane harmonic excitation also strongly influences both the existence and stability of the non-planar motion. The results presented give indication that cables may exhibit chaotic oscillations in certain parameter space.

The study on the uncertainties in the input forces considers two excitation models, one being a narrow-band random process and the other a combined periodic and white-noise process. The choice of these types of excitation is prompted by the fact that both the models can represent the fluid-dynamic forces which arise out of vortex shedding and exhibit existence of a predominant Strouhal frequency along with stochasticity. As a first step towards understanding the cable behaviour under these excitation models, the analysis is restricted to the first symmetric vertical mode of oscillation. The equivalent linearization technique is adopted in the analysis. The quadratic nonlinearity term leads to bias or a mean value in the response. The equivalent linearization technique gives rise to multiple response moments in certain range of external frequency. Since the moments of a random variable are unique, only one among the multiple solutions need be acceptable. The acceptability of the steady-state solutions is checked by an almost sure asymptotic stability analysis[4]. In the multi-valued region, only one of the steady-state response moments is observed to be stable. The theoretical results are supported by digital simulation.

References

1. IRVINE, H. M. AND CAUGHEY, T. K. — The linear theory of free vibrations of a suspended cable, *Proc. R. Soc. Lond*, 1974, **341**, 299–315
2. IRVINE, H. M., — The estimation of earthquake-generated additional tension in a suspension bridge cable, *Earthquake Engng Struct. Dynamics*, 1980, **8**, 267–273.
3. AL-NOURY, S. I. AND ALI, S. A., — Large-amplitude vibrations of parabolic cables, *J. Sound Vibr.*, 1985, **101**, 451–462.
4. IYENGAR, R. N. — Stochastic response and stability of the Duffing oscillator under narrowband excitation, *J. Sound Vibr.*, 1988, **126**, 255–263.

Thesis Abstract (Ph.D.)

Random vibration of limit cycle systems and stochastic strings by C. S. Manohar.
Research supervisor: R. N. Iyengar.
Department: Civil Engineering.

1. Introduction

The work deals with two specific nonlinear problems that arise in random vibration of engineering systems.

The first problem pertains to the effect of different types of random excitations on the inherent periodic motions of a limit cycle system. The second problem is to find the probability distribution of the eigenvalues of a stochastic string. The solution of this problem is obtained by solving a first-order nonlinear stochastic differential equation.

2. Stochastic response of Van der Pol's oscillator

The limit cycle system considered is the classical Van der Pol's oscillator governed by the equation

$$\ddot{x} - \epsilon\dot{x}\ (1 - 4x^2) + x = f(t). \tag{1}$$

For the case of $f(t) = 0$ the system possesses a stable limit cycle given by

$$x(t) = \sin\ (t + \phi_0) + 0(\varepsilon). \tag{2}$$

Here ϕ_0 is an arbitrary constant dependent on the initial conditions. In the present study, three specific models for $f(t)$ are assumed. These are (i) $f(t) = W(t)$ where $W(t)$ is a gaussian white noise with autocorrelation $< W(t_1)W(t_2) > = 2D\delta(t_1 - t_2)$, (ii) $f(t) = P\cos\ \lambda t + W(t)$, and (iii) $f(t)$ is a narrow-band filtered white noise random process.

New methods of response analysis based on closure approximations, stochastic averaging and equivalent nonlinearization technique are developed in the study. The interaction between external noise and the limit cycle of the system produces distinctly nongaussian response. This invalidates the application of linearization methods based on gaussian approximation to the response. A closure solution based on a bimodal probability density function (pdf) has been developed in this work which leads to acceptable results. Figure 1 shows the theoretical joint pdf of the response x and $\dot{x}$. The maxima and minima in this

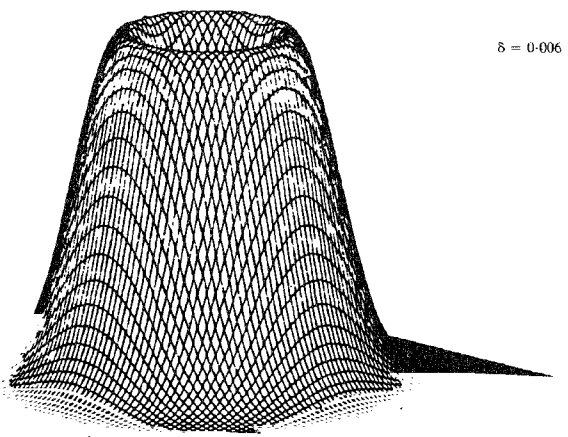

FIG 1. Joint probability density function of x and $\dot{x}$.

function correspond respectively to the stable limit cycle and the unstable focus of the unforced system At low levels of noise when the response is mainly controlled by the limit-cycle behaviour, it is observed that the probability distribution of the initial conditions strongly influences the transient behaviour. Digital simulation studies for the case of white-noise excitations have shown that the response phase does not have a uniform probability distribution as predicted by the existing theories. The newly developed method of combined averaging and nonlinearization successfully predicts this nonuniform distribution. For the case of $f(t) = P\cos\lambda t + W(t)$, there exists a region in parameter space where the linearization solutions give acceptable answers. The response here has a mean periodic component. The effect of noise is to reduce the mean response and increase the variance. The requirement of stochastic structural stability of approximate solutions has been effectively employed in the present study to verify the validity of the assumptions made on response characteristics.

3. Probability distribution of eigenvalues of the random string equation

The eigenvalue problem that arises in the vibration of stochastic strings, bars, shafts and soil layers can be started as finding the solution of the boundary-value problem

$$\frac{d}{dx}\left[(1 + \delta g(x))\frac{dy}{dx}\right] + \lambda^2 [1 + \epsilon f(x)]y = 0$$

$$y(0) = y(1) = 0. \tag{3, 4}$$

Here $g(x)$ and $f(x)$ are taken to be stationary random processes with a specified joint pdf. λ is the eigenvalue parameter which is now a random variable. In the present study, the pdf of the eigenvalues is determined by studying the zeros of the solution $y^*(x, \lambda)$ of eqn (4) together with the initial conditions

$$y^*(0) = 0; \frac{dy^*}{dx}(0) = 1. \tag{5}$$

The approach is based on an earlier work by Iyengar and Athreya[1]. Here the process $y^*(x, \lambda)$ is expressed in the form

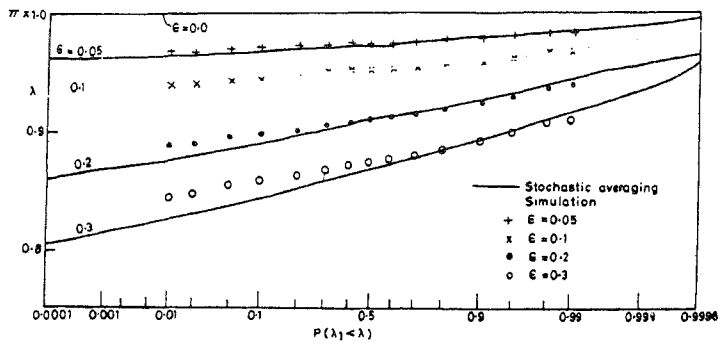

FIG. 2. Probability distribution of the first eigenvalue.

$$y^*(x,\lambda) = r \sin(\Theta + \lambda x) \tag{6}$$

$$(1 + \delta g)\frac{dy^*}{dx}(x, \lambda) = r\lambda \cos(\Theta + \lambda x).$$

The probability distribution of nth eigenvalue can be shown to be given by

$$P[\lambda_n \leqslant \lambda] = P[n\pi - \lambda < \Theta(1, \lambda)]. \tag{7}$$

Here, $\Theta(x, \lambda)$ is governed by

$$\frac{d\Theta}{dx} = \frac{\lambda \cos^2(\Theta + \lambda x)}{1 + \delta g} + \lambda(1 + \epsilon f)\sin^2(\Theta + \lambda x) \tag{8}$$

$$\Theta(0) = 0.$$

Thus, to find $P[\lambda_n \leqslant \lambda]$ one has to solve the above first-order nonlinear stochastic differential equation. In the present study, specific models for $g(x)$ and $f(x)$ are assumed so that eqn (8) can be solved analytically. Solutions based on Markov process theory, stochastic averaging and closure approximations are obtained and compared with digital simulations. Figure 2 shows the probability distribution of the first eigenvalue obtained using the stocahstic averaging technique for the case of $\delta = 0$ and $f(x)$ being a gaussian random process with mean = 1·0 and power spectral density $S(w) = 0{\cdot}4/[16 + w^2]$. The theoretical solutions show good comparison with digital simulations especially for low values of ϵ. These results are first of their kind in literature and form an important step in the analytical treatment of the stochastic string equation.

References

1. IYENGAR, R. N. AND ATHREYA, K. B. A diffusion process approach to a random eigenvalue problem, *J. Indian Inst Sci*, 1975, **57**, 185–191.

Thesis Abstract (Ph.D.)

Studies on lightweight fibrous ferrocement in compression, tension and flexure by Said Abd El-fattah El-kholy.
Research supervisor: Prakash Desayi.
Department: Civil Engineering.

1. Introduction

Since ferrocement units are thin, ranging from 20 to 40 mm, thermal comfort is one of the aspects to be borne in mind while designing or adopting ferrocement for housing construction. Replacement of sand by lightweight aggregate (LWA) would satisfy this condition. Short steel fibres when added to ferrocement improve its strength and cracking behaviour. Thus, lightweight fibrous ferrocement appears to have considerable potential as a construction material. While extensive studies are reported on mechanical properties of ferrocement and few studies on lightweight ferrocement, no information is available on lightweight fibrous ferrocement. Hence, this investigation has been undertaken to study the strength and behaviour of lightweight fibrous ferrocement (in which sand is replaced by foamed blast furnace slag) in compression, tension and flexure.

2. Workability and strength of lightweight fibrous mortar

2.1. *Experimental work*

Three values of water-cement ratio (w/c), *viz.*, 0·45, 0·50 and 0·55 by weight, three percentages of sand

replacement by foamed blast furnace slag, *viz* , 0·0, 35 and 70% by weight and four values of fibre volume fraction, *viz*., 0·0, 0·5, 1·0 and 1·5% were used. Different combinations of these parameters resulted in 36 mixes. Mix proportion of cement to fine aggregate of 1:2 was used. Fibres used were hooked steel fibres of aspect ratio of 80. Workability has been studied using slump cone and V–B consistometer. Also, for each of the 36 mixes, 6 cubes and 100mm nominal side (a total of 216 cubes) were cast and used in determining the density, compressive strength and splitting tensile strength of the different mixes.

2.2. *Results*

Results obtained from the test data are as follows:

i) Workability in terms of slump and V–B time increases with increasing w/c ratio and decreases with increase of the percentage of sand replacement.

ii) Inclusion of fibres reduces the workability.

iii) Density of lightweight fibrous mortar reduces with increase in the percentage of sand replacement while the effects of w/c ratio and fibres are found to be minor.

iv) Cube compressive strength reduces with increase in the w/c ratio or the percentage of sand replacement The influence of fibre inclusion on this property is found to be non-uniform.

v) Best fit equations have been obtained to predict the splitting tensile strength of such mortar for all percentages of sand replacement as follows:

$$\sigma_t = \sqrt{f_{cu}}\,[13{\cdot}547\ V_f + 0{\cdot}646] \quad \text{for w/c} = 0{\cdot}45, \tag{1}$$

$$\sigma_t = \sqrt{f_{cu}}\,[11{\cdot}20\ V_f + 0{\cdot}595] \quad \text{for w/c} = 0{\cdot}50; \tag{2}$$

$$\sigma_t = \sqrt{f_{cu}}\,[6{\cdot}027\ V_f + 0{\cdot}627] \quad \text{for w/c} = 0{\cdot}55. \tag{3}$$

3. Lightweight fibrous ferrocement in compression

3.1. *Experimental work*

Test specimen selected was a prism of 100 mm square in cross-section and 200 mm in height. Parameters considered in this study were the percentage of sand replacement by LWA, volume fraction of

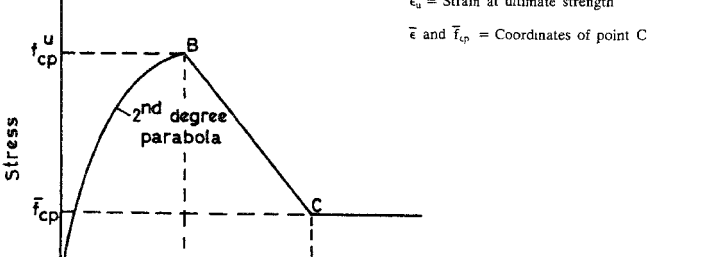

FIG. 1. Proposed stress-strain diagram for lightweight fibrous ferrocement in compression

mesh wires and fibre volume fraction. A total of 48 prisms were tested in compression and a complete stress-strain curve including the descending post-peak portion was obtained.

3.2. *Results*

Based on the test data, the following results have been obtained.

i) A model is proposed for the complete stress-strain diagram for lightweight fibrous ferrocement in compression. This is shown in Fig. 1. Coordinates of points B and C of Fig. 1 for the parameters varied have been obtained from statistical analysis of test results and the resulting equations are:

Ultimate strength

for 0·0% replacement

$$f^{u}_{cp} = \sqrt{f_{cu}}[161{\cdot}14\ V_s - 47{\cdot}60\ V_f + 6{\cdot}27]; \tag{4}$$

for 35% replacement

$$f^{u}_{cp} = \sqrt{f_{cu}}\ [130{\cdot}29\ V_s - 80{\cdot}54\ V_f + 4{\cdot}71]; \tag{5}$$

for 70% replacement

$$f^{u}_{cp} = \sqrt{f_{cu}}\ [299{\cdot}71\ V_s - 93{\cdot}29\ V_f + 3{\cdot}63]. \tag{6}$$

Strain at ultimate stress

$$\epsilon_u = \sqrt{f_{cu}}\ [0{\cdot}0339\ V_s + 0{\cdot}013\ V_f + (3{\cdot}525 \times 10^{-4})]. \tag{7}$$

Stress at the stabilised point

for 0·0% replacement

$$\bar{f}_{cp} = \sqrt{f_{cu}}\ [17{\cdot}14\ V_s - 60{\cdot}05\ V_f + 0{\cdot}896]; \tag{8}$$

for 35% replacement

$$\bar{f}_{cp} = \sqrt{f_{cu}}\ [21{\cdot}66\ V_s - 60{\cdot}05\ V_f + 1{\cdot}039]; \tag{9}$$

for 70% replacement

$$\bar{f}_{cp} = \sqrt{f_{cu}}\ [26{\cdot}23\ V_s - 60{\cdot}05\ V_f + 1{\cdot}324]. \tag{10}$$

Strain at the stabilised point

$$\bar{\epsilon} = \sqrt{f_{cu}}\ [0{\cdot}1337\ V_s + 0{\cdot}098\ V_f + (5{\cdot}457 \times 10^{-4})]. \tag{11}$$

ii) Influences of the constituent materials on the stress–strain characteristics, toughness and ductility have been determined and presented.

4. Lightweight fibrous ferrocement in tension

4.1. *Experimental work*

A streamlined shape of the specimen was used. Parameters considered in this study are three percentages of sand replacement, four values of volume fraction of mesh wires and four values of fibre volume fraction. The different combinations of these parameters resulted in casting and testing 48 specimens.

4.2. *Results*

The following results have been obtained and presented:

i) The stress–strain diagram for specimens tested in uniaxial tension is idealised to a trilinear diagram as shown in Fig. 2. The coordinates of points B and C in this figure have been obtained from statistical analysis of test results and the resulting equations are:

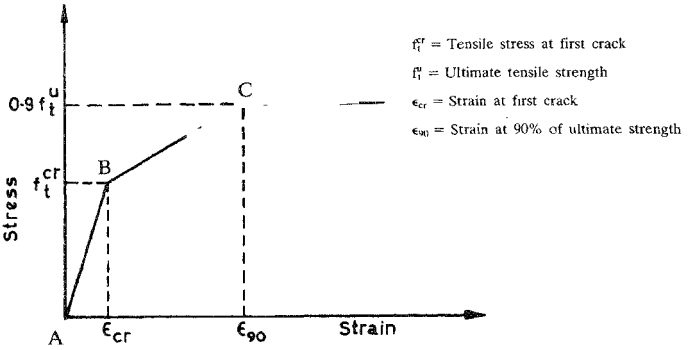

FIG. 2. Idealised trilinear plot for lightweight fibrous ferrocement in tension

First crack strength

$$f_t^{cr} = \sqrt{f_{cu}}\,[40{\cdot}11\ V_s + 8{\cdot}73\ V_f + 0{\cdot}234]; \tag{12}$$

Strain at first crack

$$\epsilon_{cr} = \sqrt{f_{cu}}\,[0{\cdot}0367\ V_s + 0{\cdot}0079\ V_f + (0{\cdot}383 \times 10^{-4})]; \tag{13}$$

Ultimate strength

$$f_t^u = \sqrt{f_{cu}}\,[14{\cdot}15\ V_f + 0{\cdot}234] + \frac{n\pi d^2}{4A} f_{su}; \tag{14}$$

Strain at 90% ultimate stress

$$\epsilon_{90} = \sqrt{f_{cu}}\,[0{\cdot}111\ V_s + 0{\cdot}067\ V_f + (0{\cdot}383 \times 10^{-4})]. \tag{15}$$

ii) Effects of V_s, V_f and percentage of sand replacement on first crack strength, strain at first crack, ultimate strength and strain at 90% of the ultimate strength have been determined and presented.

5. Lightweight fibrous ferrocement in flexure

5.1. *Experimental work*

Test specimen, a rectangular cross-section, was tested in third-point loading. The parameters considered in this study are the percentage of sand replacement by LWA, volume fraction of mesh wires and fibre volume fraction. Different combinations of these parameters resulted in casting and testing 48 specimens.

5.2. *Results*

From the test data, the following results are obtained:

(i) Influence of V_s, V_f and percentage of sand replacement on first crack strength and modulus of rupture of lightweight fibrous ferrocement in flexure have been determined and equations to predict the same are:

$$f_b^{cr} = \sqrt{f_{cu}}\,[64.64\ V_s + 19{\cdot}50\ V_f + 0{\cdot}712]; \tag{16}$$

$$f_b^{u} = \sqrt{f_{cu}}\,[173{\cdot}36\ V_s + 26{\cdot}37\ V_f + 0{\cdot}712] \tag{17}$$

(ii) First crack strength in flexure and its value in axial tension, and ultimate strength in flexure and that in tension have been compared.

(iii) The rising portion of the load-deflection diagram has been represented as a bilinear plot.

(iv) Spacing of cracks has been estimated based on bond-slip hypothesis.

(v) Flexural strength at which the maximum crackwidth reaches the allowable value of 0·1 mm is given by

$$f_{0\,1} = \sqrt{f_{cu}}\,[168{\cdot}185\ V_s + 71{\cdot}343\ V_f]. \tag{18}$$

(vi) Effect of V_s and V_f on toughness and ductility have been obtained.

6. Conclusions

1) Proposed stress–strain diagrams for lightweight fibrous ferrocement in both compression and tension agree satisfactorily with the experimental curves.

2) Proposed bilinear equation to predict the rising portion of the load-deflection diagram has worked satisfactorily.

3) The results would be useful in the development of design procedures for lightweight fibrous ferrocement structural elements required in housing and other constructions.

Notations

A : gross area of the cross-section
d : average diameter of mesh wires
f_{cp}^{u} : ultimate compressive strength of prism
f_{cp}^{s} : compressive stress at the stabilised point
f_{cu} : cube compressive strength (plain mortar)
f_{su} : ultimate tensile strength of single wire
f_t^{cr} : first crack stress in tension
f_t^{u} : ultimate tensile strength
$f_{0\text{-}1}$: stress at which maximum crackwidth reaches 0·10 mm
n : number of longitudinal wires in the cross-section of specimen
V_f : fibre volume fraction
V_s : volume fraction of mesh wires (in the longitudinal direction)
ϵ_{cr} : strain at first crack in tension
ϵ_{90} : strain at 90% of ultimate tensile strength
ϵ_u : strain at ultimate for prism in compression
$\bar{\epsilon}$: strain at the stabilised point of prism in compression
σ_t : splitting tensile strength for mortar cube.

References

1. ACI Committee — Guide for the design, construction and repair of ferrocement, *ACI Struct. J.*, 1988, **85**, 325–351.

2. Desayi, P and Jacob, K. A. — Strength and behaviour of ferrocement in tension and flexure, *Proc. Symp. on Modern Trends in Civil Engineering*, Roorkee, India, 11–13, November 1972, pp 274–279.

3. DESAYI, P. AND REDDY, V. Strength and behaviour of lightweight ferrocement in tension, *Proc. Second Int. Symp on Ferrocement*, Bangkok, Thailand, Jan. 1985, pp 61–73

4. HANNANT, D J *Fibre cements and fibre concretes*, 1978, Wiley

Thesis Abstract (Ph.D.)

Microstrip elliptical ring antenna by Dharmishtan K. Varughese.
Research supervisors: A. Kumar and T. S. Vedavathy.
Department: Electrical Communication Engineering.

1. Introduction

The concept of microstrip antennas was first proposed by Deshchamps as early as 1953[1] but the first practical microstrip antennas were developed in the year 1970 by Byron. Since then microstrip antennas have been studied widely and employed in many practical systems.

MERA (microstrip elliptical ring antenna) has been chosen for theoretical investigation as it equips the designer with one more parameter, namely, eccentricity, than those available in the case of an elliptical patch antenna (Fig. 1). This may provide additional flexibility to the designer.

2.1. *Expression for* E_z

Of the various methods available for the analysis of microstrip antennas, cavity method has been used for the analysis of MERA. In the cavity model (Fig. 2) the microstrip antenna is modelled as a cavity bounded at its top and bottom by electric walls and on its periphery by magnetic walls.

Elliptic cylinder coordinates defined below have been used in the analysis[2].

$$x = h_0 \cosh \xi \cos \eta$$
$$y = h_0 \sinh \xi \sin \eta \qquad (1)$$
$$z = z$$

where h_0 = semi-focal distance.

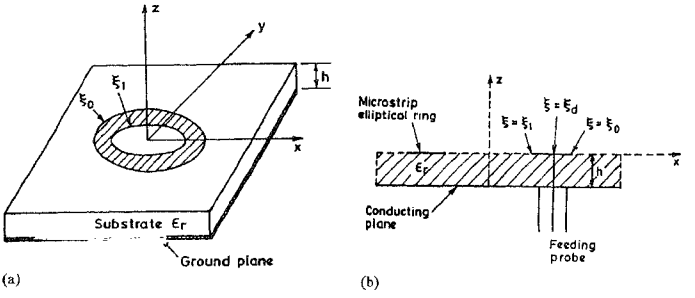

FIG. 1. Microstrip elliptical ring geometry.

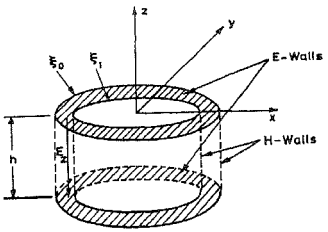

FIG. 2. Cavity model for elliptical ring resonator

Let MERA be excited by a z-directed line current source located at $\xi = \xi_d$ and $\eta = 0$, where $\xi_1 < \xi_d < \xi_0$ so that the current source may be expressed mathematically by

$$\bar{J} = \hat{z}\, I\, f\, \delta\ (\xi - \xi_d)\ \delta(\eta). \tag{2}$$

The expression for E_z has been obtained by solving the wave equation

$$\frac{\delta^2 E_z}{\delta \xi^2} + \frac{\delta^2 E_z}{\delta \eta^2} + 2k^2\ (\cosh 2\ \xi - \cos 2\ \eta)\ E_z = 0 \tag{3}$$

where $2k = ae\ \omega \sqrt{\mu\epsilon}$.

The boundary condition requires that $\delta E_z / \delta \xi = 0$ at $\xi = \xi_0$ and $\xi = \xi_1$. The solution for E_z involves ordinary and modified Mathieu functions.

Expressions for E_x and E_y in terms of E_ξ and E_η have also been derived.

2.2. *Radiation field*

The radiation field of MERA at a point $P(r, \theta, \phi)$ lying in the upper half plane $z \geq 0$ is given approximately by (Fig. 3)

$$E_\theta = \frac{jk_0 e^{jk_0 r}}{4\pi r}\ (f_x \cos\ \phi + f_y \sin\ \phi) \tag{4a}$$

$$E_\phi = \frac{jk_0 \cos\ \theta\ e^{jk_0 r}}{4\pi r}\ (-f_x \sin\ \phi + f_y \cos\ \phi) \tag{4b}$$

where f_x and f_y are the x and y components of the Fourier transform, f, of the aperture field E_a

$$f_t = \iint_{\text{aperture}} E_a \exp\ \{ - jk_0 h_0 \sin\ \theta\ (\cos\ \phi\ \cosh\xi\ \cos\eta + \sin\phi\ \sinh\xi\ \sin\eta)\}\ ds \tag{5}$$

Since h is small compared to the wavelength, it is assumed that the fringing field E_a extends uniformly up to a distance h from the periphery of the ring and is zero beyond that.

$$|E_a| = E_\xi\ |\ \xi = \xi_1,\ \xi_0 = E_z |\ \xi = \xi_1,\ \xi_0. \tag{6}$$

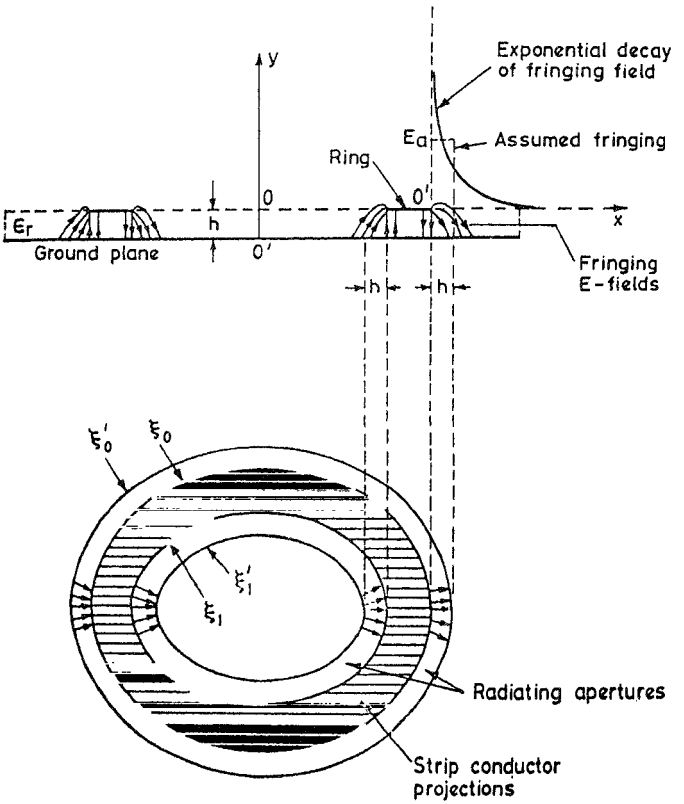

FIG. 3. Approximation of aperture fields E_a due to fringing at the edges of the ring structure.

In terms of rectangular components, the aperture field is given by

$$\tilde{E}_a = \hat{x}E_x + \hat{y}E_y. \tag{7}$$

From these relations it is possible to write expressions for E_θ and E_ϕ for $TM_{z\,mn0}$ and $TM_{z\,mn0}$ modes.

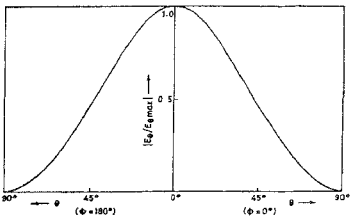

FIG 4a. Radiation patterns of MERA for TM_{c110} mode. $\epsilon_r = 10$, F = 10 GHz, $\xi_0 = 1{\cdot}10$, $\xi'_0 = 1{\cdot}30$, $\xi_1 = 0{\cdot}47$ and $\xi'_1 = 0{\cdot}1$.

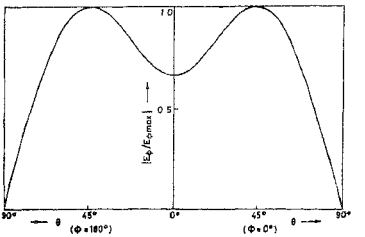

FIG 4b Radiation patterns of MERA for TM_{c110} mode. $\epsilon_r = 10$, F = 10 GHz, $\xi_0 = 1{\cdot}10$, $\xi'_0 = 1{\cdot}30$, $\xi_1 = 0{\cdot}47$, and $\xi'_1 = 0{\cdot}1$.

MERA is designed using standard mode charts given by Sharma[3] and Kretzschmar[4]. Numerical computations of the radiation patterns for TM_{c110}, TM_{s110}, TM_{c210} and TM_{s210} are carried out. Figure 4 is one typical radiation pattern.

2.3. *Input impedance*

Expressions for the input impedance of microstrip elliptical ring antenna have been derived employing a parallel RLC circuit model. The resonant resistance

$$R_0 = \frac{1}{G_0} = \frac{V^2}{2P_T} \tag{8}$$

$$V = E_{z(\xi = \xi_d')} \times h \tag{9}$$

$$f_{\text{res}} = \frac{1}{2\pi\sqrt{LC}} \tag{10}$$

and

$$Q_T = R_0\sqrt{C/L} \tag{11}$$

where Q_T is the total quality factor

$$Z_{in} = R + jX = \frac{1}{\dfrac{1}{R_0} + j\omega C + \dfrac{1}{j\omega L}} \tag{12}$$

$$P_T = P_r + P_c + P_d \tag{13}$$

where P_r, P_c and P_d represent the power radiated, dissipated at the conducting surfaces and dissipated in the dielectric substrate.

2.4. *Directivity*

$$D = \frac{1/2\ Re\ [E_\theta H_\phi^* - E_\phi H_\theta^*]}{P_r/4\pi r^2} \Big|_{\text{max. w.r.t. } \theta \text{ and } \phi.} \tag{14}$$

2.5. *Radiation efficiency*

$$\eta = \frac{P_r}{P_T} \times 100 \tag{15}$$

neglecting P_c where P_T is the total power accepted by the antenna from the connected transmitter.

3. Conclusions

Based on the investigations carried out on the input impedance, directivity and efficiency of MERA the following observations may be made.

(1) For the TM_{c110} mode, there is a reduction in the resistance at resonance, as the feed point is moved towards the inner periphery of MERA from the outer periphery for alumina substrate ($\epsilon_r = 10$).

(2) It may also be seen that as the dielectric thickness is increased from 0·075 to 0·16 cm and from 0·16 to 0·32 cm for $\eta = 0$ and $\eta = \pi/4$, the resonant resistance and the input impedance increase for the TM_{c110} mode.

It is observed that the dependence of directivity and efficiency with frequency deviates from the expected nature.

References

1. BHAL, I. J AND BHARTIA, P. — *Microstrip antennas*, 1980, p.1 Artech House.
2. MCLACHLAN, N W. — *Theory and application of Mathieu functions*, 1947, p. 170, Clarendon Press.
3. SHARMA, A. K. — Spectral domain analysis of an elliptic microstrip ring resonator, *IEEE Trans.*, 1984, **MTT-32**, 212–218.
4 KRETZSCHMAR, J. G. — The elliptic microstrip ring resonator, in *Proc. Seventh European Microwave Conf.*, Copenhagen, Denmark, Sept. 5–8, 1977, pp 465–469

Thesis Abstract (Ph.D.)

Multicriteria games with applications to two-target game problems by D. Ghose.
Research supervisors: U. R. Prasad and I. S. N. Murthy.
Department: Electrical Engineering.

1. Introduction

Game theory is concerned with the modelling and analysis of decision-making in situations of conflict which arise when many decision-makers (players or agents) attempt to control the behaviour of a system to satisfy their own individual requirements. A particularly important branch of game theory is that of pursuit-evasion differential games[1] which finds application in aeronautics in modelling and analysis of problems of interception of a manoeuverable flight vehicle (the evader) by another flight vehicle (the pursuer). These are called single-target games as only the pursuer possesses a weapon system (modelled as a target set in the state space). An extension of the single-target game is the two-target game in which each player has a target set[2,3]. This model finds application in the analysis of aerial combat encounters between fighter aircraft. In these games, each player has the dual objective of avoiding his opponent's target set while simultaneously bringing the opponent on to his own target set. This provides the motivation for modelling

these games as multicriteria games. However, the literature on game theory has very little to offer in terms of useful solution concepts for multicriteria games. In this work, it is attempted to develop a theory for such games starting from the static matrix games and apply these concepts to the modelling and analysis of two-target differential games.

2. Two-person multicriteria matrix games

A two-person zero-sum multicriteria matrix game (in which each element of the matrix as a vector) is defined and various kinds of solutions for these games are proposed. Existing solution concepts for these games in the literature are those of equilibrium strategies[4] which are based on Pareto optimality and mutual response properties. Here, new solution concepts based on security notions are defined. Pareto saddle-point concept is the most desirable among them. The restricted class of matrix games for which they exist are identified. Pareto optimal security strategies are defined and their existence proved. Necessary and sufficient conditions to obtain these through scalarized games are also established[5]. It is proved that a finite number of scalarizations are sufficient to obtain all the Pareto optimal security strategies of a player. Finally, an additional structure of qualitative outcomes is imposed on the multicriteria matrix game and optimal security strategies of both pure and mixed kind are obtained[5].

3. Two-person *multicriteria continuous-kernel games*

Next, the concept of security is extended to a general two-person nonzero-sum multicriteria continuous-kernel game in which the players have a continuum of strategies. Only pure strategies are considered here. The zero-sum game is treated as a special case of the nonzero-sum game. Different kinds of scalarized games are formulated from the original multicriteria game. These are then used to prove the existence of, and to obtain necessary and sufficient conditions for the determination of, equilibrium, Pareto optimal response and Pareto optimal security strategies for the players

4. Multicriteria differential games and modelling of two-target game problems

After presenting the relevant theory on the security and Pareto optimality aspects of static games, the above ideas are extended to dynamic or differential games. Pareto optimal security, response and equilibrium strategies are defined and sufficient conditions are obtained through scalarization procedures. Next, two-target differential games, which are generalizations of pursuit-evasion games, are modelled as zero-sum multicriteria differential game problems based on the fact that each player has a dual objective of avoiding his opponent's target set and terminating the game on his own target set[6,7]. It is shown that the concepts of Pareto optimality and security are important in choosing winning strategies for players since the opponent, by violating certain threshold levels on individual criteria, can cause an undesirable outcome for the player. The utility of the concept of security is discussed in relation to other existing solution concepts for two-target games which are viewed to be variations of the equilibrium solution concept.

5. Qualitative analysis of two-target games

To establish the fact that the notion of security is important in its own right in two-target games, and not merely because it has been modelled as a multicriteria game, a qualitative analysis of the two-target game is carried out next. Secured outcome regions and secured outcome strategies are unambiguously defined depending on the preference ordering of the four possible outcomes (win for either player, draw, or mutual kill) of the game by the players. It is shown that under certain conditions an initial state can belong to two different secured outcome regions for the two players. Conditions under which the secured outcome regions of the two players match are also presented. A construction procedure, based on the qualitative solution of two single-target games[8], is presented to obtain the secured outcome regions of players, for any pair of preference orderings of outcomes by the players[9].

6. Quantitative analysis of two-target games

Finally, the multicriteria model of the two-target game is reverted to, and the secured draw and mutual kill strategies are defined in terms of the security levels on the individual criterion functions. Strategy

optimization problems are formulated, the solution to which, if they exist, determines the best possible secured outcome strategies for players A number of examples are solved to illustrate the procedure[10].

References

1. ISAACS, R — *Differential games*, 1965, Wiley.
2. GETZ, W M. AND LEITMANN, G. — Qualitative differential games with two-targets, *J. Math. Anal Appl.*, 1979, **68**, 421–430.
3. ARDEMA, M. D , HEYMANN, M. AND RAJAN, N. — Combat games, *J. Optimization Theory Appl.*, 1985, **46**, 391–398.
4. SHAPLEY, L. S. — Equilibrium points in games with vector payoffs, *Nav. Res Logistics Q* , 1959, **6**, 57–61.
5. GHOSE, D. AND PRASAD, U. R. — Solution concepts in two-person multicriteria games, *J. Optimization Theory Appl.*, 1989, **63**, 167–189
6. PRASAD, U R. AND GHOSE, D — Formulation and analysis of combat problems as zero-sum bicriterion differential games, *J Optimization Theory Appl.*, 1988, **59**, 1–24.
7 GHOSE, D. AND PRASAD, U. R. — Multicriterion differential games with applications to combat problems, *Comput Math. Appl.*, 1989, **18**, 117–126.
8 SHINAR, J. AND DAVIDOVITZ, A — Unified approach to two-target game analysis. *Proc. IFAC World Congress on Automatic Control*, Munich, 1987, Vol. 8, pp 65–71.
9. GHOSE, D AND PRASAD, U. R. — Qualitative analysis of secured outcome regions for two-target games, *J Optimization Theory Appl.*, 1991, **68**, 233–255.
10. GHOSE D. AND PRASAD, U. R. — Analysis of security strategies for a two-target game, *Proc AIAA Conf. on Guidance, Navigation and Control*, Boston, 1989, pp 1416–1421.

Thesis Abstract (Ph.D.)

Effect of surface roughness on the prebreakdown and breakdown phenomena in SF_6 and its mixtures by Mohammed Mustafa Khan.
Research supervisor: R. S. Nema.
Department: High Voltage Engineering.

1. Introduction

When compressed SF_6 gas was first introduced as an electrical insulant in high-voltage equipment, it was found that the insulation strength of the system was less than what was predicted by theory. An explanation for this apparent reduction in the dielectric strength of compressed SF_6 gas can be given by considering perturbations of the macroscopic electric field produced either by roughness of the electrode surface or by protrusions. The reduction in breakdown voltage depends on protrusion's shape, size, gas and gas pressure. It is, therefore, essential to investigate these effects. In this work, the effect of protrusion on the dielectric strength of SF_6, $SF_6 + N_2$ and $SF_6 + CO_2$ mixture in uniform field is studied at different gap spacings and gas pressures in the sub-atmospheric range so that a comparison is possible in this regard.

2. Results and discussion

2.1. *Breakdown voltage*

It is to be noted that no corona is observed prior to breakdown in both with and without protrusion. The measured breakdown voltages in the absence of protrusion agree well with the calculated values by NKH formula. It is, therefore, clear that the Paschen's law holds good in the experimental range in every gas and mixture studied with uniform field in the absence of any protrusion.

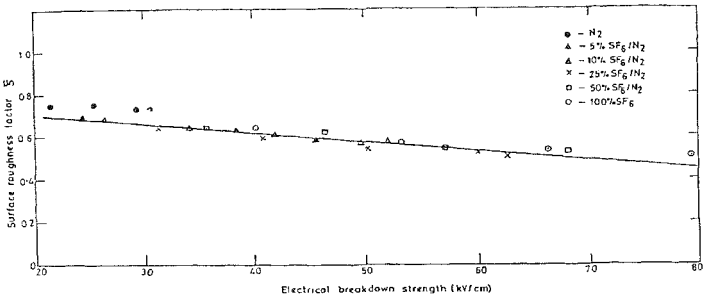

FIG. 1 Plot of surface roughness factor (0·1 cm hemispherical protrusion) *vs* electrical breakdown strength (in the absence of protrusion) in N_2, SF_6 and SF_6 / N_2 mixtures at 0·7 cm gap.

It is seen that with protrusion, the breakdown voltages are not the same at different pressures for the same pd. Therefore, Paschen's law does not hold good in the presence of protrusion.

There is a large reduction in the dielectric strength of highly electronegative gas SF_6 and its mixtures in the presence of protrusion. It is seen that maximum percentage reduction observed is 50% in the case of SF_6 at 600 Torr in this study. This may be explained by considering the enhancement of the field at the tip of the protrusion, reduction of the gap length and field emission from the protrusion.

2.2. *Surface roughness sensitivity*

A surface roughness factor ξ is used to describe surface roughness sensitivity. The surface roughness factor is defined as the ratio of breakdown voltage level measured in the pressure and in the absence of protrusion.

Data obtained have been converted to determine the surface roughness sensitivity of gases and mixtures at different pressures and gap spacings for SF_6, SF_6 + N_2 and SF_6 + CO_2.

Calculated and measured values of surface roughness factor are found to agree reasonably well. Surface roughness factor has been calculated from Pedersen's formula[1] which is given below

$$PR_{max} = (K\sqrt{K}) / [1 - 3\,(^1/_4\,\xi\sqrt{1-\xi^2})^{3/2}]$$

where P is Pressure, R_{max}, Maximum protrusion height, and K, 18 and $\bar{K}$, 24·24/Kpa-cm or 2460/bar-cm.

Figure 1 is plotted to illustrate the results between surface roughness factor and the electrical breakdown strength of SF_6 and its mixtures with N_2. Similar results have been obtained for SF_6 + CO_2 also. It is observed that the uniform field breakdown strength is the most influencing factor in the reduction of breakdown strength with protrusion[2].

References

1. PEDERSEN, A. The effect of surface roughness on breakdown in SF_6, *IEEE Trans*, 1975, **PAS–94**, 1749–1754.

2. NEMA, R. S., KULKARNI, S. V. AND HUSAIN, E. On calculation of breakdown voltages of mixtures of electron attaching gases, *IEEE Trans.*, 1982, **EI–17**, 434–446.

Thesis Abstract (Ph.D.)

Studies on the pre-breakdown and breakdown phenomena in binary and ternary gas mixtures containing SF_6 and CCl_2F_2 by G. R. Venkateshaiah.
Research supervisor: M. S. Naidu.
Department: High Voltage Engineering.

1. Introduction

Gases and gaseous plasmas find a wide variety of applications in gas-discharge lasers, thermonuclear devices and as gaseous insulating/arc-quenching medium in electrical power systems. Electronegative gases of high dielectric strength such as SF_6, CCl_2F_2 and perfluorocarbons are extensively used. Such gases are expensive and sometimes produce toxic and corrosive byproducts. Also, the working conditions vary significantly with regards to thermal conductivity, condensation temperatures, pollution, field nonuniformities, etc. Optimum solution lies in tailoring suitable gas mixtures by admixing electronegative gases with low-cost buffer gases like N_2, CO_2, air, etc., forming binary and ternary gas mixtures.

Although a fair amount of data is available on the breakdown strength of some of the multicomponent gas mixtures, at high pressures, very little information is available on the fundamental physical processes that occur prior to breakdown. The present investigation is aimed at accurate determination of the swarm coefficients for ionization and electron attachment (α/p, η/p), critical E/p (E/p at which $\alpha = \eta$) over the range $100 \leq E/p \leq 240$ V cm^{-1} Torr^{-1} and also the sparking potentials V_s over the range $2 \leq Pd \leq 50$ Torr-cm. (near Paschen's minimum) in the mixture of gases ($SF_6-CCl_2F_2$, N_2-CO_2, SF_6-CO_2, $CCl_2F_2-CO_2$, $SF_6-CCl_2F_2-N_2$, $SF_6-CCl_2F_2-CO_2$ and $SF_6-N_2-CO_2$) using Townsend's steady-state technique. The data in ternary gas mixtures have been obtained for the first time.

2. Experimental apparatus and procedure

Ionization experiments and dc-breakdown voltage measurements have been carried out using Townsend's steady-state technique. Uniform field electrodes of Rogowski profile with provision to vary the gap distance up to 30 mm have been used in this study Binary gas mixtures were prepared by the multiple dilution technique whereas the ternary gas mixtures were prepared by the method of partial pressures to an accuracy of ± 1·0%. The coefficients α and η are measured to an overall accuracy of ± 3·0% and the breakdown potentials to an accuracy of ± 0·5%.

3. Results and discussion

3.1. *$SF_6-CCl_2F_2$ mixtures*

Critical E/p [$(E/p)_c$ at which $\alpha = \eta$ below which sparking should not occur in gases/gas mixtures] obtained in the present study and derived from the ionization experiments is shown in Fig. 1, together with the data of Wotton *et al*[1,2] and Somerville *et al*[3], derived from the measured breakdown voltages (V_s) and those of Frechette[4] obtained from the ionization experiments. α/p, η/p, and $(E/p)_c$ exhibit a characteristic nonlinearity with the addition of CCl_2F_2 to SF_6 over the entire range of E/p studied. The results of Wootton *et al*[4] and Somerville *et al*[3] display a continuous increase in $(E/p)_c$ with the addition of CCl_2F_2 to SF_6 up to about 80% and then decrease to that of pure CCl_2F_2. The present results and those of Frechette[4] indicate a slight decrease in $(E/p)_c$ with the addition of small concentrations of CCl_2F_2 (up to 20%) and then increase to a maximum value at around 70% which is about 6 to 9% lower than the $(E/p)_c$ values obtained from the breakdown test results. The differences in $(E/p)_c$ may be due to different electrode geometry and Pd range adopted by different workers. The positive synergism exhibited by the mixtures may be attributed to the increase in the attachment rate assisted by large vibrational excitation cross-section of CCl_2F_2 and consequential modifications in the electron energy distribution in the mixtures from those for pure gases.

Measured sparking potentials (V_s) in SF_6, CCl_2F_2 and CCl_2F_2–SF_6 mixtures near Paschen minimum ($2 \leq Pd \leq 24$ Torr-cm) determined at low pressures (10–20 Torr) are shown in Fig. 2. It can be observed

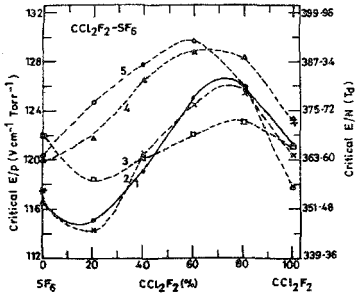

FIG. 1. Critical E/p as a function of percentage CCl_2F_2 in CCl_2F_2–SF_6 mixtures; (—●—) present data; (x) Frechette[4], (□) Frechette and Novak[5], Calculated values; (Δ) Somerville *et al*[5] (o) Wootton *et al*[5].

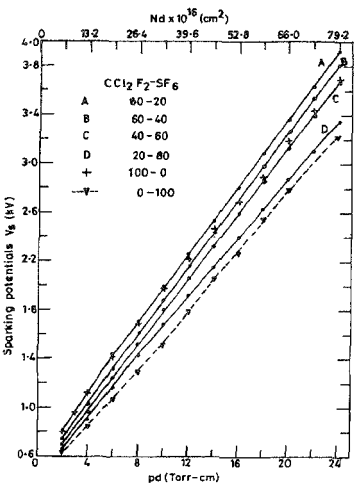

FIG. 2. Sparking potentials (V_s) as a function of Pd (Nd) in CCl_2F_2–SF_6 mixtures

that V_s increases almost linearly with Pd for all mixture ratios. Also, for any given Pd, V_s increases with the addition of CCl_2F_2 to SF_6, similar to what was observed by Wotton *et al*[1,2] and Somerville *et al*[3] for Pd > 60 Torr-cm. V_s of the mixtures containing 60 and 80% CCl_2F_2 can be observed to be always higher than those of pure SF_6 and CCl_2F_2. The data of V_s in these mixtures clearly establishes the positive synergistic behaviour observed in the ionization experiments.

Similar investigations carried out in the binary mixtures of N_2–CO_2, SF_6–CO_2 and CCl_2F_2–CO_2 demonstrated that CO_2 is also an excellent buffer gas comparable to or even better than N_2, which can be mixed with electron-attaching gases. CO_2 exhibited efficient electron slowing-down property in the mixtures with SF_6 and CCl_2F_2. Addition of small percentages (20–30%) of SF_6 or CCl_2F_2 increased the dielectric strength of CO_2 considerably (30–40%).

3.2 *SF_6–CCL_2F_2–N_2 Mixtures*

α/p and η/p are experimentally determined in about 22 combinations of the ternary gas mixtures in which each component gas is varied from 0 to 100% over the range $100 \leq E/p \leq 240$ V cm^{-1} Torr^{-1}. The α/p and η/p characteristics exhibited nonlinear variations with the addition of CCl_2F_2 to SF_6–N_2 mixtures. The degree of nonlinearity was observed to decrease with the addition of more and more N_2 into the mixtures. This was attributed to be due to the ionization of CCl_2F_2 by metastables of N_2 and increase in the electron mean energies of the swarm with the addition of small concentrations of CCl_2F_2 ($\leq$ 20%).

$(E/p)_c$ obtained from α/p and η/p characteristics in ternary gas mixtures is shown in Fig. 3, together with the theoretical values of Frechette et al[5] (full lines) and the values obtained from the measured V_s

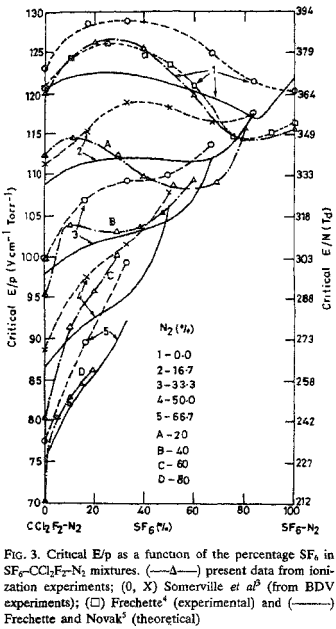

FIG. 3. Critical E/p as a function of the percentage SF_6 in SF_6–CCl_2F_2–N_2 mixtures. (—Δ—) present data from ionization experiments; (0, X) Somerville *et al*[3] (from BDV experiments); (□) Frechette[4] (experimental) and (———) Frechette and Novak[5] (theoretical)

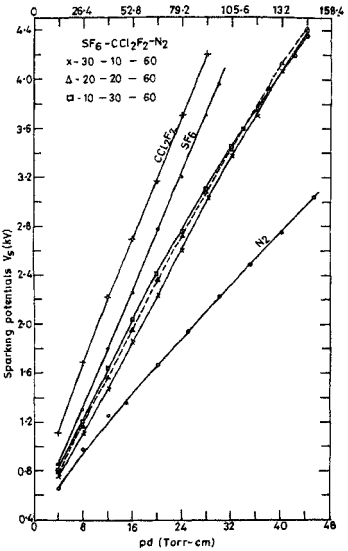

FIG. 4. Sparking potentials (V_s) as a function of Pd (Nd) in SF_6–CCl_2F_2–N_2 mixtures.

by Somerville *et al*[3] (dashed lines). Each curve represents a fixed N_2 concentration like 0, 20, 40, 60 and 80%. It can be observed that the degree of nonlinearity in the characteristics decreases with the increase in the concentration of N_2 in the mixtures.

Maximum $(E/p)_c$ of 126 occurs at 25% SF_6 concentration of SF_6–CCl_2F_2 mixtures, whereas peak values of 114 and 104 occur at around 10% SF_6 in the ternary mixtures containing 20 and 40% N_2, respectively. Characteristic nonlinearities in the mixtures may be due to modifications in the electron energy distribution from those of pure gases which vary according to the percentage concentration of the component gases and, as also E/p. In addition, the efficiencies of ionization and attachment are dependent upon the electron energy distribution in the mixtures.

Sparking potentials (V_s) measured in a few selected mixture ratios of practical importance (10–30–60, 20–20–60, and 30–10–60) in SF_6–CCl_2F_2–N_2 mixtures over the range $4 \leq Pd \leq 50$ Torr-cm are shown in Fig. 4, together with the data in pure gases SF_6, CCl_2F_2 and N_2 for comparison. It can be observed that although V_s of the mixtures is lower than those of pure gases of SF_6 and CCl_2F_2, the breakdown strength of N_2 is increased considerably (10 to 50%) over the range of Pd studied. From the breakdown test results of Wootton *et al*[1,2] such mixtures were found to be economically viable in CGIT systems while possessing about 87% of the dielectric strength of pure SF_6.

Similar investigations have been carried out in SF_6–CCl_2F_2–CO_2 and SF_6–N_2–CO_2 mixtures. From the results it can be observed that CO_2 has performance comparable to N_2 as a buffer gas (electron slowing-down gas). α/p, η/p, $(E/p)_c$ exhibited characteristic nonlinearities which decrease with higher concentrations of CO_2 in the mixtures.

4. Conclusions

The present study clearly demonstrated the existence of positive synergism for higher concentrations of CCl_2F_2 in SF_6 (greater than 20%). Addition of small concentrations of SF_6 or CCl_2F_2 (about 40%) to buffer gases N_2 or CO_2 increased the dielectric strength of the binary mixtures equal to 80 to 90% of that for pure SF_6, thus making them economically viable. Ternary gas mixtures exhibit nonlinear synergistic behaviour for different mixture ratios with respect to ionization, attachment and sparking potentials which decreases at higher concentrations of buffer gases. From the considerations of critical E/p optimum mixture ratios suggested are: $SF_6(10\%)$–$CCl_2F_2(50\%)$–$N_2(40\%)$; $SF_6(10\%)$–$CCl_2F_2(40\%)$–$CO_2(50\%)$ and $SF_6(20\%)$–CO_2 (20%)–$N_2(60\%)$ for insulation purposes.

References

1 WOTTON, R. E., DALE, S. J. AND ZIMMERMAN, N. J. — Electric strength of some gases and gas mixtures, *Proc. 2nd Int. Conf. on Gaseous Dielectrics*, USA, 1980, Vol. II, pp 137–148.

2 WOOTTON, R. E. — *Gases superior to SF_6 for insulation and interruption*, EPRI Report, 1982, No. EI-2602

3. SOMERVILLE, I. C., TEDFORD, D. J AND THURGOOD, A. — Automatic measurement of spark breakdown potential in gas mixtures, *6th Int. Conf. on Gas Discharge*, London, 1980, pp 271–274

4. FRECHETTE, M. F. — Experimental study of SF_6/N_2 and SF_6/CCl_2F_2 mixtures by the steady-state Townsend method, *J. Appl. Phys.*, 1986, **59**, 3684–3693.

5. FRECHETTE, M. F. AND NOVAK, J. P. — Boltzmann-equation analysis of electron transport properties in $CCL_2F_2/SF_6/N_2$ gas mixtures, *J. Phys. D Appl. Phys.*, 1987, **20**, 438–443.

Thesis Abstract (Ph.D.)

Developmental studies on ion thrusters for satellite propulsion by M. H. Balakrishnaiah.
Research supervisor: G. R. Nagabhushana.
Department: High Voltage Engineering.

1. Introduction

Geosynchronous satellites are widely used in many important applications such as communication, weather forecast and geological survey. The orientation of these satellites in orbit is subject to many gravitational fields and therefore changes gradually. However, the orientation is quite critical in most applications and must be maintained within $\pm$ 0·1° between the orbital and equatorial plane of the satellite. It is estimated that changes due to gravitational fields are in the range of 0·9° per year thus requiring correction once in 40 days. Presently, conventional hydrazine thrusters are being used for such corrections. Nearly 100 kg of fuel is required for a life of 10 years.

Ion thrusters can be used in place of conventional thrusters for finer correction bringing down the propellant consumption to just 10 kg.

The 'electron-bombardment ion thruster' originally developed by Kaufman[1], using mercury as the propellant, has been used extensively. Its advantages over other existing chemical and electrical thrusters are:

(i) high specific impulse, (ii) low volume of mercury for a given mass, and (iii) high efficiency. The present work was therefore directed towards developmental studies on electron bombardment ion thrusters with mercury as the propellant.

2. Principle of operation and present work

In this type of thrusters, mercury is vapourised at a desired rate and the vapours pass into a hollow cathode where a discharge is maintained to produce partially ionised mercury vapour. The partially ionised vapour is then distributed into the main plasma chamber with the help of a baffle. In this chamber, the electrons are subjected to crossed electric and magnetic fields so that they travel in helical paths towards the anode and cause a high degree of ionisation of the neutral mercury vapour. A screen and accelerator grid combination (having numerous aligned aperatures) extract the ions and accelerate them into space thereby giving rise to a reaction thrust on the satellite.

To maintain electrical neutrality of the satellite, the ejected ion beam is neutralised by electrons from another hollow cathode discharge.

The present work involved the following:

(i) Preliminary design and fabrication of an ion thruster for a nominal thrust of 10 mN.

(ii) Design and fabrication of a mercury flow meter and vapouriser.

(iii) Establishing the mercury vapouriser characteristics in terms of heater input and mercury flow rate.

(iv) Establishing the current-voltage characteristics of a hollow cathode. This involved studies of the influence of:
   (a) mercury vapour flow rates ranging from 18 to 30 mg/min,
   (b) cathode tip temperatures in the range of 900 to 1200°C,
   (c) discharge currents in the range of 1 to 2 Å, and
   (d) magnetic fields 30 to 70 Gauss.

(v) Study of the mercury vapour plasma in static condition in terms of number density and energy of electrons as a function of
   (a) mercury flow rate,
   (b) discharge current, and
   (c) magnetic field.
   The range of these parameters is already indicated in (iv) above.
   The study was carried out by obtaining the voltage current characteristic of a simple Langmuir probe.

(vi) Establishing an ion beam with a current of 160 mÅ (design value being 157 mÅ for 10 mN) with the use of another hollow cathode as a neutraliser.

(vii) The thrust developed was measured using an eddy current probe. During this measurement, the thruster was mounted on a four-legged stand (the legs being designed for critical loading) that would deflect because of the thrust. The deflection was calibrated using a strain gauge and a linear variable differential transducer. Thrust measurement was carried out (using the eddy current probe) for different mercury flow rates, discharge currents, magnetic fields and acceleration potentials.

(viii) A 127° electrostatic analyser was designed, fabricated and used for studying the energy distribution of the ions in the ion beam for different
   (a) flow rates of mercury,
   (b) main discharge currents,
   (c) magnetic fields, and
   (d) acceleration voltages.

3. Results and discussion

The hollow cathode was found to operate satisfactorily with the keeper discharge current in the range of 0·1 to 1·5 Å, the keeper discharge voltage being in the range of 8 to 14 V. The discharge-initiation voltage was dependent mainly on mercury flow rate and the cathode tip temperature and was in agreement with the results of other workers[2].

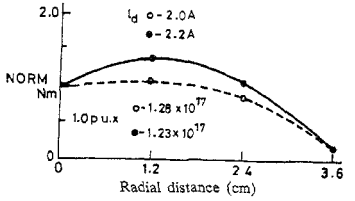

FIG. 1. Spatial density distribution of electrons

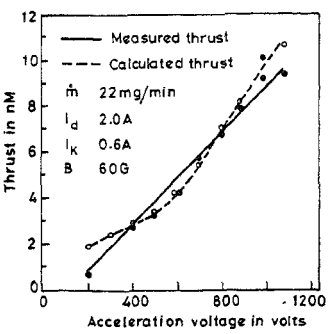

FIG. 2. Measured and calculated thrust as a function of ion acceleration voltage

The number desnity of electrons in the main plasma chamber was calculated based on Langmuir's theory and found to be in the range of 7–8×10^{17} per m^3 and 1–2×10^{17} per m^3 at baffle and screen, respectively. The spatial density distribution at grid is shown in Fig. 1. This is in agreement with the results of Strickfaden and Geiler[3]. The number density of ions calculated using Bohm's criterion[4] and orbital theory[5] agree well with the above values. The electron energy distribution was found to be non-Maxwellian consisting of a Maxwellian group of electrons with low energies—1·5 to 2 eV near the baffle and 1 to 2 eV near the screen grid—and a group of primary electrons with high energy—34 eV near the baffle and 15 eV near the screen, respectively.

Ions were extracted by applying an appropriate voltage and were neutralised by electrons from another hollow cathode. Under dynamic condition, the thruster produced 10 mN thrust with an ion beam current of 160 ma for a main discharge current of 2 Å at 35 V and acceleration potential of 1000 V, when the mercury flow rate was 22 mg/min, and keeper current of 0·6 Å at 14 V. The thrust measured using eddy current probe was in close agreement with the thrust computed using beam parameters (Fig. 2).

The 'analyser constant' of the electrostatic analyser[6] built was determined both theoretically (*i.e.*, from the dimensions) and experimentally. They were found to agree very closely. The studies with the analyser gave the following results.

(i) Variation of energy distribution along a radius indicated that uniform thrust was developed over the total area of the aperture of the thruster.

(ii) The energy distribution of the ions is nearly monoenergetic for different mercury flow rates (Fig. 3).

(iii) The current in the main discharge had a linear relationship with the thrust.

Since the thruster is a multiparameter device the analyser can be used to study the performance of the thruster.

During these studies, only two cathodes were used and were exposed to atmospheric air nearly 100 times to make necessary changes in the system. The total duration of operation is estimated to be more than 1000 hours. In the absence of such frequent exposure to air (oxygen), the life would be much higher. Therefore, it is believed that thrusters using the above construction would be useful for North–South station-keeping of geosynchronous communication satellites.

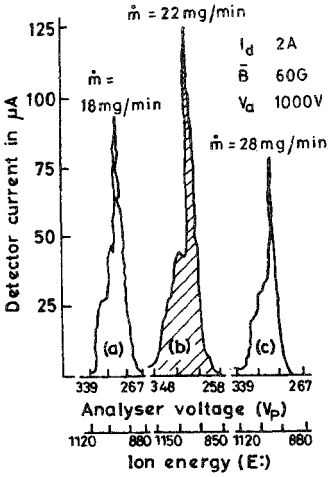

FIG. 3. Ion energy distribution characteristics for different mercury flow rates.

References

1. KAUFMAN, H. R. — Origin of the electron-bombardment ion thruster, *J. Spacecraft Rockets*, 1981, **18**, 289–292.
2. FEARN, D. G. AND PHILIP, C. M. — An investigation of physical processes in a hollow cathode discharge, AIAA, *9th Elect. Propulsion Conf*, Bethesda, April 1972.
3. STRICKFADEN, W. B. AND GEILER, K. L. — Probe measurements of the discharge in an operating electron bombardment engine, *AIAA J.*, 1963, **2**, 1815–1823.
4. BOHM, D. — Characteristics of electrical discharges in magnetic fields, (ed., A. Guthrie and R. K. Wakerling), Ch 3, 1949, McGraw-Hill.
5. CHEN, F. F. — Saturation ion currents to Langmuir probes, *J. Appl. Phys.*, 1965, **36**, 675–678.
6. FHADIL, H. A. *et al* — Energy distribution of atmospheric ions drifting in rare gases, *Int. J. Mass Spectrosc. Ion Processes*, 1985, **65**, 307–319.

Thesis Abstract (Ph.D.)

Effect of foundry variables on structure and properties of investment cast nickel base superalloy PK 24 (IN 100) by H. S. Chandraseckariah.
Research supervisors: S. Seshan and S. G. A. Pasha (orgn)
Department: Mechanical Engineering.

1. Introduction

Research and development activities on materials for high-temperature applications have led to a new

Table I

Specified composition of PK 24 (IN 100)

Sl no	Element		Units	Specifications	
				Min	Max
1	Carbon	C	%	0·15	0·20
2	Silicon	Si	%	–	0·20
3	Manganese	Mn	%	–	0·20
4	Sulphur	S	%	–	0·015
5	Silver	Ag	ppm	–	0·0005
6	Aluminium	Al	%	5·0	6·0
7	Arsenic	AS	ppm	–	–
8	Boron	B	%	0·01	0·02
9	Bismuth	Bi	ppm	–	–
10	Cadmium	Cd	ppm	–	-
11	Cobalt	Co	%	13·00	17·00
12	Chromium	Cr	%	8·00	11·00
13	Copper	Cu	%	–	0·20
14	Iron	Fe	%	–	1 00
15	Gallium	Ga	ppm	–	–
16	Hafnium	Hf	%	–	–
17	Indium	In	ppm	–	–
18	Magnesium	Mg	ppm	–	–
19	Molybdenum	Mo	%	2·00	4·00
20	Nitrogen	N2	ppm	–	–
21	Nb + Ta		%	–	0·25
22	Nickel	Ni	%	–	bal
23	Oxygen	O_2	ppm	–	–
24	Lead	Pb	ppm	–	0·0015
25	Antimony	Sb	ppm	–	–
26	Selenium	Se	ppm	–	–
27	Tin	Sn	ppm	–	–
28	Tantalum	Ta	%	–	–
29	Tellurium	Te	ppm	–	–
30	Titanium	Ti	%	4·50	5·00
31	Thallium	Tl	ppm	–	–
32	Vanadium	V	%	0·70	1·20
33	Tungsten	W	%	–	0·20
34	Zinc	Zn	ppm	–	–
35	Zirconium	Zr	%	0·03	0·09

class of materials known as superalloys. Broadly, such superalloys fall under the categories of cobalt-, iron- and nickel-base superalloys. Of the above, nickel-base superalloys are more suitable for higher temperature applications. The initial developments in nickel-base superalloys were through enhanced alloying. However, beyond a particular level of addition, enhancement in properties is possible only through improvements in processing. Single-crystal approach, rapid solidification and mechanical alloying do represent feasible routes, but such sophisticated techniques are economically unsuitable for the production of majority of the superalloy components for industrial applications. On the other hand, vacuum investment casting method has been accepted as a satisfactory processing technique for superalloys.

Adequate literature is available pertaining to the effect of various alloying elements on the structure and mechanical properties of investment-cast nickel-base superalloys, but data on the influence of the mould variables and other processing variables are rather meagre. Likewise, hardly any information is available on the casting characteristics of nickel-base superalloys cast in investment shells. Realizing the need for the generation of such vital information for the most popular nickel-base superalloy PK 24 (IN 100), a systematic investigation was completed. Salient details of the experimental investigation and the findings are given here.

2. Experimental details

This investigation was on the nickel-base superalloy PK 24 (IN 100) which contains many major and minor alloying elements, apart from a number of carefully controlled trace elements. Specified composition of the alloy is given in Table I. The investment casting test tree was very carefully designed to consist of test specimens for the study of different mechanical properties and microstructural aspects. Assembled wax tree was invested in the refractory slurry (fused silica + ethyl silicate) and stuccoed to form the shell.

Melting of IN 100 (PK 24) was carried out in a medium-frequency, double-chamber, vacuum-induction furnace. At various predetermined temperatures of the molten metal and the investment mould, and

maintaining different preselected vacuum levels, test castings were made. From the solidified casting tree, individual test specimens were separated and used for the study of surface finish, foundry characteristics, microstructural aspects and mechanical properties.

3. Conclusions

The findings of the investigation were analysed systematically to study the influence of casting variables, *viz.*, (a) pouring temperature, (b) mould temperature, (c) level of vacuum, and (d) number of shell coats on the above-mentioned properties of PK 24 (IN 100) test castings made through vacuum-investment casting process.

a. *Surface finish of castings*

A general inference is that conditions conducive for increased chilling of metal at the metal-mould interface result in improved surface finish of the casting.

b. *Foundry characteristics*

(i) *Metal mould equilibrium temperature (MME temperature):* MME temperature is of importance in controlling the solidification and hence the final structure and properties. Mould temperature and pouring temperature have marked influence on MME.

(ii) *Fluidity:* Individual processing variables do affect the fluidity but the combined effect of two or more variables on fluidity is much higher.

c. *Microstructure*

(i) *Microporosity:* Higher vacuum levels result in minimal microporosity, and increased section thickness leads to higher levels of micropores.

(ii) *Grain size:* Higher pouring temperatures, higher vacuum levels and thicker section size result in larger grain size. As the grain size influences all the properties, selection of optimum processing variables based on the above considerations is very essential.

(iii) *Dendrite arm spacing:* The variation of DAS follows a trend similar to that of grain size.

(iv) *Eutectic volume fraction and carbide volume fraction.* The variation of these with the processing variables is very marginal.

(v) *Secondary gamma prime morphology:* Secondary gamma prime phase plays a vital role in the high-temperature strengthening of nickel-base superalloys TEM studies on the alloy investigated revealed that increased heat inputs in terms of pouring temperature and mould temperature result in reduced particle size.

d. *Mechanical properties*

Hardness values change very little when process variables are altered. The variations in mechanical properties closely follow variations in microstructural characteristics, *viz.*, grain size, DAS and micro porosity. High-temperature UTS is a very important consideration for this alloy (PK 24 (IN 100)). Values of UTS at the elevated temperatures do get influenced by process variables and conform to standard specifications. Microstructural constituents, in particular the secondary gamma prime particles, exert a marked influence on the high-temperature UTS value.

As a turbine blade material, this alloy is required to have satisfactory stress rupture properties. It has been found possible to enhance the stress rupture life through judicious selection of the process variables. Empirical relationships have been derived connecting all the process variables with each one of the properties, thus enabling the prediction of any property corresponding to a set of variables employed.

It is concluded that the process variables studied, *viz.*, pouring temperature, mould temperature, vacuum level and the number of shell coats have varying influence on the microstructure and hence the properties of investment-cast, nickel-base superalloy Nimocast PK 24. A judicious selection of the variables is essential and possible in order to realise the optimum properties.

References

1. DESFORGES, C. D. — Metals and alloys for high-temperature applications: current status and future prospects, *Source book on materials for elevated temperature applications*, (ed. Bradley, E. F), 1979, pp 1–18, ASM Metals Park, Ohio 44073, USA.

2. DARDI, L. E., DADAL, R. P. AND YAKER, C. — Metallurgical advancements in investment casting technology Advanced high temperature alloys: processing and properties. *Proc Nicholas J. Grant Symp. on Processing and Properties of Advanced High Temperature Alloys*, (ed. Allen, S. M., *et al*), 1986, pp 25–39, ASM, Metals Park, Ohio 44073, USA.

3. YUKAWA, N., MURATA, Y. AND NODA, N. — Analysis of solidification behaviour and alloy design of a nickel-base superalloy IN 100, *Superalloys 1984, Proc Fifth Int. Symp. on Superalloys* (ed., Gell, M. *et al*), 1984, pp 83–92, The Metallurgical Society of AIME, Warrendale, PA 15086

4. HOLT, R. T. AND WALLACE, W. — Impurities and trace elements in nickel-base superalloys *Int. Metals Rev.*, 1976 **21**, (Review 203), 1–24.

5. SULLIVAN, C. P AND DONACHIE, M. J. JR — Some effects of microstructure on the mechanical properties of nickel-base superalloys *Source book on materials for elevated temperature applications*, (ed., Bradley, E. E), 1979, pp 250–259, ASM, Metals Park, Ohio 44073, USA.

6. THOMAS, G. B. AND GIBBONS, T. B. — Creep and fracture of a cast Ni–Cr-base alloy containing trace elements, *Mater Sci Engng*, 1984, **6**(1), 13–23.

7. OUICHOU, L., LESSOULT, G., LAMANTHE, G., HAMAR, R., THERET, J. M. AND BACHELET, E. — Microporosity formation in investment castings of nickel-base superalloys: Metallurgical effects, thermal modelling and foundry assessment, *High-temperature alloys for gas turbine* (ed., Brunetaud, R. *et al*), 1982, pp 955–971, D. Reidel.

Thesis Abstract (Ph.D.)

An efficient three-dimensional finite-element analysis of simple and extended tube expansion chamber mufflers by A. D. Sahasrabudhe.
Research supervisors: M. L. Munjal and S. Anantha Ramu.
Department: Mechanical Engineering.

1. Introduction

Exhaust noise of internal combustion engines has been a major source of traffic noise. Hitherto, the design and analysis of reactive muffler components has been based on simple one-dimensional analysis using transfer matrix method. However, commercial mufflers require three-dimensional (3D) analysis in the frequency range of interest owing to the propagation of higher order modes. Out of the various methods of 3D analysis, finite element (FEM) is the most attractive[1]. A real 3D finite-element model requires several hundreds of nodes resulting in tedious data preparation and solution of a large number of simultaneous equations. Therefore, previous researchers have generally restricted themselves to 1, 2D or axisymmetric 3D analyses with simplifying assumptions. In the present work, finite-element formulation of an acoustic problem has been done by two well-known methods, *viz.*, the variational method and the Galerkin weighted residual method. A finite-element computer program has been developed incorporating special solution techniques. A preprocessor computer program has also been developed to handle input data preparation. Program is then used for a truly 3D analysis of reactive muffler components like simple and extended tube expansion chambers and sudden area discontinuities.

2. Results and discussion

The selection of suitable element shape functions is an important aspect of the finite-element analysis. For

a linear wave propagation, which is a second-order partial differential equation, C^1 continuity model is desired. In this model, continuity of pressure and its three spatial derivatives have to be ensured. In the present work, 8-noded hexahedral elements with Hermitian shape functions are used for the C^1 continuity model, while isoparametric quadratic (20-noded brick and 15-noded prism) elements are used assuming C° continuity model. The results obtained in the form of transmission loss (TL) by both these models tally very well indicating the adequacy of C° continuity in which continuity of pressure alone is ensured (*see* Fig. 1). It has been observed that using the C^1 continuity model and Hermitian element[2],

$$\text{typical finite-element dimension} \leqslant 0{\cdot}2\ \lambda_{min}. \tag{1}$$

The use of C° continuity model and quadratic elements leads to

$$\text{typical finite-element dimension} \leqslant 0{\cdot}52\ \lambda_{min}. \tag{2}$$

Thus, C° continuity with higher order elements requires less number of nodes in modelling, which increases computational efficiency and hence should be preferred to C^1 continuity.

Two special solution techniques, *viz.*, matrix condensation[3] and transfer matrix techniques[4] have been developed making use of recursive substructuring principle to reduce the core memory and CPU time requirements substantially. The saving in core memory and CPU time by using these efficient techniques with $m = 2$ (2^m segments) in comparison to full FEM model is of the order of 35 and 64%, respectively. For large systems, with $m \geqslant 3$, the efficiency is enhanced further.

These special techniques have then been used for the 3D analysis of simple and extended tube expansion chambers and the results are found to corroborate with the experimental and analytical results available in literature. The effect of expansion ratio, length of the chamber, lengths of the extended tubes, radial and offset locations of the inlet/outlet tubes have been investigated and certain design criteria have been established. A couple of them are as follows.

(i) An approximate relation for the l/d ratio required to achieve the plane-wave behaviour up to a frequency kl ($= n\pi$) has been obtained as

$$\left(\frac{1}{d}\right)_{n\pi} = 2\left(\frac{1}{d}\right)_{(n-1)\pi} - \left(\frac{1}{d}\right)_{(n-2)\pi}, \tag{3}$$

where the suffix denotes the frequency kl, for $n \geqslant 3$,

$$\left(\frac{1}{d}\right)_{\pi} = 0{\cdot}65, \text{ and}$$

$$\left(\frac{1}{d}\right)_{2\pi} = 1{\cdot}0.$$

(ii) For a given area of the expansion chamber, the circular shape is best suited for delaying the onset of higher order modes.

(iii) The performance of extended tube expansion chambers is better compared to their simple expansion chamber counterparts. The extended length of the inlet and outlet tubes being responsible for the creation of resonant end chambers, suitable values may be chosen for them to achieve better performance in the desired frequency bands. In fact, with the extended inlet and outlet tube lengths (l_{ei} and l_{eo}) as per the following equations

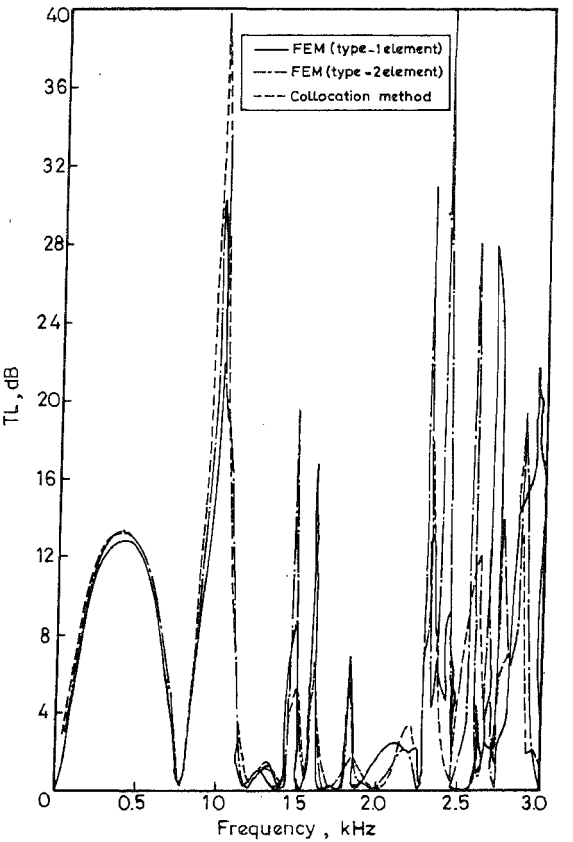

FIG. 1. TL of an offset-inlet offset-outlet rectangular expansion chamber muffler. $b_1 = b_3 = h_1 = h_3 = 0{\cdot}05$m; $b_2 = h_2 = 0{\cdot}15$m; $L_2 = 0{\cdot}0225$ m.

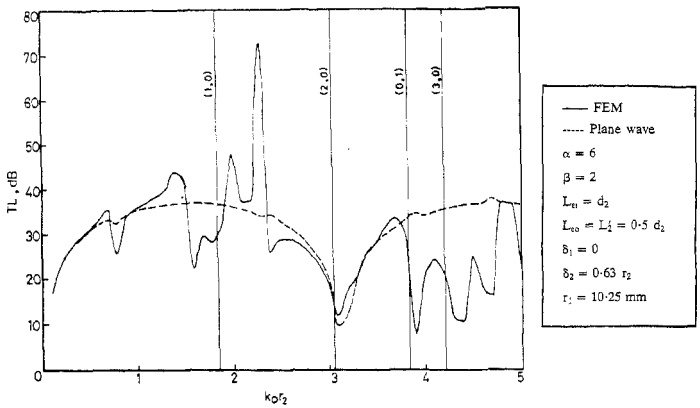

FIG 2 Optimal TL curve of an extended-tube expansion chamber muffler.

$$l_{ei} = 0{\cdot}5\ l_2 \tag{4}$$

$$l_{eo} = 0{\cdot}25\ l_2 \tag{5}$$

where l_2 is the length of the chamber, the resonance peaks cancel three out of every four troughs, thereby widening the high TL frequency band (Fig. 2)

Finally, the 3D finite element analysis has been used to obtain the equivalent transfer matrix of a sudden area discontinuity within the plane-wave frequency limit incorporating the effect of evanescent higher order modes[5]. Using this transfer matrix, accurate and comprehensive expression for the Karal factor (representing the inertive effect of discontinuity) has then been obtained as a function of α (radius ratio), kr_2 (non-dimensional frequency) and δ^* (offset distance). This Karal correction factor is useful in accounting for the inertive effect of discontinuity and hence the accuracy of plane-wave results is ensured right up to the plane-wave limit.

References

1. MUNJAL, M. L. — *Acoustics of ducts and mufflers*, 1987, Wiley.
2. ROSS, D. F. — *J. Sound Vibr.*, 1981, **79**, 133–143.
3. CHRISTIANSEN, P. S. AND KRENK, S. — *J. Sound Vibr.* 1988, **122**, 107–118.
4. LECKIE, F. A. AND PESTEL, E. C. — *Int. J. Mech. Sci*, 1960, **2**, 137–167.
5. PEAT, K. S. — *J. Sound Vibr.*, 1988, **127**, 123–132.

Thesis Abstract (Ph.D.)

Laminar buoyancy-induced flows and transport processes in stratified media by D. Angirasa.
Research supervisor: J. Srinivasan.
Department: Mechanical Engineering.

1. Introduction

In recent years there has been a growing awareness that density-stratification plays a crucial role in determining buoyancy-induced flows and transport processes. The ocean as well as the atmosphere are stratified. Most of the lakes are dense at the bottom and light at the top. Other examples include storage tanks and environmental chambers.

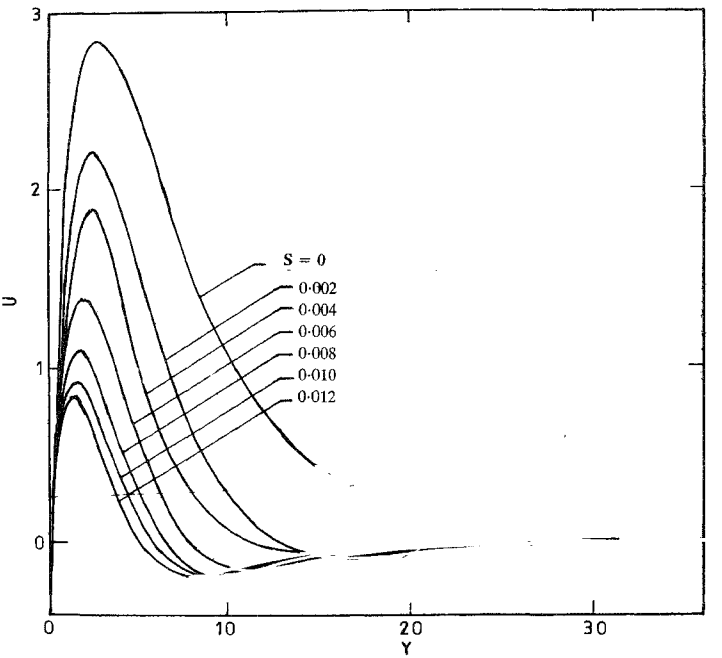

FIG. 1. Velocity profiles at X = 100 for Prandtl number, Schmidt number = 100 and buoyancy ratio = −2 for various values of stratification parameter S.

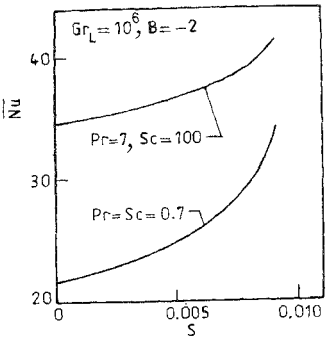

FIG. 2. Average Nusselt number (Nu) for Grashof number of 10^6 and buoyancy ratio of −2 and various Prandtl numbe (Pr), Schmidt number (Sc) and stratification parameters (S).

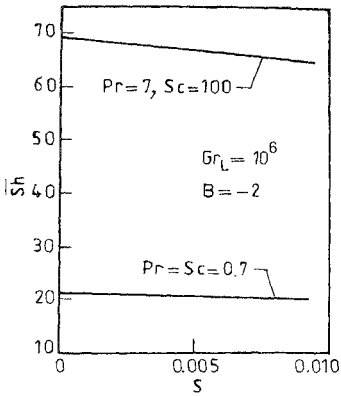

FIG. 3. Average Sherwood number (Sh) for Grashof number of 10^6 and buoyancy ratio of −2 and various Prandtl number (Pr), Schmidt number (Sc) and stratification parameters (S)

In many natural convection flows the buoyancy that drives the flow has more than one component. The buoyancies may aid or oppose one another. Then, the interaction among the multiple buoyancies and stratification is quite complex Very little is known about such phenomena Ostrach[1] recently reviewed the literature on combined buoyancies.

In this work, the role of stable temperature stratification on the flows and transport characteristics has been studied in detail by numerical solution of governing partial differential equations. Thermal buoyancy and the combined buoyancy of heat and mass diffusion are considered.

2. Numerical procedures

For solving boundary-layer type of problems an explicit numerical scheme was employed. For the recirculating flows the alternating direction implicit (ADI) scheme was used. In either case, upwind differencing was employed for convection terms to ensure numerical stability. Detailed discussion of the schemes is given by Roache[2].

3. Results

We first considered laminar natural convection boundary layer flow adjacent to a vertical surface due to the combined buoyancies of heat and mass diffusion in a thermally stratified ambient. The stable ambient thermal stratification is assumed to be linear. It is observed that even for very high levels of thermal stratification, boundary-layer flow is possible provided the buoyancy due to mass diffusion is dominant and aids the vertically upwards thermal buoyancy (Fig. 1). Both aiding and opposing buoyancies were considered, and also the effect of Schmidt number. Nusselt and Sherwood number data are presented for gaseous and aqueous solutions (Figs 2 and 3).

Laminar axisymmetric plumes due to combined buoyancies in a thermally stratified medium was considered next. We found that plumes depart from boundary-layer type of flow for much smaller levels of stratification because of the progressive decay of both buoyancies in the streamwise direction.

Recirculating flows arising due to thermal buoyant convection in a thermally stratified environment were treated next. For high levels of thermal stratification which makes the temperature potential at some height of the plate as zero, we observed horizontal wall plumes which were shown by Chen and Eichhorn[3] in their laboratory flow visualization. We demonstrated that the usual definition of the Nusselt number is not suitable for natural convection in stratified media.

Finally, we considered natural convection flows in square horizontal cavity with the open side exposed to a stable thermally stratified environment. We observed that the number of recirculating zones has increased for the open cavity. Plume instabilities were seen in cavity flows.

References

1 OSTRACH, S — Natural convection with combined driving forces, *Physicochem Hydrodynamics*, 1980, **1**, 233–247

2. ROACHE, P J. — *Computational fluid dynamics*, 1982, Hermosa, Albuquerque

3 CHEN, C C AND EICHHORN, R. — Natural convection from a vertical surface to a thermally stratified fluid, *ASME J. Heat Transfer*, 1976, **98**, 446–451

Thesis Abstract (Ph.D.)

Crystallographic aspects of thermally induced organic solid state reactions by K. Vyas.
Research supervisor: H. Manohar.
Department: Inorganic and Physical Chemistry.

1. Introduction

In recent years, x-ray crystallographic techniques have been widely used in the study of solid-state reactions[1,2]. This is due to the realisation that the rigid crystalline matrix provides an extraordinary spatial control over the initiation and progress of the reaction. Consequently, structural and geometric parameters such as packing and orientation of the reactant molecules, their conformation and the short contacts between reactive centres play a vital role in contrast to the electronic and dipolar effects which are important in solution chemistry. This leads to stereo-selective and stereo-specific products and sometimes to products impossible to realise in solution. It is this 'spatial' or 'topochemical' factor which is of interest to a chemical crystallographer. The structural investigations of the reactants and products of the following thermal solid-state reactions were undertaken to understand the mechanism of the reactions at the molecular level in terms of the topochemical factors. The reactions are:

(i) O- to N-acyl migration in salicylamides (Scheme 1)[3]
(ii) *cis–trans* isomerisation in substituted bi (cyclopentenylidene) derivatives[4] (Scheme 2).

2. Results and discussion

2.1. *O- to N-acylmigration* (Scheme 1)

Two derivatives of the reactants, *viz.*, O-benzoyl and O-propionyl salicylamide (OBZ and OPR) and the corresponding products, *viz.*, N-benzoyl and N-profinoyl salicylamide (NBZ and NPR) were prepared and characterised by spectroscopic methods. Two modifications of OBZ, *viz.*, OBZ4 (4 molecules/unit cell) and OBZ16 (16 molecules/unit cell) in $P2_1/C$ space group were obtained. Their x-ray crystal structures were solved using direct methods and refined by least-squares procedures. The structures of the acetyl derivatives (OAC and NAC) have been solved earlier in our laboratory[5]. Hence, these two structures were also considered for discussion.

Scheme 1.

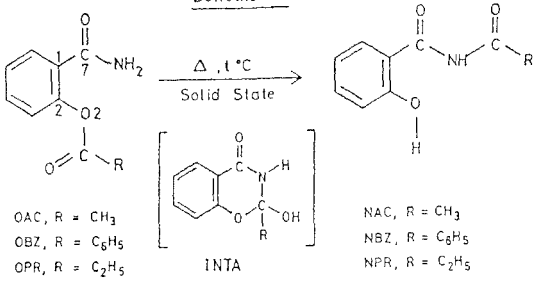

OAC: O-acetyl salicylamide (t ~ 100°c) NAC: N-acetyl salicylamide
OBZ: O-benzoyl salicylamide (t ~ 100°C) NBZ: N-benzoyl salicylamide
OPR: O-propionyl salicylamide (t~ 85°C) NPR: N-propionyl salicylamide

Scheme 1.

The molecules of the reactants are held together by hydrogen bonds. The amide structures were rationalised using the close-packing principles and directional preferences of the N – H · · · O = C bond by Leiserowitz and Hagler[6]. Primary amide molecules form centrosymmetrically related dimers by means of N – H · · · O bonds. These cyclic dimers are interlinked by other N – H · · · O bonds through various motifs. Interestingly, each structure provides an example for each motif, *viz.*, screw axis motif (OAC), translation motif (OBZ4 & OPR), glide motif (OBZ16). The hydrogen bond interactions are also depicted in terms of graph-set notations proposed by Etter[7].

In all N-acyl derivatives (NAC, NBZ, NPR), the side chain (N-acyloxyamide group) is linked to the phenolic oxygen atom by an intramolecular hydrogen bond. The packing of the molecules in the lattice is further strengthened by intermolecular hydrogen bonds. The hydrogen-bonding pattern of the secondary amides is discussed in the light of principles put forth by Etter[8] and also in terms of graph-set notations.

On the basis of the crystal structures of the reactants an attempt has been made to understand the mechanism of the reaction. The reaction is considered in terms of nucleophile–electrophile interaction[9]. Based on relevant parameters for such interaction, contact distance N(1) · · · C(8)(d) and the angles N(1) – C(8) – O(3) (α) and C(7) – N(1) – C(8) (α), an intramolecular mechanism was proposed. In addition, based on the unexceptionally short contact one of the amide hydrogens with the phenolic oxygen O(2) and the orientation of the amide group an intramolecular hydrogen abstraction process was suggested.

The reactant molecules were next analysed for thermal motion[10,11] using anisotropic thermal parameters (U_{ij}s). Rigid bond test[12] has been used to evaluate the accuracy of the U_{ij}s. Rigid molecule test[13] revealed that the molecules are not rigid. Between the reactive centres, *viz.*, C(8), and N(1), there is a significant internal motion as evidenced by large mean square displacement amplitude between the atoms. Non-rigid body analysis[14] indicated that the libration of acyloxy group about the C(2)-O(2) bond contributes significantly to the internal motion of the molecules. Interestingly, this libration, apparently plays an important role in bringing the acyl carbon C(8) towards the nucleophile, *viz.*, the amide nitrogen N(1), for the bond formation to occur. To sum up, both structural features and thermal motion analysis are in a position to throw light on the mechanism.

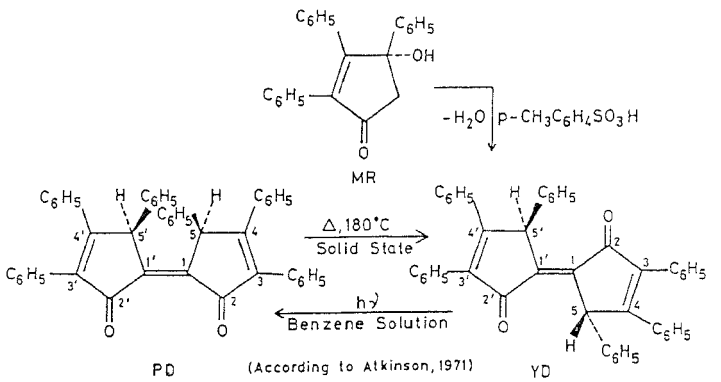

MR: 4-hydroxy-2, 3, 4-triphenyl cyclopent-2-en-1-one; PD: cis-2,2′-dioxo-3, 3′, 4, 4′, 5 α, 5′α-hexaphenyl 1, 1′-bi(cyclopentenylidene); YD: trans-2, 2′-dioxo-3, 3′, 4, 4′, 5α, 5′β-hexaphenyl 1, 1′-bi (cyclopentenylidene).

Scheme 2.

2.2. *cis-trans Isomerisation in substituted bi (cyclopentenilidene) derivatives*

The compounds MR, YD and PD were prepared and characterised spectroscopically. The crystal structure of MR and PD were determined and compared. However, the structure of YD could not be done as crystals of good quality could not be obtained. Surprisingly, the x-ray structure of PD is different from that assigned by Atkinson[4] based on spectral data. The spectral data was reinterpreted based on the observed crystal structure. The isomerisation reaction resembles the behaviour of indigo derivatives. There is a relative difficulty to isomerise in the present case unlike the facile conversion in indigoes. This observation could be explained on the basis of lack of conjugation through the central bond connecting the five-membered rings.

The above-mentioned studies reveal the importance of x-ray diffraction technique in understanding the mechanism of the solid-state reactions. It may also be added that the thermal motion analysis has been applied for the first time to a reaction involving a covalency change.

References

1. PAUL, I. C. AND CURTIN, D. Y. — *Acc Chem. Res.*, 1973, **6**, 217–225.
2. MANOHAR, H. — *J. Indian Inst. Sci.*, 1988, **68**, 277–294.
3. GORDON, A. J. — *Tetrahedron*, 1967, **23**, 863–870.
4. ATKINSON, R. S. — *J. Chem Soc. C*, 1971, 3524–3531.
5. MOHAN RAO. V. — *X-ray crystallographic and magnetic studies on dimeric copper (II) acetate adducts*, Ph.D. Thesis, Indian Institute of Science, Bangalore, 1980.
6. LEISEROWITZ, L. AND HAGLER, A. T. — *Proc. R. Soc. A.*, 1983, **388**, 133–175.
7. ETTER, M.C. — *Israel J. Chem* , 1985, **25**, 312–319.

8 ETTER, M. C , URBANCZYK-LIPKOWSKA, Z ,AMELI, T M. AND PANUNTO, T W	*J Cryst Spectrosc. Res* , 1988, **18**, 491–507
9. BURGI, H. B , DUNITZ, J D AND SHEFTER, E	*J. Am. Chem Soc.*, 1973, **95**, 5065–5067
10. CRUICKSHANK, D W J.	*Acta Cryst* , 1956, **9**, 754–756.
11. SCHOMAKER, V AND TRUEBLOOD, K N.	*Acta Cryst B*, 1968, **24**, 63–76
12 HIRSHFELD, F L.	*Acta Cryst A*, 1976, **32**, 239–244.
13. ROSENFIELD, R. E., TRUEBLOOD, K N AND DUNITZ, J D.	*Acta Cryst. A*, 1978, **34**, 828–829
14 DUNITZ, J. D AND WHITE, D N J.	*Acta Cryst. A*, 1973, **29**, 93–94.

Thesis Abstract (Ph.D.)

Synthetic spectroscopic and structural studies on transition metal complexes of diphosphazane ligands by M. S. Balakrishna.
Research supervisor: S. S. Krishnamurthy.
Department: Inorganic and Physical Chemistry.

1. Introduction

The main objective of this work is to synthesize new acyclic and cyclic diphosphazane ligands of the type $RN(PX_2)_2$ and $[RNP(X)]_2$ and to study their reactivity toward various transition metal organometallic derivatives. These diphosphazanes offer considerable scope as ligands since the substitutents on both nitrogen and phosphorus can be altered readily with attendant changes in the P–N–P bond angle and conformation around the phosphorus centres[1,2]. The reactions of the diphosphazanes with transition metal organometallic derivatives containing labile ligands yield several interesting complexes[3-5] which have been characterized by elemental analyses and ir and nmr (^1H, ^{13}C and ^{31}P) spectroscopic measurements. The structures of a few representative compounds have been confirmed by single crystal x-ray analysis.

2. Synthesis and structural studies

2.1. *Ligand synthesis*

The general method adopted for the synthesis of diphosphinoamines and cyclodiphosphazanes is as follows[6,7]:

The chlorine atoms in the $RN(PCl_2)_2$(I) and $[Bu^tNPCl]_2$ (III) can be easily replaced by alkoxide or aryloxide groups as shown in Scheme 1.

2.2. *Reactions of diphosphazanes (II) with Group 6 metal carbonyl derivatives*

Mononuclear Group 6 metal carbonyl derivatives of (II) of the general formula *cis*-$[M(CO)_4(PX_2)_2NR]$(V) have been prepared by the displacement of the coordinated olefin from the norbornadiene complexes, *cis*-$[M(CO)_4(C_7H_8)]$ (M = Cr, Mo) or piperidine from *cis*-$[M(CO)_4(pip)_2]$ (M = Mo, W) by the appropriate diphosphazane ligands following well-established procedures as shown in Scheme 2.

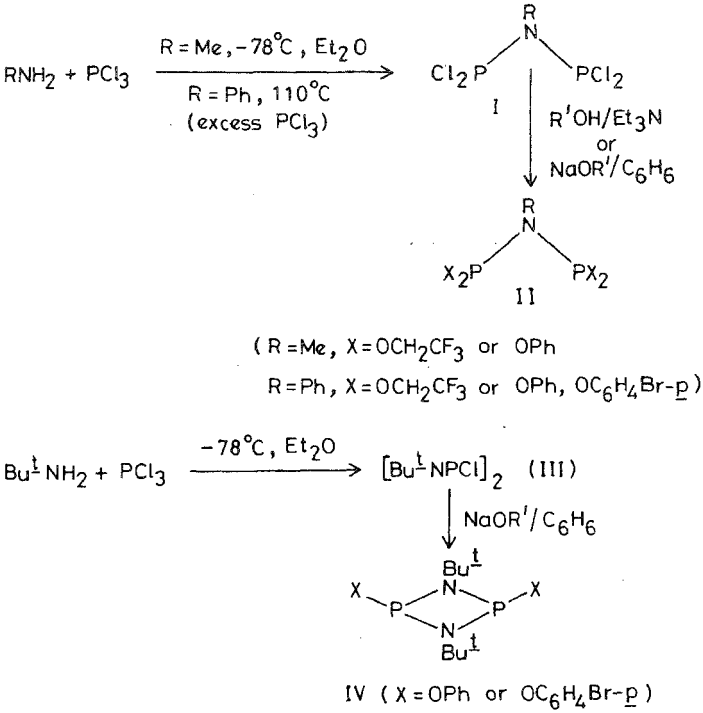

Scheme 1.

Even in the presence of an excess of the diphosphazane ligand only the *cis*-chelated complexes (V) could be isolated. The structure of one of these complexes, *cis*–[Mo $(CO)_4$(P $(OPh)_2)_2$NPh] has been confirmed by single-crystal x-ray analysis.

Seven coordinated complexes of diphosphazanes, RN $(PX_2)_2$ (R = Me, Ph) have been prepared by the following route:

$[MI_2(CO)_3(MeCN)_2] + RN(P(OPh)_2)_2 \longrightarrow [MI_2(CO)_3(P(OPh)_2)_2NR]$ VI [M = Mo, W; R = Me, OPh].

These complexes are the first examples of seven coordinated derivatives of diphosphazane ligands. The structure of one of these complexes, *viz.*, $[WI_2(CO)_3$ (P $(OPh)_2)_2$) NPh] has been confirmed by single-crystal x-ray analysis. The complex shows the less-common pentagonal bipyramidal geometry around the metal centre.

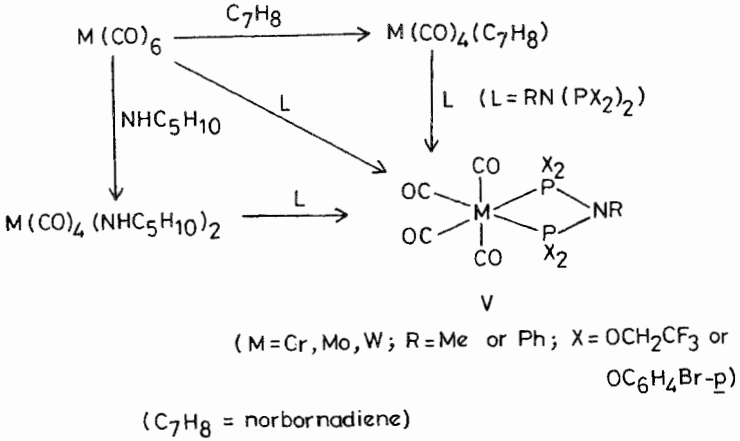

Scheme 2.

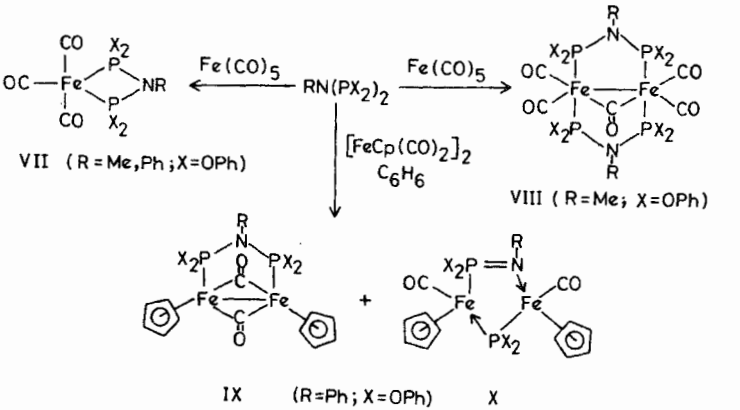

Scheme 3.

2.3. *Reaction of diphosphazanes (II) with iron pentacarbonyl and [FeCp $(CO)_2]_2$ (Cp = η^5–C_5H_5)*

Reactions of $Fe(CO)_5$ with diphosphazanes, $RN(P(OPh)_2)_2$ (R = Me, Ph) under ultraviolet irradiation (using a medium-pressure 450-W mercury ultraviolet lamp with a water-cooled pyrex jacket) afford both mononuclear (VII) and binuclear (VIII) complexes as shown in Scheme 3.

The thermal reaction of $PhN(P(OPh)_2)_2$ with [FeCp $(CO)_2]_2$ yields a mixture of IX and X which are separated by fractional crystallization. The formation of complex X is interesting in that one of the P–N bonds of the ligand cleaves to give the fragments $P(OPh)_2$ = NPh and $P(OPh)_2$ which act as bridging ligands between the two metal centres.

2.4. *Reactions of diphosphazanes (II) with rhodium derivatives*

Reactions of diphosphazanes, $RN(PX_2)_2$ with rhodium derivatives such as [RhCl] (COD)]$_2$ and [RhCl $(CO)_2]_2$ lead to the isolation of dinuclear complexes as shown in Scheme 4.

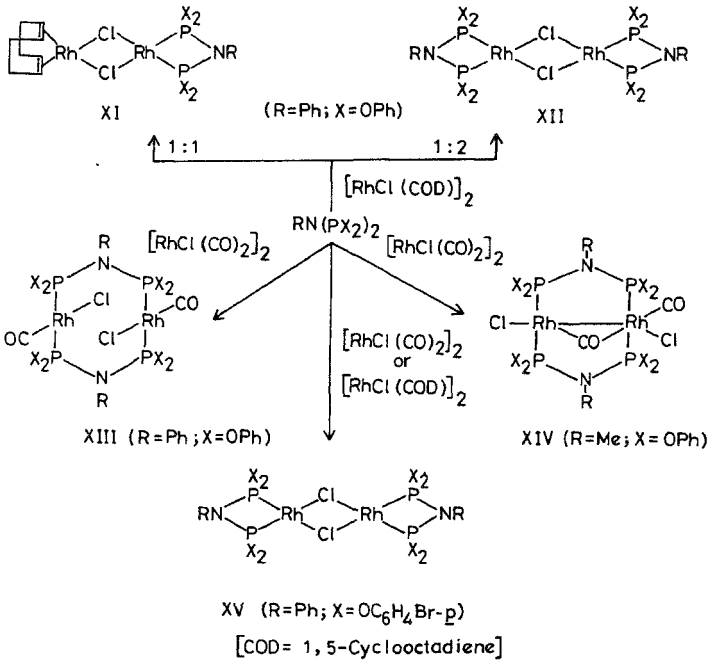

Scheme 4.

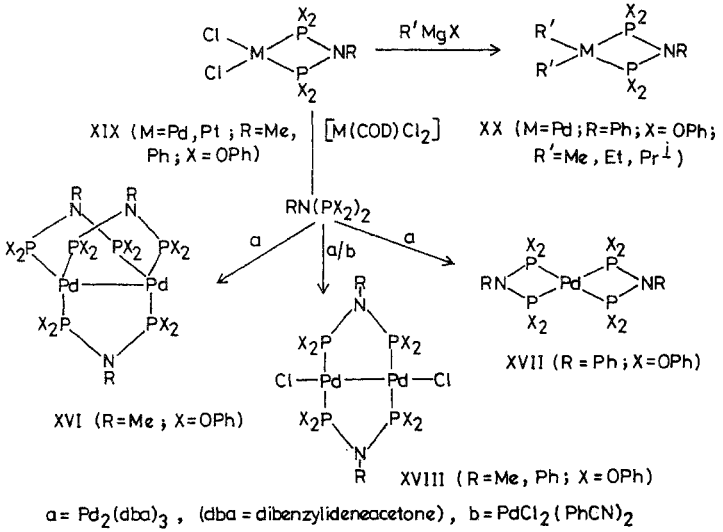

Scheme 5.

The ^{31}P nmr spectra of these complexes clearly display $^{103}Rh-^{31}P$ coupling. The $^{1}J(RhP)$ value varies from 187 to 285 Hz.

2.5. Reactions of diphosphazanes(II) with palladium and platinum derivatives

Reactions of diphosphazanes with suitable palladium precursors lead to the isolation of both mononuclear and dinuclear complexes. Reactions with platinum derivatives have been explored to a limited extent and only complexes of the type *cis*-$[PtCl_2\text{-}(P(OPh)_2)_2NR]$ have been isolated. The complexes isolated are shown in Scheme 5.

A novel dinuclear palladium (O) complex, $[Pd_2\{(P(OPh)_2)_2NR\}_3]$ (XVI), containing three bridging bidentate N-methyl diphosphazane ligands has been isolated and this represents the first example of a palladium (O) complex with acyclic diphosphazane ligands. An analogous reaction with the N-phenyl diphosphazane, $PhN(P(OPh)_2)_2$ does not give a dinuclear complex; only a *bis*-chelated complex (XVII) could be isolated. The structure of XVI has been determined by single-crystal x-ray analysis which reveals an unusually short metal–metal distance of 2·856 Å.

The chelate complex, $[PdCl_2(P(OPh)_2)_2NPh]$, reacts with Grignard reagents, R'MgX (R = Me,Et,Pr^i) to give the organopalladium derivatives, $[PdR'_2(P(OPh)_2)_2NPh]$(XX).

2.6. Coordination chemistry of cyclodiphosphazane, [Bu^{t}NP (OPh)]$_2$

Reactions of cyclodiphosphazane, [Bu^{t}NP (OPh)]$_2$ have been carried out with Group 6 metal carbonyl,

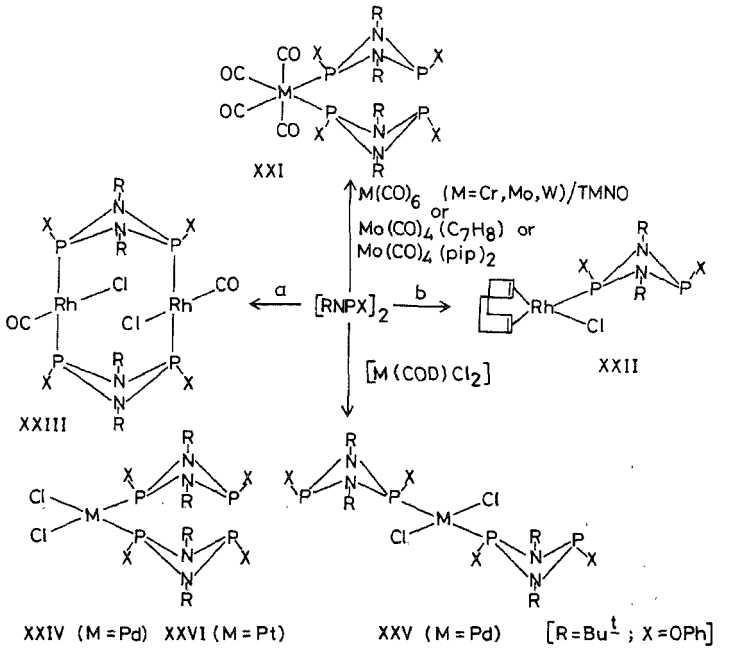

Scheme 6.

rhodium, palladium and platinum derivatives and several new complexes have been isolated and characterized (*see* Scheme 6). In these complexes, monodentate as well as bridged bidentate modes of coordination of cyclodiphosphazane ligands have been observed.

3. Conclusions

The results obtained demonstrate the versatility of diphosphazane ligands. Fairly small differences in the diphosphazane ligands can cause significant changes in their coordination behaviour[8–10]. Some of the complexes isolated (XVIII, XXI–XXVI) can serve as valuable synthons for preparing a variety of homo- and heterobinuclear complexes and high-nuclearity clusters.

References

1. Keat, R., Muir, K. W., Muir, L. M. and Rycroft, D. S. *J. Chem. Soc., Dalton Trans.*, 1981, 2192–2198.

2.	CHEN, H -J , BARENDT, J F., HALTIWANGER, R C., HILL, T. G AND NORMAN, A D	*Phosphorus Sulfur*, 1985, **26**, 155–158
3.	BALAKRISHNA, M S., PRAKASHA, T. K. AND KRISHNAMURTHY, S. S.	*Proc Indian Natn Sci Acad* , A, 1989, **55**, 335–341.
4	BALAKRISHNA, M. S , PRAKASHA, T. K AND KRISHNAMURTHY, S. S.	*Phosphorus, Sulfur and Silicon*, 1990/91, **49/50**, 409–412
5	BALAKRISHNA, M S , PRAKASHA, T K., KRISHNAMURTHY, S S , SIRIWARDANE, U , AND HOSMANE, S N.	*J Organomet. Chem* , 1990, **390**, 203–216.
6	DAVIES, A R , DRONSFIELD, A T HASZELDINE, R N. AND TAYLOR, D. R.	*J. Chem. Soc , Perkin Trans* , 1973, 379–385.
7.	JEFFERSON, R , NIXON, J F., PAINTER, T M , KEAT, R. AND STOBBS, L.	*J Chem Soc., Dalton Trans.*, 1973, 1414–1419
8.	KING, R. B.	*Acc Chem. Res* , 1980, **13**, 243–248.
9.	HAINES, R. J., LAING, M , MEINTJIES, E AND SOMMERVILLE, P	*J Organomet Chem.*, 1981, **215**, C17–C19.
10	MAGUE, J. T. AND LLOYD, C. L	*Organometallics*, 1988, 7, 983–993.

Thesis Abstract (Ph.D.)

Novel reactions of copper(I) phenoxide with heteroallenes: A synthetic and structural study by N. Narasimhamurthy.
Research supervisors: A. G. Samuleson and H. Manohar.
Department: Inorganic and Physical Chemistry.

1. Introduction

Reactivity of copper(I) phenoxide and its complexes with O_2 has been the subject of several recent investigations[1,2]. These studies have indicated that copper(I) phenoxide with appropriate coordination geometry and electronic environment provides a suitable site for the activation of O_2 However, these studies have been concentrated primarily on the activation of O_2 and little attention has been focussed on other small molecules like heteroallenes. Although activation of CO_2 by copper(I) phenoxide has been studied[3], surprisingly, its analogs like CS_2 and related heteroallenes have remained uninvestigated. In the present study, novel reactions of copper(I) phenoxide with heteroallenes have been identified Synthetic ramifications of these reactions and structural characterisation of the products by spectroscopic techniques and single-crystal x-ray study are discussed.

2. Results and conclusions

The synthetic and mechanistic aspects of the reactions of copper(I) phenoxides with heteroallenes and related molecules, studied, are depicted in Fig. 1. A novel reactivity of copper(I) phenoxides and alkoxides (**1**) with CS_2 is exploited to prepare a variety of aryl and alkyl orthocarbonates (**2**). This is the first example of such a reactivity observed with copper(I) phenoxides and alkoxides[4]. Several orthocarbonates hitherto unknown and difficult to prepare are synthesised using this procedure. It has been shown that the reactivity and ease of formation of these products depends on the steric, electronic and coordination effects of the substituents at the phenoxide. Several control experiments carried out to understand the reaction pathways are depicted in Fig. 1. It has been shown that the reaction proceeds through a tetrameric

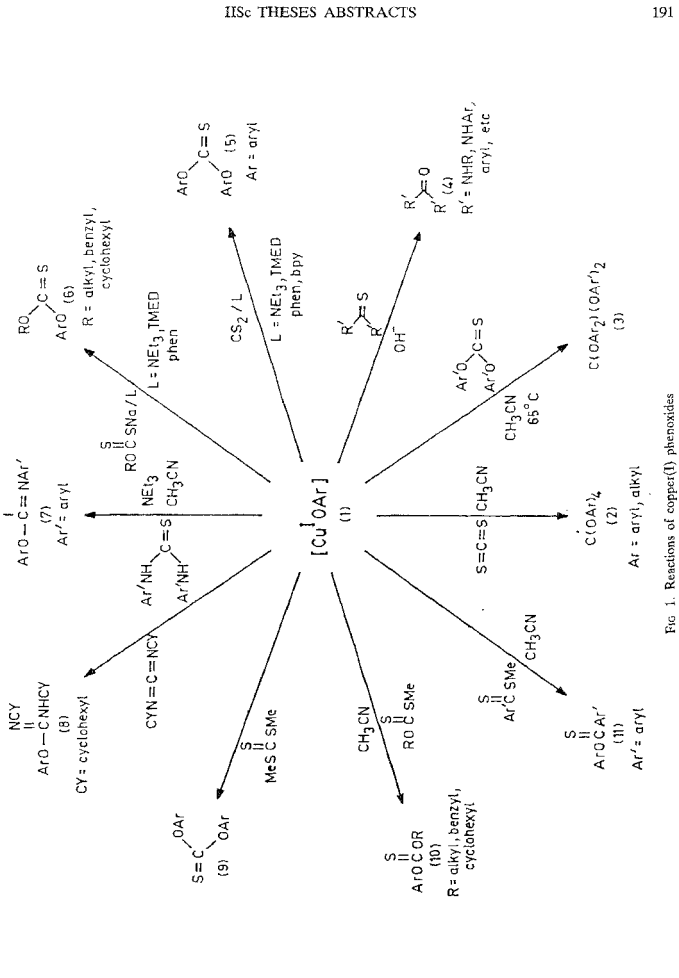

FIG 1. Reactions of copper(I) phenoxides

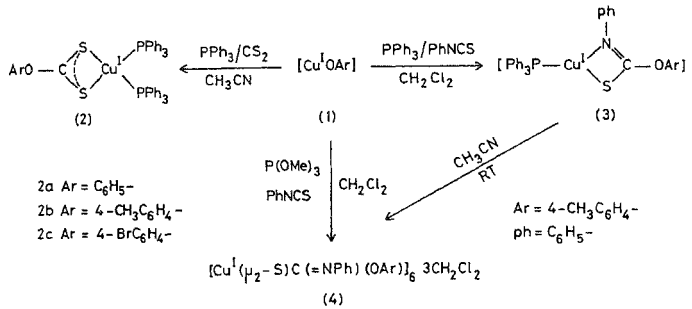

FIG 2 Copper(I) complexes isolated from the reaction of $[Cu^{I}OArLn]$ with CS_2 and PhNCS. (L = Phosphorus donor).

copper(I) phenoxide intermediate rather than by a simple stepwise nucleophilic substitution of phenoxide ion at CS_2.

In the presence of tertiary nitrogen and phosphorus donor ligands a modified reactivity of copper(I) phenoxide with CS_2 and related xanthates has been observed[4]. These modifications lead to a facile method for the preparation of thioncarbonates(5) and mixed thioncarbonates (6). Differences in reactivity with respect to the nature of the ligand are observed. The use of pure σ-donor ligands like triethylamine and tetramethylethelenediamine show increased reactivity and give good yields of thioncarbonates. In the case of moderate π-acceptor ligands like 1,10-phenanthroline or 2,2'-bipyridyl, the course of the reaction could be monitored spectrophotometrically and is shown to follow a pseudo-first-order kinetics. Strong π-acceptor ligands like PPh_3 and $C_6H_{11}NC$ show reduced reactivity and do not promote the formation of thioncarbonates (5). These results are rationalised on the basis of the formation of a binuclear copper(I) phenoxide complex. A further understanding of these reactions needs the synthesis and isolation of binuclear copper(I) complexes with σ-donor nitrogen ligands, the structural and physicochemical studies of these complexes and the effect of structure and environment on the affinity of CS_2. These aspects should be able to bring out features which will throw some light on the mechanistic understanding of the reaction.

Unlike CS_2, the reactivity of copper(I) phenoxides with other heteroallenes like PhNCO, PhNCS and dicyclohexylcarbodiimide has been shown to be dependent on the nature of the ancillary ligands, order of addition of the reagents and the nature of the solvents used. The reaction of copper(I) phenoxide with PhNCS in the presence of PPh_3 or $P(OMe)_3$ as an ancillary ligand lead to different products. The synthetic and structural characterisation of the products obtained with PhNCS and its analogous CS_2 are described in Fig. 2. The reaction of PhNCS in the presence of $P(OMe)_3$ leads to a compound without the ancillary ligand. This compound represents the first structurally characterised hexameric copper(I) complex $[(4\text{-}MeCh_3C_6H_4O\text{-})C(=NC_6H_5)\ (\mu_2\text{-}S)Cu]_6$,[7] formed by the insertion of PhNCS across Cu(I)–O. The ligand $(4\text{-}MeCh_3C_6H_4O\text{-})C(=NC_6H_5)S^{-}$ displays a novel type of tridentate coordination through bridging S and N atoms. The six cuprous ions together with coordinating atoms assume a 'paddle-wheel' geometry. The hexamer shows two different types of Cu-Cu distances. In contrast, the reaction of PhNCS in the presence of PPh_3 as a ligand provides a copper(I) complex $[(4\text{-}MeCH_3C_6H_4O)C(=NC_6H_5)SCu(PPh_3)]$ possibly monomeric in nature with one coordinating PPh_3 ligand. Interestingly, the latter compound in the presence of coordinating solvents like CH_3CN loses PPh_3 readily and converts to hexameric complex. The analogous CS_2 reaction in the presence of PPh_3 leads to a monomeric tetrahedral copper(I) complex, $[(PPh_3)_2Cu(n^{-}\text{-}S_2)COC_6H_4CH_3\text{-}4)]$ coordinated by two PPh_3 ligands and two sulphur atoms from the dithiocarbonato moiety. These two reactions have simplified the mechanistic understanding of the formation of hexameric complex. A mechanism is proposed, involving an intermediate monomeric copper(I) complex coordinated by a phosphorus donor ligand, for the formation of these compounds.

These findings suggest that the nucleophilic activation of heteroallenes by copper(I) phenoxide may require a fine tuning of coordination geometry and electronic environments. Such ligand modification to alter the properties of the copper(I) phenoxide is expected to open up new areas of interesting chemsitry. As these studies progress, a better understanding of the factors which affect the reactivity should be gained and rational design of specific catalysts might become a reality.

Carbon compounds containing more than two hetero atoms on the same carbon atom are known to exhibit changes in conformation and structural parameters. The results of the investigations of such (anomeric) interactions in orthocarbonates, $C(OR)_4$, by MM2 calculations and x-ray diffraction methods are also reported[8]. MM2 calculations on $C(OR)_4$, R = H (**1**), Me (**2**), Ph (**3**) indicate two closely spaced minima D_{2d} and S_4 symmetry. Single-crystal x-ray structures for three derivatives of orthocarbonates $C(OAr)_4$, Ar=$-C_6H_5$ (**4**), $-C_6H_3Me_2-3,5$ (**5**), C_6H_4Br-4 (**6**) are solved The two crystallographic nonequivalent molecules in the unit cell of (**4**), as well as (**5**), adopt conformations in which the central $C(OC)_4$ units have a near D_{2d} symmetry, while the corresponding fragment in (**6**) has a distorted S_4 symmetry. These findings suggest that the energy between the two conformers D_{2d} and S_4 is very small as also indicated by MM2 results. The consequences of this effect on conformation and structural parameters of these compounds are discussed in detail.

References

1. KARLIN, K D. AND ZUBIETA, J — *Copper coordination chemsitry. biochemical and inorganic perspectives*, 1982, Adenine Press.
2. KARLIN, K. D AND ZUBIETA, J — *Biological and inorganic copper chemistry*, Vols 1 & 2, 1984, Adenine Press
3. YAMAMOTO, T , KUBOTA, M. AND YAMAMOTO, A — *Bull Chem. Soc Jap* , 1980, **53**, 680–683
4. NARASIMHAMURTHY, N. AND SAMUELSON, A G — *Tetrahedron Lett.*, 1986, **27**, 991–992.
5. NARASIMHAMURTHY, N. AND SAMUELSON, A G. — *Tetrahedron Lett* , 1988, **29**, 827–830.
6. NARASIMHAMURTHY, N. AND SAMUELSON, A G — *Proc Indian Acad Sci. A*, 1989, **55**, 383–391.
7. NARASIMHAMURTHY, N., SAMUELSON, A. G AND MANOHAR, H. — *J. Chem Soc. Chem. Commun.*, 1989, 1803–1804.
8. NARASIMHAMURTHY, N , MANOHAR, H. SAMUELSON, A G. AND CHANDRASEKAR, J. — *J. Am Chem. Soc* , 1990, **112**, 2937–2941

Thesis Abstract (Ph.D.)

Synthetic studies in terpenoids by S. Janaki.
Research supervisor: G. S. R. Subba Rao.
Department: Organic Chemistry.

1. Introduction

The Diels-Alder reaction involving a cyclohexa-1, 3-diene and a variety of dienophiles is one of the most common and elegant methods for the construction of a bicyclo [2·2·2] skeleton[1]. The greater comprehension of the steric and electronic effects governing Diels–Alder reaction[2] has led to the utilisation of specifically functionalised dienes and dienophiles to produce adducts which are otherwise difficult to obtain with a degree of regio- and stereospecificity

Our continuing interest in the synthesis of spirosystems[3] prompted us to carry out the synthesis of spiro

compounds of β-vetivone family. The spiro centre can be produced by the specific bond cleavage of the bicyclo[3.2.1] system. One of the attractive ways of making a bicyclo[3.2.1.]system is by the skeletal rearrangement of a bicyclo[2.2.2] system.

2. Experimental and discussion

Regiospecific addition of α-chloroacrylonitrile to the diene (**5**), obtained by metal ammonia reduction of 6-methoxy-1-methyltetralin (**3**), followed by conjugation, furnished the adduct (**6**) as a mixture of *endo*- and *exo*- isomers (5:2). Hydrolysis of the mixture with aq.KOH in DMSO afforded the ketone (**7**) Reduction of the ketone (**7**) with sodium borohydride gave a mixture (3:1) of *endo*- and *exo*- alcohols (**8** and **9**). Rearrangement of the *endo*- alcohol (**8**) with BF_3-Et_2O gave a 3:2 mixture of the enone (**10**) and the ketone (**11**). Oxidation of the ketone (**10**) with $RuCl_3$. $3H_2O$–$NaIO_4$ furnished the keto acid (**12**). Addition of methylmagnesium iodide to the keto acid (**12**), followed by esterification afforded the hydroxy ester (**13**). Dehydration of the ester (**13**) gave a mixture of olefins (**14** and **15**) which was separated by chromatography over silica gel impregnated with 15% silver nitrate. The *exo*-olefin (**15**) was readily isomerised to the *endo*-olefin (**14**) with PTS. Grignard reaction of the ester (**14**) with methyl magnesium iodide afforded a mixture of (±)–hinesol (1) and 10-epi (±)–hinesol (**2**)[4]. The structure of the ketone (**11**) was deduced from spectral data and confirmed by chemical degradation experiments. The ketone (**11**) was deoxygenated *via* thio acetalization followed by desulfurization with Raney–Ni to furnish the compound (**16**). The compound (**16**) was oxidised with $RuCl_3$–$3H_2O$–$NaIO_4$ to the dione (**17**). Aldol condensation of the dione (**17**) gave the unsaturated ketone (**18**), thus establishing the position of the double bond in the ketone (**11**).

The synthesis of structurally interesting tricyclic bridged sesquiterpenes, isolated from *E.georgei* Diels, has been attempted using the above strategy.

Diels-Alder reaction of the diene (**24**), readily accessible from the corresponding aromatic precursor (**22**) by metal–ammonia reduction and isomerisation, with α-chloroacrylonitrile gave the adduct (**25**). Hydrolysis of the adduct (**25**) furnished the tricyclic ketone (**26**). Grignard reaction of the ketone (**26**) with methyl magnesium iodide afforded the alcohol (**27**) (*exo*- and *endo*- mixture) which underwent a stereospecific Wagner-Meerwein rearrangement on refluxing with BF_3-Et_2O in benzene to yield exclusively the enone (**30**). The enone (**30**) was transformed to the sesquiterpenes (**19**) and (**20**). On the other hand, reduction of the ketone (**26**) with sodium borohydride furnished the isomeric mixture of alcohols (**28**) and (**29**) (1:3 ratio). The *endo*-alcohol (**29**) underwent a smooth acid-catalysed rearrangement to the enone (**31**). The enone (**31**) was further elaborated to the natural product (**21**).

Calyone (**32**), calyenone (**33**) and precalyone (**34**), isolated from the aqueous ethanolic extract of *Roylea calycina* (Roxb.) Briq., showed significant anticancer activity against P-388 lymphocytic leukaemia in mice[5]. Precalyone is readily converted to cayone by mild acidic reagents like silica gel and amberlite IR-120 (H^+ form). Calyone undergoes dehydration to give calyenone. In view of these interconversions, the synthesis of calyenone will prove the structure of other two molecules and hence the total synthesis of calyene was attempted.

An attempted synthesis of **36**, a key intermediate in the synthesis of calyenone, was accomplished starting from the ketone (**37**). Thus, Woodward alkylation of the ketone (**37**) with potassium-t-butoxide and methyl iodide gave the ketone (**38**). Reduction of ketone (**38**) with sodium borohydride, followed by acetylation of the resulting alcohol (**39**) gave the acetate (**40**). Allylic oxidation of the acetate (**40**) furnished the enone (**41**). Metal–ammonia reduction of the double bond in the enone (**41**) gave the alcohol (**42a**) with A/B *trans* ring junction. The acetate (**42b**), obtained by the acetylation of the alcohol (**42a**), was carbomethoxylated to the ester (**43**). Introduction of **8(9)** double bond in (**43**) with phenylselenenyl chloride furnished the enone (**44**). The ketal ester (**45**) was reduced with LAH and the residue obtained after removal of the solvent was found to be a mixture of components, none of which analysed for the required product.

Recently, Errington *et al*[6] isolated the methyl ester of 7-oxo-11-nordrim-8-en-12-oic acid (**44**) as the major component from the terpene fraction of the culture fluid of *Lepista glaucocana* (Bres.) Singer and deduced its structure from analytical and spectral data. Since the intermediate (**38**) is readily available

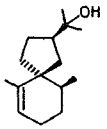

1

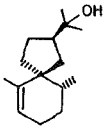

2

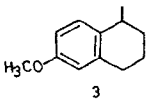

3

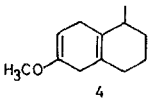

4

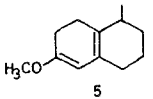

5

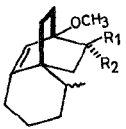

6 R_1, R_2 = Cl, CN
7 R_1, R_2 = O
8 R_1 = H; R_2 = OH
9 R_1 = OH; R_2 = H

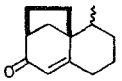

10

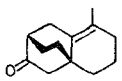

11

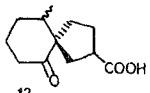

12

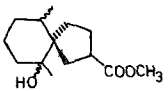

13

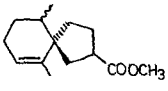

14

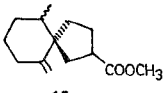

15

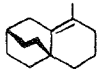

16

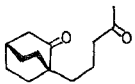

17

18

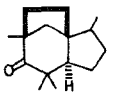

19

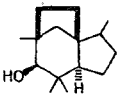

20

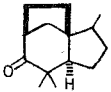

21

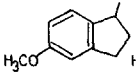

22

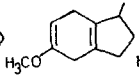

23

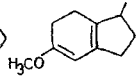

24

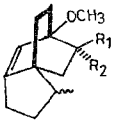

25 R_1, R_2 = Cl, CN
26 R_1, R_2 = O
27 R_1, R_2 = CH_3, OH
28 R_1 = OH; R_2 = H
29 R_1 = H; R_2 = OH

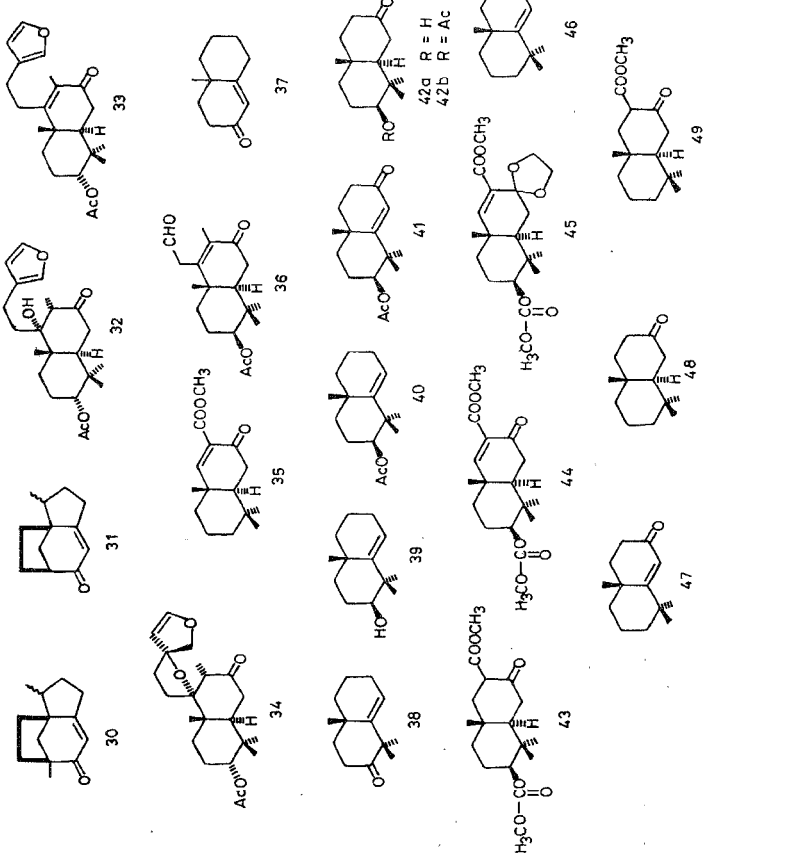
30
31
32
33
34
35
36
37
38
39
40
41
42a R = H
42b R = Ac
43
44
45
46
47
48
49

from the previous experiments, its conversion to the metabolite (**44**) has been successfully carried out to confirm the proposed structure. Thus, reduction of the ketone (**38**) under Huang-Minlon conditions yielded the compound (**46**). Allylic oxidation of the compound (**46**), followed by metal–ammonia reduction of the enone (**47**), gave the saturated ketone (**48**) with A / B *trans* ring junction. Reaction of **48** with dimethyl carbonate in the presence of sodium hydride afforded the β-ketoester (**49**) which was subsequently converted to the natural product[7] having the **8(9)** double bond through the sequence of reactions involving the elimination of phenylselenenyloxide.

References

1. PETRZILKA, M AND GRAYSON, J. I. — *Synthesis*, 1981, 765–786.
2. WOODWARD, R B AND HOFFMAN, R. — *The conservation of orbital symmetry*, 1970, Verlag Chemie, Weinheim
3. PRAMOD, K. AND SUBBA RAO, G. S. R. — *Ind. J. Chem. B*, 1986, **25**, 783–784.
4. SUBBA RAO, G. S. R., AND JANAKI, S. — *Tetrahedron Lett.*, 1988, **29**, 3105–3108
5. OM PRAKASH, BHAKUNI, D S., KAPIL, R. S., SUBBA RAO, G. S R. AND RAVINDRANATH, B. — *J. Chem. Soc., Perkin Trans. I*, 1979, 1305–1308.
6. ERRINGTON, S. G., FARRELL, I W , HALSALL, T. G., HEARN, M. T. W. JONES, E. R. H. AND THALLER, V. — *J. Chem Res (S)*, 1987, 47.
7. JANAKI, S. AND SUBBA RAO, G. S R. — *Ind. J. Chem. B*, 1988, **27**, 505–507.

Thesis Abstract (Ph.D.)

Investigations of the interaction of molecules with clean and modified transition metal surfaces by techniques of electron spectroscopy by K. Prabhakaran.

Research supervisor: C. N. R. Rao.
Department: Solid State and Structural Chemistry Unit.

1. Introduction

In the last two decades, electron spectroscopic techniques such as ultraviolet and x-ray photoelectron spectroscopies (UPS and XPS), high-resolution electron energy-loss spectroscopy (HREELS) and Auger electron spectroscopy (AES) as well as low-energy electron diffraction (LEED) have emerged as the most powerful means to investigate the electron states of solid surfaces and adsorbed molecules[1-3]. This has become possible because of high surface sensitivity of these techniques and potentiality to carry out studies in ultra high vacuum on well-defined systems like single crystal surfaces. A major theme in this work is addressed to understand the nature of interaction of a variety of molecules with the surfaces of metals, modified metals, alloys and metallic glasses and to characterise the intermediate surface species formed during their chemical transformations. One of the important problems discussed is related to the characterisation of molecular oxygen adsorbed on single crystal as well as polycrystalline metal surfaces. Attempts have been made to understand the nature of oxygen in the superconducting oxide $YBa_2Cu_3O_{6.9}$.

2. Experimental

Electron spectroscopic measurements were carried out in VG ESCA 3 MARK II and VG ESCALAB spectrometers. Hell radiation (hv = 40·8eV) was used for the UPS studies and AIK α (1486·6eV) or MgK α (1253·6eV) x-radiation for the XPS studies. In electron energy-loss spectroscopy (EELS), one measures the loss in energy of the incident electrons during an inelastic scattering process on interaction with matter. If a primary beam of energy in the range 2·5–6eV is used information on the excitation of the vibrational dipoles of adsorbed molecules is obtained.

In AES, x-radiation or an electron beam is used as the source. This initiates ionization of a core electron and the vacancy created in the core level is filled by a nonradiative electron jump from a higher energy level with the simultaneous ejection of an Auger electron from one of the energetically accessible levels.

In LEED, electrons of well-defined energy and direction of propagation diffract crystal surfaces. The electrons are scattered mainly by the individual atom cores of the surface and produce wave interferences that depend strongly on the relative atomic positions of the surface under examination.

3. Results and conclusions

In recent years, there have been several reports in literature on the presence of chemisorbed molecular oxygen species on various metal surfaces. A critical overview of the present understanding of the nature of molecular oxygen adsorbed on metal surfaces as derived from UPS, XPS and HREELS investigations has been presented. It seems clear that at low temperatures, molecularly adsorbed oxygen exists in a peroxo form (O_2^{2-}) with filled π_g antibonding orbital. However, on surfaces such as of Ag, the possibilty of the presence of a superoxo type of molecular oxygen (O_2^{1-}) with more than half-filled π_g antibonding level cannot be ruled out.

Adsorption of molecular oxygen on Cu(110), polycrystalline Cu and polycrystalline Ag was carried out at low temperatures. In all these systems we have observed the presence of a peroxo type of molecular oxygen which dissociates in the temperature range 150–230K. This species is characterised by a ν(O–O) of 600-800 cm^{-1} and an O(1s) binding energy of 531·5–533 eV. The adsorbed molecular oxygen gives rise to a three-peak UP spectrum due to π_g, π_u and σ_g levels. At higher temperatures, molecular oxygen dissociates to atomic oxygens which forms an ordered layer on the Cu(110) surface, exhibiting a (2×1)-O LEED pattern. Adsorption of oxygen on this surface at low temperatures (~ 80K) results in the formation of (1×1) LEED pattern. On a polycrystalline Ag surface at low temperatures, besides a peroxo species, we see evidence for a superoxo type of molecular oxygen characterised by ν(O–O) band around 1300cm^{-1} in HREELS. This species disappears when the surface is warmed to 200K, whereas the peroxo species is stable up to 230K. Polycrystalline Cu surface has been modified by presorption of electronegative atoms such as Cl to enhance the stability of the chemisorbed molecular oxygen. The co-adsorbed chlorine depletes the metal electron density available for transfer to the antibonding orbital of O_2 which makes the dissociation sluggish.

An attempt has been made to understand the nature of oxygen in superconducting $YBa_2Cu_3O_{6.9}$ (T_c~90K) in the normal and the superconducting states. The study reveals the existence of a peroxo type of oxygen species (O_2^{2-}) characterised by an O(1s) binding energy of 532·6eV in addition to the O^{2-} species with an O(1s) binding energy of 528·5eV. The concentration of the peroxo type of species increases significantly when the sample is in the superconducting state. By measuring the intensity of the inelastically scattered electrons, using an electron energy-loss spectrometer we are able to monitor the surface conductivity changes of the sample as a function of temperature.

We have carried out electron energy-loss spectroscopic studies of surface hydroxylation on a Cu(110) surface covered by atomic oxygen, by interaction with proton donor molecules such as water, methanol, formic acid, ammonia, dimethyl amine; H_2S and HCl. The characteristic δ(OH) and ν(O–H) bands of surface hydroxyl group are observed around 1100 and 3600cm^{-1}, respectively. We have investigated the interaction of organic molecules such as formaldehyde, acetaldehyde, paraldehyde, acetone, acetic acid, ethanol and diethyl ether with clean and oxygen-covered Cu(110) surfaces. It is shown that on a clean Cu(110) surface these molecules adsorb molecularly at low temperatures and transform to various surface species on warming. Interesting chemical reactions take place when these molecules are adsorbed on an oxygen-covered surface. We have also attempted to understand the nature of interaction of carbonyl compounds with a Cu(110) surface modified by depositing aluminium atoms.

In another experiment, we studied the interaction of carbon monoxide (CO) with the surfaces of glassy and partially crystalline alloys containing elements such as Ni, B, Si, Fe, Mo, Cu and Pd. The prominent mode of interaction of CO with the surfaces of glassy alloys is found to be dissociative. CO dissociation on a glassy $Cu_{50}Zr_{50}$ surface forms graphitic and carbidic carbon species.

Oxygen-, nitrogen- and carbon-containing molecules, namely, oxygen, water, methanol, carbon monoxide, nitrogen, ammonia and amines adsorbed on metal surfaces have been characterised by employing Auger electron spectroscopy. Analysis of Auger spectra shows that these Auger transitions rise from the molecular orbitals of the adsorbed species and are distinctly different from the transitions arising from the atomic species.

References

1. CARLSON, T A — *Photoelectron and Auger spectroscopy*, 1975, Plenum

2. BRIGGS, M P. AND SEAH, D — *Practical surface analysis*, 1983, Wiley.

3 JOYNER, R W. AND ROBERTS, M. W. — *Surface and defect properties of solids*, Specialist Periodic Report, 1976, Chemical Society, London

Thesis Abstract (Ph.D.)

High-temperature superconductivity in thallium cuprates and related systems by A. K. Ganguli.
Research supervisor: C. N. R. Rao.
Department: Solid State and Structural Chemistry Unit.

1. Introduction

Synthesis and characterization of novel oxide materials have been a major area of research for solid-state chemists. Discovery of high-temperature superconductivity in oxide materials[1] has further brought forward the importance of sustained efforts for the synthesis of novel materials with probable higher superconducting transition temperatures which will be of tremendous importance to various frontier technological applications.

2. Experimental and discussion

Synthesis, characterization and properties of the following families of layered superconducting Tl cuprates have been investigated: (1) $Tl_2Ca_{n-1}Ba_2Cu_nO_{2n+4}$, (2) $TlCa_{n-1}Ba_2Cu_nO_{2n+3}$, (3) $TlCa_{1-x}Y_x{-}Ba_2Cu_2O_{7+\delta}$, (4) $Tl_{1-x}Pb_xCaSr_2Cu_2O_{7+\delta}$, (5) $TlCa_{1-x}\ Ln_xSr_2\ Cu_2O_{7+\delta}$, and (6) $TlSr_{2-x}\ La_xCuO_{5+\delta}$. Besides x-ray diffraction, electrical and magnetic measurements, a variety of other techniques such as high-resolution electron microscopy, neutron diffraction, x-ray photoemission, x-ray absorption, non-resonant microwave absorption, thermoelectric power and Raman spectroscopy have been employed to investigate these superconducting cuprates[2,3]. After developing a method for the synthesis of the thallium cuprates, the n=2 and 3 members of the $Tl_2Ca_{n-1}Ba_2Cu_nO_{2n+4}$ family were the first to be characterized in some detail. Intergrowth structures in this family of cuprates were also identified. $TlCaBa_2Cu_2O_{7+\delta}$, the n = 2 member of the 1122 type belonging to the $TlCa_{n-1}Ba_2Cu_nO_{2n+3}$ series, containing only one Tl–O layer was then synthesized and characterized for the first time[4] ($T_c \sim 90$K). Partial substitution of Ca by Y in this 1122 cuprate was found to decrease the T_c. Although members of the Tl–Ca–Sr–Cu–O system cannot be prepared, partial substitution of Tl by Pb enables us[5] to prepare 1122 cuprates of the type $Tl_{1-x}Pb_xCaSr_2Cu_2O_{7+\delta}$; the x=0·5 member shows a T_c of 90K. A neutron-diffraction study of this oxide has also been carried out. A new series of superconducting cuprates of the formula $TlCa_{0.5}Ln_{0.5}Sr_2Cu_2O_{7+\delta}$ (T_c, 60–90K) (Ln= rare earth) has been identified[6]. $TlCa_{1-x}Yb_xSr_2Cu_2O_{7+\delta}$ ($0{\cdot}25 \leq x \leq 1{\cdot}0$) is a fascinating system where the nature of charge carriers seems to change from electron-like to hole-like as a function of composition. The first member of a new $TlSr_{n+1-x}Ln_xCu_nO_{2n+3}$ (Ln=La) series of superconducting cuprates possessing the 1021-type structure has been synthesized[7]. The n=1 (1021) members show T_cs around 40K, with electrons or holes as the majority charge carriers depending on x.

Members of the $PrBa_2Cu_3O_{7-\delta}$ system possessing the orthorhombic structure over a wide range of oxygen stoichiometry ($\delta = -0{\cdot}5$ to $+0{\cdot}5$) have been prepared and characterized[8]. Similar compositions with a

tetragonal structure have also been prepared. None of the oxides is superconducting, independent of the structure or stoichiometry. Praseodymium seems to be present to a small extent in the 4+ state in oxygen-excess (negative) samples. Orthorhombic $PrBa_2Cu_3O_{7-\delta}$ samples show that the presence of twins has no relation to superconductivity. A neutron-diffraction study of a near-stoichiometric sample has shown a disordered orthorhombic structure with 72% occupancy of the 01 (chain) sites and with no interchange between Pr and Ba sites.

Oxides of the type $La_{2-x}M_xBO_{4+\delta}$ (M=Na, Sr or Ba; B=Ni or Pd) have been synthesized and their electrical, magnetic and other properties have been investigated. Nickelates of the type $La_{2-x}Ni_xO_{4+\delta}(0{\cdot}0 \leq x \leq 0{\cdot}2)$ show onset of diamagnetism around 20K. No anomalies are observed in the resistivity, magneto-resistance and thermopower of these nickelates[9]. Palladates of the type $La_{2-x}M_xPdO_{4+\delta}$ have been synthesized for the first time. These crystallize in a tetragonal structure, $a \simeq 4{\cdot}12$A, $c \simeq 6{\cdot}90$ A. All the palladates show high resistivity and nearly temperature-independent magnetic susceptibility behaviour[10]. The 570cm^{-1} infrared band of La_2PdO_4 decreases in intensity on substitution of La by Na, Sr or Ba.

References

1. BEDNORZ, J. G. AND MULLER, K. A. — *Z Phys B*, 1986, **64**, 189–193.
2. GANGULI, A. K., NANJUNDASWAMY, K. S., SUBBANNA, G. N., RAJUMON, M. K., SARMA, D. D. AND RAO, C. N. R. — *Mod. Phys. Lett. B*, 1988, **2**, 1169–1176.
3. GANGULI, A. K., NANJUNDASWAMY, K. S., SUBBANNA, G. N., UMARJI, A. M., BHAT, S. V. AND RAO, C. N. R. — *Solid St. Commun.*, 1988, **67**, 39–42
4. GANGULI, A. K., SUBBANNA, G. N. AND RAO, C. N. R. — *Physica C*, 1988, **156**, 116–118.
5. GANGULI, A. K., NANJUNDASWAMY, K. S AND RAO, C. N. R. — *Physica C*, 1988, **156**, 788–790.
6. RAO, C. N. R., GANGULI, A. K AND VIJAYARAGHAVAN, R — *Phys. Rev B*, 1989, **40**, 2565–2567.
7. GANGULI, A. K., MANIVANNAN, V., SOOD, A. K AND RAO, C. N. R. — *Appl. Phys. Lett*, 1989, **55**, 2664–2666
8. GANGULI, A. K., RAO, C. N. R., SEQUEIRA, A. AND RAJAGOPAL, H. — *Z Phys B*, 1989, **74**, 215–219
9. GANGULI, A. K., NAGARAJAN, R., RANGA RAO, G., VASANTHACHARYA, N. Y. AND RAO, C. N. R. — *Solid St. Commun.*, 1989, **72**, 195–197.
10. GURU ROW, T. N., GANGULI, A. K., RANGAVITTAL, N., SESHADRI, R. AND RAO, C. N. R. — *J. Solid. St. Chem.*, 1991, **95**, 224–229.

Thesis Abstract (M.Sc. (Engng))

Bilinear constitutive models for bimodulus materials by J. G. Ashoka.
Research supervisor: K. Vijayakumar.
Department: Aerospace Engineering.

1. Introduction

The expanded use of polymers and fiber-reinforced composites in aerospace, hydrospace, and petrochemical industries has stimulated fresh look into the behaviour of these materials under service. One of the

important chartacteristic behaviours of these materials, known as bimodulus materials, when viewed as idealised elastic media is that they often exhibit different mechanical properties under tensile loading than under compressive loading. Proper material modeling is required to enable correct behavioural prediction of components made of such materials. Although several hypotheses have been proposed earlier to formulate consistent constitutive relations[1,2], none of the models based on such hypotheses is firmly established[1]. The present work deals with a critical review of existing constitutive models and embarks on the development of some new constitutive models for isotropic and orthotropic bimodulus materials. For this purpose, the following six criteria have been identified as essential requirements to be satisfied by a consistent constitutive model: (i) Principle of coordinate invariance, (ii) Symmetry of compliance matrix, (iii) Dependency on stress tensor state, (iv) Principle of linear shear response, (v) Principle of continuity in homogeneous media, and (vi) Principle of reduction to classical materials.

2. A general constitutive model for isotropic bimodulus materials

Isotropic bimodulus materials are characterised, apart from axis independency of uniaxial elastic coefficients and coincidence of principal stress planes and principal strain planes, by the feature that the shear modulus in pure shear stress state can be different from shear modulus in pure shear strain condition.

2.1. *Orthotropic materials with isotropic shear response*

To retain isotropic shear response of isotropic bimodulus materials even when the principal stress–strain relations are orthotropic, orthotropic materials with isotropic shear response are first identified by consideration of transformation relations for elastic coefficients of an anisotropic material from one coordinate system to another in terms of multiple angles instead of conventional powers of sines and cosines.

2.2. *A general constitutive model*

After a critical review of existing models, a general constitutive model has been presented satisfying all the six criteria of a consistent constitutive model mentioned earlier. The proposed model is described in biaxial principal stress plane and provides zonewise linear principal stress–strain relations[3]. Elastic coefficients take on different discrete values depending on (i) the signs of principal stresses, (ii) the signs of principal strains, and (iii) the energy ratio greater than or less than unity. The last criterion, believed to be new, is introduced to cater to unequal cross compliances in tension-compression situations and to unequal shear moduli in pure shear stress and pure shear strain states. Rigbi's riddle, namely, the condition of isotropy in a solid is incompatible with the existence of two modulii has been successfully resolved. The model is described by ten zones and needs six independent material constants, of which four correspond to uniaxial compliances and two need to be determined from biaxial tests. Two special models based on the signs of principal stresses and principal strains are derived.

3. A general constitutive model for orthotropic bimodulus material

A general constitutive model is presented satisfying the six criteria of a consistent model. The model proposed is described in material symmetry directions and zonewise linear orthotropic strain–stress relations are maintained. The elastic compliances in the model are dependent on (i) the signs of normal stresses, (ii) the signs of normal strains, and (iii) on the energy ratio greater than or less than unity. The model accounts for four different cross compliances and different direct compliances. The model is described by 12 zones and needs 13 independent compliances. Of these, eight correspond to uniaxial compliances along material symmetry axes, and five need to be determined from biaxial tests. Six special models are derived from the general model by considering one or two of the criteria mentioned above for defining the compliances.

3.1. *Application to composites*

In the literature, limited experimental data are reported for a few composite materials exhibiting bimodular behaviour. The applicability and evaluation of the constitutive models need determination of compliances from experimental data by fitting the data through nonlinear regression analysis. This requires minimisation of a deviation function between the estimated strains and the measured strains, subject to equality

constraints among the compliances due to continuity relations in each model. A nonlinear constrained minimisation process has been carried out by adapting NAG system routine E04UAF which utilizes quasi-Newton method along with estimation of Lagrange multipliers. The strain and stress sign-based model has been applied to the limited experimental data available for Aramid and polyester cord rubbers, graphite epoxy and ATJ-S graphite composite materials

References

1 BERT, C W. AND REDDY, J N. Mechanics of bimodular composite structures. In *Mechanics of composite material—Recent advances* (eds, Hashin, Z. and Herakovich, C T), *Proc. IUTAM Symp*, Aug. 16–19, 1982, pp 325–338.

2. TABADDOR, F. A survey of constitutive equations of bimodulus elastic materials, *Mechanics of bimodulus materials* (ed., Bert, C W.), 1979, ASME, AMD-33, pp 1–15.

3 VIJAYAKUMAR, K. AND ASHOKA, J G A bilinear constitutive model for isotropic bimodulus materials, *J. Engng Mater. Technol., Trans. ASME*, 1990, **112**, 372–379.

Thesis Abstract (M.Sc. (Engng))

Bentonite–kaolinite–sand mixtures as backfill material for nuclear fuel waste disposal vault by H. N. Dwarakanath.
Research supervisors: A. Sridharan and M. Sudhakar Rao.
Department: Civil Engineering.

1. Introduction

The aim of the present investigation is to find a suitable backfill material to be used in underground nuclear fuel waste disposal vaults. The requirement for such backfill material with regard to permeability, shrinkage, compactibility, erodibility, swelling, swelling pressure and compressibility[1] are stringent and contradictory in some cases. Hence, one has to arrive at optimum conditions. In this work an attempt has been made to study known mixtures of bentonite, kaolinite and sand in different proportions to examine their suitability as backfill material. It will be easy to compare the properties of any natural solid with those of known standard mixtures of bentonite, kaolinite and sand and check their suitability.

In the present work, aspects like ground-water contamination and production of toxic radon gas from nuclear fuel waste has been discussed[2]. Also, sites that have been identified as safe in literature for permanent isolation of different levels of nuclear fuel wastes have been discussed in detail.

2. Materials and methods

Bentonite, kaolinite and sand are used as materials in this investigation. The test procedures for determining Atterberg limits, free swell indices, compaction characteristics, swelling and compressibility characteristics have been discussed with regard to bentonite–kaolinite–sand mixtures. Permeability tests were also conducted for some selected mixtures. Pinhole tests were conducted as designed by Sherard *et al* [3] to check the erodibility characteristics of soil mixtures.

3. Results and discussion

It has been found that the index properties of bentonite–kaolinite–sand mixtures such as liquid limit, plastic limit and plasticity index calculated from their individual values are higher than the ones experimentally obtained. The free swell index of the mixtures also behaved in a similar way as the liquid and plastic limits. Shrinkage limit was found to initially increase with the increase in liquid limit/bentonite content up to a certain value after which it was found to decrease with increase in liquid limit/bentonite content.

Correlations have also been obtained between free swell index and liquid limit and free swell index and bentonite content.

Loose bentonite–kaolinite–sand mixtures with bentonite content less than or equal to 10% compress even at a nominal pressure of 6·25 kPa on inundation with water whereas mixtures having bentonite content more than or equal to 15% invariably showed swelling. Time-compression curves were found to be almost linear for lower pressures whereas for higher pressures they were typical 'S' curves of Casagrande's type. The permeability coefficient is found to decrease about 10 folds with decrease in void ratio (the range being 0·6 to 1·6) and increase in bentonite content from 15 to 30%. Attempts have been made to correlate (i) equilibrium void ratios at 6·25 and 400 or 800 kPa, (ii) final void ratio on rebound, and (iii) compression index with liquid limit and/or bentonite content.

There is a good linear correlation between the reciprocal of maximum dry density and optimum moisture content for various mixtures studied. Other published results also show similar behaviour. Attempts have also been made to find the correlations between compaction characteristics such as maximum dry density and optimum moisture content with liquid limit, bentonite content and shrinkage limit. All the points on the wet side of the optimum of the compaction curves of the bentonite–kaolinite–sand mixtures were found to lie between 0 and 4% air voids line

Bentonite–kaolinite–sand mixtures were found to erode as indicated by the pinhole test results and the material eroded was found to be kaolinite (essentially silt-sized fraction). Polyvinyl alchohol (PVA) was found to be an effective additive in binding the soil particles thus preventing them against erosion.

The effect of PVA addition on other engineering properties such as index properties (liquid, plastic and shrinkage limits), free swell index, compaction characteristics, swelling potential and swelling pressure and compressibility have been studied.

4. Conclusions

Based on the results obtained, a mixture of about 20 per cent bentonite, 25 per cent kaolinite and 55 per cent sand could provide an effective backfill material. The influence of kaolinite is marginal and its percentage could be effectively controlled depending upon the availability of silty material. Thus, there is an in-built flexibility in using these materials as constituents of backfill. If the backfill material is likely to be a mixture of bentonite, kaolinite and sand, the results presented in this work would be of great use for suitable selection of a backfill material.

References

1. YONG, R. N., BOONSINSUK, P. AND WONG, G — Formulation of backfill material for a nuclear fuel waste disposal vault, *Can. Geotech. J.*, 1986, **23**, 216–228
2. FANG, H. Y., LUO, G. Y AND CHU, T. G. — Radioactive toxic radon gas and its control methods, *Int. Symp on Environ. Geotechnology*, Lehigh University, Bethlehem 2, 1987, 219–231
3. SHERARD, J. L., DUNNIGAN, L. P. AND DECKER, R. S. — Identification and nature of dispersive soils, *ASCE Geotech. Engng Div*, 1976, **102**(GT4), 287–301.

Thesis Abstract (M.Sc. (Engng))

Holoconnector for single-mode optical fibres: Theoretical analysis and design by Arvind Mathur.
Research supervisor: S. V. Pappu.
Department: Electrical Communication Engineering.

1. Introduction

It is a well-established fact that the information-carrying capacity of a carrier wave increases as its

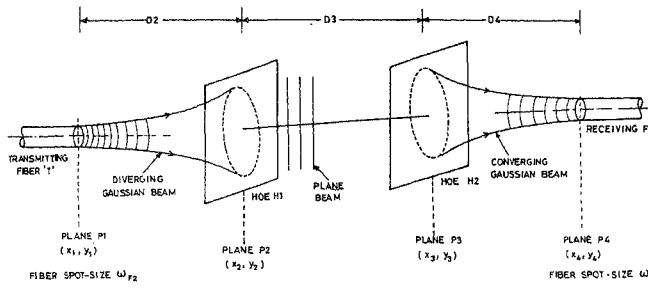

FIG. 1 Schematic of holoconnector.

frequency goes up. That is why lightwave communications have become particularly attractive in the contemporary environment of ever-increasing information traffic, especially during the last decade with the advent of low-loss optical fibers. A vital component of an optical fiber-based communication link is the connector which enables a demountable connection between a pair of optical fibers. For a viable communication link it is essential that the connection be strong, reliable, and as loss free as possible. It is therefore imperative to continually update our knowledge of connector theory and design. This work represents a step in this direction.

Of the many possible approaches for designing connectors, the expanded-beam connector is the most attractive. Holographic approach for the realization of expanded beam connectors offers many advantages[1,2]; for example, low fabrication and replication costs, elimination of specialized jobs like grinding, polishing, etc., required for obtaining high-quality conventional optical elements (COEs); and the multiple, simultaneous, wavefront-transforming capabilities of single holographic optical elements (HOEs). In the past, attempts were made to design holoconnectors[1,3,4], but there exists no systematic study of the first-principles design, in which the nature of the output beam from a chosen fiber is explicitly considered. We have therefore carried out a first-principles analysis of a holoconnector; and the results of the analysis along with a proposed practical design, which constitute the original contribution are presented in this work.

2. Contribution of the thesis

The schematic diagram of a holoconnector for use with single-mode optical fibers is shown in Fig. 1, which essentially consists of two HOEs, H1 and H2, an input (or 'transmitting') fiber T and an output (or receiving) fiber R. The aim is to couple the power radiated by fiber T into fiber R. Fiber T, emitting a diverging Gaussian beam, illuminates H1 which transforms it into a plane wavefront. This plane wavefront propagates in free space until it meets H2, which then transforms the plane wavefront into a converging wavefront on to fiber R. This operation essentially couples the optical field from one fiber to another by using holographic elements for wave-shaping. The recording configurations for H1 and H2 are shown in Fig. 2.

Using the Fresnel-Huygens diffraction formula[5] and the Gaussian approximation[6] for weakly guiding single-mode fibers, expressions for the amplitude transmittance of the HOEs, H1 and H2, recorded using the output radiation of a single-mode fiber and a plane reference beam, have been obtained. The holoconnector set-up has then been analyzed using diffraction theory and expressions for the propagating fields

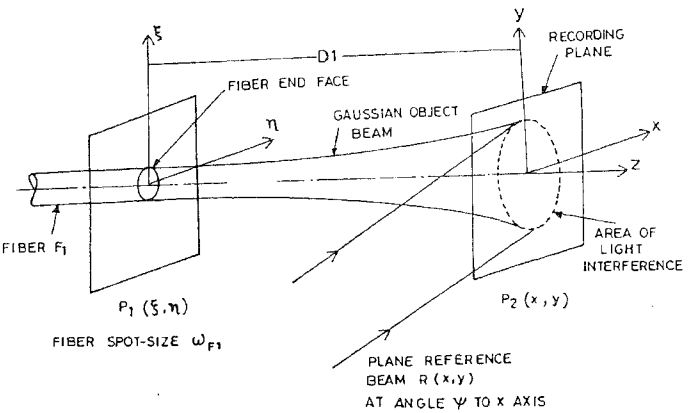

FIG. 2a Schematic of recording geometry for H1

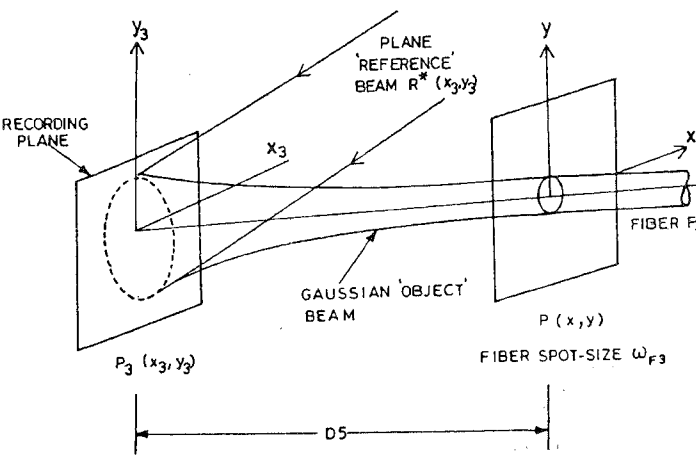

FIG. 2b Recording geometry of H2.

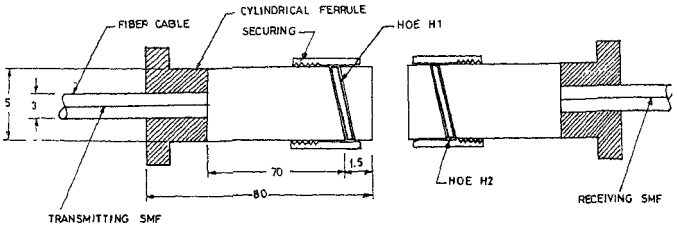

FIG. 3a Ferrule details.

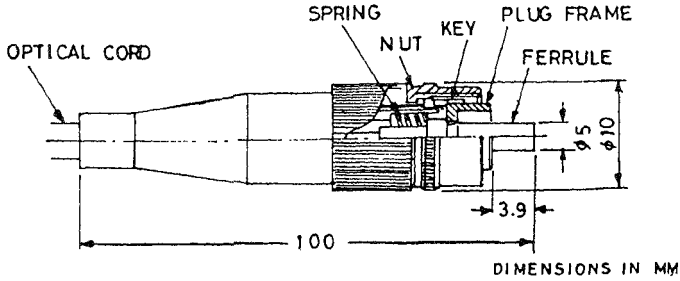

FIG. 3b. Housing plug for the ferrule.

have been obtained at each plane of interest. The central result of our analysis is an expression for the image field, in the plane P4, based on which various characteristics of the holoconnector have been studied.

The salient features of our analysis are the following:

1. The amplitude distribution of the image field in the plane P4 is Gaussian. However, the amplitude distribution is asymmetrical along the two axes of the plane P4 and thus is an elliptic Gaussian rather than a circular Gaussian, as assumed for the output radiation pattern of the single-mode fiber.
2. Using the quadratic and linear phase factors in the image field, coordinates of the image in receiver-fiber plane P4 have been calculated.
3. The variation of the image-plane distance with inter-hologram spacing has been studied graphically and it is shown that in the ideal case the HOEs, H1 and H2, should constitute a sandwich.
4. The focussing action of H2 has been verified graphically by studying the evolution of the Gaussian beam spot size between the planes P3 and P4 of the holoconnector.
5. Using the overlap integral formalism[6], expression for the transmission coefficient for the holoconnector has been obtained. Using this expression, useful equi-efficiency curves have been obtained. It is shown, using some typical values and neglecting the ellipticity of the image field, that a transmission coefficient of 0·75, which corresponds to an insertion loss of about 1·2 dB, can be obtained for the holoconnector.

Using physical and practical considerations a design for the holoconnector has been proposed (Fig. 3).

References

1 NISHIHARA, H , INOHARA, S , SUHARA, T AND KOYAMA, T — Holocoupler: A novel coupler for optical circuits, *IEEE J* , 1975, **QE-11**, 794–796.

2. SOLYMAR, L AND COOKE, D J. — *Volume holography and volume gratings*, 1981, Academic Press.

3 ASH, E. A , SEAFORD, E., SOARES, O AND PENNINGTON, K S — Holographic coupler for integrated optics, *Appl. Phys. Lett* , 1974, **24**, 207–208

4. SOARES, O D D. — Holographic coupler for fiber optics, *Opt Engng*, 1981, **20**, 740–745.

5 GOODMAN, J W — *Introduction to Fourier optics*, 1968, McGraw-Hill

6. MARCUSE, D. — Loss analysis of single-mode fiber splices, *Bell System Tech J.*, 1977, **56**, 703–718

Thesis Abstract (M.Sc. (Engng))

Indentation and low penetration depths by M. R. Sridhar.
Research supervisor: S. K. Biswas.
Department: Mechanical Engineering.

1. Introduction

Past investigations have shown that static indentation hardness of materials decreases with depth of indentation in the first 100μm range and then remain more or less constant with penetration up to a large penetration depth[1]. This is contrary to general expectation for homogeneous and isotropic material where hardness is insensitive to penetration and indentation load. Hardness measurement in this regime (less than 100μm) of penetration is further compounded by the problem that indenter tip is rarely defect free. The defect exists as a curved surface or as tips of large included angles. The defect height in commercially ground indenters comes in the range 1 to 10μm. Hardness measurement in this penetration range is likely to be influenced by the inevitable presence of defects at the indenter tip[2]

An attempt is made here to study the hardness of commercially available rolled lead sheets using conical indenters where tip defects have been engineered in a regulated manner (double cones) A two-dimensional slip line field model[3] of a double wedge has been used to simulate hardness trends observed in conical indentation experiments. An attempt is thereby made to assess mechanical properties of the surface layers of the lead sheet.

2. Experimental

An experimental rig for conducting indentation experiments was designed and fabricated. Indentation is carried out through sudden application of weight on top of an aluminium cylinder which is kept vertical by adjusting tensions in six thin inextensible wires which hold the aluminium cylinder. As the indentation progresses the vertical movement of the cylinder is recorded as a function of time by an LVDT. An exponential curve is fit into the penetration time recording and mean pressure at zero time is obtained. This value is transformed to the more standard form of hardness data where the load gradually increases with penetration[4]. The indenters used are double cones with a fixed secondary cone included angle of 120°. To obtain a range of average indentation strains, the height of this cone was varied. Two primary cones of angle 30 and 60° were used. The experiments were conducted under nominally dry and lubricated conditions.

3. Results and discussion

Experimental mean pressure was found to decrease with penetration up to a critical value beyond which it first increased and then remained unchanged with penetration. Increasing the height of the secondary cone lowered the hardness-penetration characteristics When secondary cone height was increased beyond a certain value, a lift in characteristics was observed. Increasing the primary cone angle had the effect of reducing the penetration at which all the characteristics recorded converge. The effect of lubricating the indenter lead sheet interface was to lower the overall mean pressure levels.

Same trends as above could be obtained qualitatively in the slip line field simulation if the top 20–30μm of the sheet was assumed stronger than the bulk.

Assuming constraint to remain constant at all layers for a given penetration the integrated ($\bar{k}$) shear strength corresponding to a given penetration and angular configuration was estimated from the experimental hardness-penetration characteristics. Known the strains, corresponding to an indenter configuration, $\bar{k}$–strain were obtained and differentiated to yield the stress–strain characteristics of the lead sheets at different depths These stress–strain characteristics were used to estimate the hardness characteristics of another angular configuration under dry and lubricated conditions. A comparison of these estimates with experimental results showed reasonable corroboration.

References

1 CHAKRABARTY, J — *Theory of plasticity*, 1987, McGraw-Hill

2. MOTT, B. W. — *Micro-indentation hardness testing*, 1956, Butterworth's Scientific.

3. PETHICA, J. B , HUTCHINGS, R AND OLIVER, W C — Hardness measurements at penetration depths as small as 20 nm, *Philosopical Mag A*, 1983, **48**, 593–606.

4. TABOR, D. — Indentation hardness and its measurement. Some cautionary comments, *Micro-indentation techniques in material science and engineering* (eds, Blau, P. J and Lawn, B. R), ASTM, 1986, pp 129–159.

Thesis Abstract (M.Sc. (Engng))

Acoustic characterization of porous ceramic tiles by Udayshankar Shirahatti.
Research supervisor: M. L. Munjal.
Department: Mechanical Engineering.

1. Introduction

The performance of an acoustic material depends on the manner in which the acoustic disturbances are propagated in the porous medium. In this connection, two properties of the material, *viz.*, the complex propagation constant (k) and characteristic impedance of medium (Y) prove to be essential for the noise-control engineering purpose[1]. The major emphasis in this work is to determine k and Y and later make use of them for the design of composite acoustic barriers and dissipative ducts. The acoustic material chosen for analysis is a ceramic tile.

These tiles have superior durability against heat, water, wind, moisture and other extreme environmental conditions. They have high mechanical strength because of the porcelain particles that glaze-fuse into a matrix. Furthermore, because the interfaces of the particles are not fully filled up, a large number of irregular continuous pores exist throughout the surface of porcelain board which makes the tile sound absorptive.

The raw material for making ceramic tiles is 'grog' (a mixed grade) available as waste from rejected electrical insulators. The grog is sieved to get the required particle size. The sieved grog is mixed with an

adhesive for green strength and glaze. Later it is fired in a sintering furnace at a specific temperature for a specific time. Normally ceramic tiles are made in thickness of 20 mm

2. Evaluation of normal incidence properties

A model from each of the three approaches, *viz.*, phenomological, microstructural and empirical has been chosen[2-5]. The appropriate parameters for each model have been arrived at by comparing the predicted values of normal incidence absorption coefficient with those observed on a specially designed impedance tube[6]. Incidentally, a flow-resistance-measuring rig[7] has been designed, fabricated and used

Making use of the values of k and Y evaluated by means of the most appropriate of these models, two application areas of industrial noise control, *viz.*, composite barrier and parallel baffle muffler have been analyzed.

3. Analysis of composite acoustic barriers

Making use of the available analytical techniques, general computer programs have been developed for prediction of normal incidence properties of the material (without or with backing airgap), transmission loss of composite barriers, and transmission loss of dissipative ducts and parallel baffle mufflers (without or with airgaps at the back of the acoustic lining). Newton–Raphson method has been used for solution of transcendental equations at various stages, making use of appropriate starting values of the complex roots. This is particularly noteworthy for evaluation of transverse wave numbers for a dissipative duct taking into account the convective effect of mean flow[8].

The predicted values of transmission loss for mufflers are compared with those observed on an experimental set-up designed and fabricated specially for the purpose.

Incidentally, performance curves have been drawn for various applications of ceramic absorbers, *viz.*, closed spaces, acoustic barriers, and parallel baffle mufflers.

4. Conclusions

On the basis of theoretical and experimental investigations reported, the following conclusions can be drawn.

1. The absorption coefficients, as measured using impedance tube, show improvements at low frequencies with increasing thickness of ceramic tile and airgap.
2. The absorption coefficients compared reasonably well with those predicted by means of Beranek's and Attenborough's model.
3. Of the models, namely, Mechel, Beranek and Attenborough, the third seems to be more satisfactory in characterizing the ceramic tile in terms of complex propagation constant k and characteristic impedance Y.
4. Ceramic barriers by themselves may not prove to be useful but composite barriers built by a combination of ceramic tile-airgap-steel show considerable improvements, for industrial noise control applications. Of course, steel could be replaced by any other metal (preferably lead) with equivalent surface density.
5. It has been shown that transmission loss of lined ducts with a uniformly moving medium may be evaluated on computer making use of simple Newton–Raphson method.
6. The experimental and theoretical results on the ducts for TL show considerable differences which would be attributed to flanking transmission and non-local reaction of sound waves with lining wall. For better results, the number and fixing of partition blocks will have to be augmented.
7. The facilities of impedance tube set-up, flow-resistance measurement set-up, and dissipative duct transmission loss set-up, designed and fabricated during this investigation, as also the computer programmes, could be used in future to evaluate acoustic characteristics of any other material.

References

1. ZWIKKER, C AND KOSTEN, C. W — *Sound absorbing materials*, 1949, Elsevier.
2. DELANY, M E AND BAZLEY, E N. — Acoustical properties of fibrous absorbent materials, *Appl. Acoust.*, 1970, **3**, 105–116
3. BERANEK, L. L. — Acoustical properties of homogeneous, isotropic rigid tiles and flexible blankets, *J Acoust. Soc. Am.*, 1947, **19**, 556–568.
4 ATTENBOROUGH, K. — Acoustical characteristics of rigid, fibrous absorbents and granular materials, *J. Acoust. Soc. Am* , 1983, **73**, 785–799.
5 MECHEL, F. P. — Extension to low frequencies of the formulas of Delany and Bazley for absorbing materials (in German), *Acustica*, 1976, **35**, 210–213.
6 PANICKER, V. B AND MUNJAL, M. L. — Impedance tube technology for flow acoustics, *J. Sound Vibr.*, 1981, **77**, 573–577
7. — *Standard test method for airflow resistance of acoustical materials*, ASTM Standard 522–73, 245–251.
8. MUNJAL, M. L — *Acoustics of ducts and mufflers*, 1987, Wiley.
9. VER, I. L — Acoustical design of parallel baffle mufflers, *Proc. Nelson Acoust Conf*, 1981

Thesis Abstract (M.Sc. (Engng))

Ageing characteristics of aluminium–7% silicon–0·3% magnesium casting alloy with cadmium trace addition and iron impurity by S. Murali.
Research supervisors: K. S. Raman and K. S. S. Murthy.
Department: Metallurgy.

1. Introduction

The Al-7Si-0·3Mg alloy is one of the most versatile aluminium casting alloys and has excellent casting characteristics and high strength and moderate ductility in the heat-treated condition. The high strength-to-weight ratio of this alloy has increased its wider application of complex castings replacing many ferrous and non-ferrous materials. Investigation of some of the factors that influence the mechanical properties of the alloy has been carried out The important factors considered are: chemical composition (Mg and Fe), melt quality (degassing, grain refinement and modification), solidification rate and heat-treatment. The commonly occurring problems encountered in shopfloor, that is Mg variation[1,2], Fe impurity and delay in ageing during heat-treatment, have been considered and the influence of some of these factors on mechanical properties of the alloy has been investigated.

Fe impurity is easily picked up during melting and remelting or may already be present in the base alloy itself. Increase in Fe content decreases ultimate tensile strength (UTS), yield strength (YS), ductility[2] and fracture toughness[3]. As per different specifications, Fe impurity is normally allowed up to 0·6%. However, the exact influence of Fe impurity at different levels on the microstructure and mechanical properties of the alloy is not fully understood or reported.

During heat-treatment, the delay occurring between solutionising and artificial ageing decreases hardness and strength while ductility increases and this is termed as 'delayed ageing' or 'room temperature storage'[2,5,6]. Absolute prevention of this delay in ageing is difficult during routine production, as quite often this may result from several non-metallurgical reasons such as power failure, inadequate furnace capacity or equipment breakdown, etc. It has been generally reported that addition of certain trace elements like Cd, In, Sn, and Cu reduces the detrimental effect of delayed ageing on the mechanical properties of the alloys based on Mg_2Si precipitates[5,6].

2. Experimental

To study in detail the effect of these factors, experiments were conducted on the following lines:

(a) Alloys with different Mg (minor element) and Fe (impurity) contents.

(b) Cd trace addition to counter the detrimental effect of delayed ageing.

(c) The casting of alloy in the form of DTD bars in sand and permanent moulds and wedge permanent mould castings with a view to vary solidification rate.

(d) Heat-treatment with different periods of room temperature storage or delay in ageing up to 96 hours.

(e) Determination of mechanical properties: hardness, tensile strength, ductility and dynamic fracture toughness.

(f) Examination of macro-micro structures and fractured surfaces.

3. Results and discussion

The alloy stored at room temperature (delay in ageing) registers a decrease in hardness, UTS, YS while increasing ductility. Addition of Cd trace element has neutralised the detrimental effect of delayed ageing by retaining the hardness and strength with even a marginal increase in ductility. Similar results were observed for low and high Mg alloys.

Increase in Fe content from 0·2 to 0·8% has decreased the UTS, YS and ductility while hardness has increased. Correlation of microstructure and mechanical properties has indicated that the coarse intermetallic compound (β) $FeSiAl_5$ formed during solidification is the cause for reduction in mechanical properties. The anomalous behaviour of increase in hardness and decrease in strength and ductility can be attributed to the increase in work hardening rates at higher Fe levels. Results have also been obtained for different Mg contents, solidification rates (sand and chill castings) and delay periods with Cd trace addition.

Fracture toughness studies at different Mg and Fe contents and solidification rates are also discussed. An analysis of the load-time curve revealed the ductile or brittle behaviour of the alloy. The parameters: total energy absorbed (E_T), dynamic fracture toughness (K_{Id}, K_{Id}, K^*_d), critical flaw size (a_{cr}), ratio $P_{max}P_{gy}$ decreases significantly with increase in Fe content from 0·3 to 0·6 per cent. Stereo photomicrographs of broken Charpy samples of higher Fe content indicate the brittle nature of the alloy and brittle cleavage fracture was also observed at higher Fe contents.

Solidification pattern and soundness of permanent mould wedge casting were studied by obtaining cooling curves, density values and mechanical properties at different positions of the casting.

4. Conclusions

The findings of the investigation are summarised as follows:

1. The alloy is sensitive to Mg content: increase in Mg content from 0·32 to 0·65 per cent has increased hardness and strength while ductility and total energy absorbed in impact test, are significantly reduced by 33 and 50 per cent, respectively.

2. Increase in Fe from 0·2 to 0·8 per cent has decreased ductility by 50 per cent. The total energy absorbed is almost zero at 0·8 per cent Fe indicating the extreme brittleness of the alloy.

3. Chill castings always have better mechanical properties than sand castings at different Mg and Fe contents. During the study of fracture toughness at different solidification rates and Fe levels, higher values of E_T, K_{Id} and a_{cr} were obtained at higher solidification rates.

4. For low and high Mg content alloys stored at room temperature, Cd addition not only retains hardness and strength but improves ductility marginally.

Most of the international and Indian specifications for this alloy indicate a wide range of 0·2 to 0·6 per cent Mg content and Fe impurity up to 0·6 per cent. For obtaining optimum properties of this alloy the delay effect has not at all been taken into account in any of these specifications. The present investigation has clearly shown that the characteristics of the alloy and the properties obtained strongly depend upon Mg content, Fe impurity and delay in ageing and therefore the specifications need re-examination.

References

1. HARRIS, R C., LIPSON, S. AND ROSENTHAL, H — Tensile properties of aluminium–silicon–magnesium alloys and the effect of sodium modification, *Trans. AFS*, 1956, **64**, 470–481.
2. TSUKUDA, M., KOIEE, S. AND ASANO, K. — Effect of pre-ageing at room temperature on mechanical properties of Al–7% Si–Mg casting alloy, *J. Jap. Inst. Light Metals*, 1978, **28**, 531–540.
3. VORREN, O., EVENSON, J. E., PEDERSEN, T B AND ARDAL Og SUNNDAL VERK, A S. — Microstructure and mechanical properties of AlSi(Mg) casting alloys, *Trans. AFS*, 1984, 459–446.
4. COUTURE, A. — Iron in aluminium casting alloys — A literature survey, *AFS Inst. Cast. Metal J.*, Dec. 1981, 9–17.
5. PASHLEY, D.W., RHODES, J W. AND SENDOREK, A. — Delayed ageing in aluminium–magnesium–silicon alloys: Effect on structure and mechanical properties, *J Inst. Metals*, 1966, **94**, 41–49.
6. GHATE, G. P., MURTHY, K. S. S AND RAMAN, K. S — Effect of trace elements on the delayed artificial ageing of Al–7% Si–0·3% Mg alloy, *Aluminium*, 1984, **60**, 18–19.

Thesis Abstract (M.Sc. (Engng))

Lengthening kinetics of plate-like precipitate in Ti–V alloy by R. Goswami.
Research supervisor: M. Mohan Rao.
Department: Metallurgy.

1. Introduction

During solid-state phase transformation, product phase develops various types of morphologies depending on the structure and migrational characteristics of the interphase interface. The plate-like morphology of the second phase has been obtained in many alloys such as Al-Ag[1], Al-Au[2], Ti-Nb[3]. The lengthening kinetics of plate-like precipitate in several alloys has been investigated and there exists a controversy in uniquely describing the lengthening kinetics in terms of diffusion-controlled growth models. The present work explores the lengthening kinetics of the α-plates in Ti–5·9 at % V alloy as a function of time and temperature using quantitative metallographic technique. Transmission electron microscopy has also been used to characterise the nature of the precipitate/matrix interface.

2. Experimental technique

Ti-containing 5·9 at % V after solutionising the alloy at 900°C for one hour was treated isothermally in an inert atmosphere in the two-phase field and subsequently cooled to room temperature. Volume fraction (V_v) and surface area per unit volume (S_v) of the plate-like precipitates were measured using point-counting and line intersection methods, respectively. Thickness and longest length of the plate on the plane of polish were measured using a graduated eye piece which was calibrated at the operating magnification in the optical microscope (Neophot–21). For transmission electron microscopy, specimen was electro thinned by jet polishing technique.

3. Results and discussion

A plate can be modelled as a rectangular parallelopiped neglecting the curve surfaces of the plate-shaped

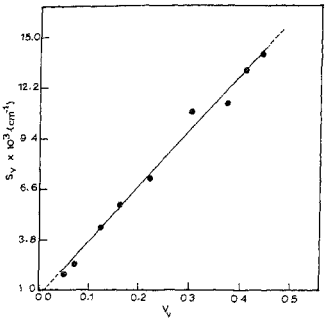

FIG 1a The variation of S_v with V_v at 720°C

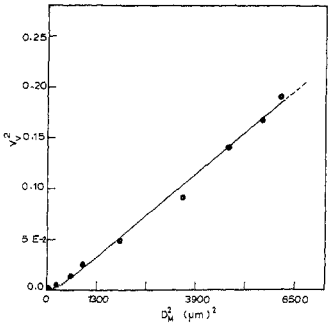

FIG. 1b The dependence of V_V^2 on D_M^2 at 720°C

precipitate The largest dimension (D_M) is obtained when the plane of polish cuts the plate along its body diagonal. The length of the body diagonal can be represented by the following equation

$$D_M^2 = W_M^2 + L_M^2 + \Delta_M^2 \tag{1}$$

where W_M, L_M and Δ_M are the width, length and thickness of the plate, respectively. Subscript M is used to represent maximum values of the dimensions at any time during growth. Since Δ_M is very small compared to W_M and L_M, Δ_M^2 can be neglected in eqn (1)

To determine the lengthening rate, the value of the width is required because the rate of change of D_M cannot represent the lengthening rate of the precipitate To determine the width and also the thickness of the precipitate the following equations have been derived[3].

$$V_V = (\Delta/2)\ S_V \tag{2}$$

$$V_V^2 = (\beta^2 N_V^2 \Delta_M^2 W_M^2) D_M^2 - \beta^2 N_V^2 \Delta_V^2 W_M^4 \tag{3}$$

where N_V is the total number of nuclei per unit volume and β, a constant. Other quantities have been defined earlier.

Figure 1a shows the dependence of S_V of the α-plates on V_V at 720°C A linear behaviour is seen at all reaction temperatures as is to be expected from eqn (2) when Δ is constant The constancy at thickness may probably be due to the soft impingement of the adjacent growing plates. The dependence of volume fraction (V_V) with respect to diagonal length (D_M) of α-plate has been shown in Fig. 1b. Linear relationship between V_V^2 *vs* D_M^2 at all reaction temperatures, except in the early stages of growth at 720°C, is noticed. The deviations from linearity in Fig. 1b in the early stages of growth are attributed to growth in the width and length direction. From the constancy of the width it can be inferred that the further growth of α-plate takes place in the lengthening direction only. The width calculated from V_V^2 *vs* D_M^2 plot was used to calculate the length of the plate.

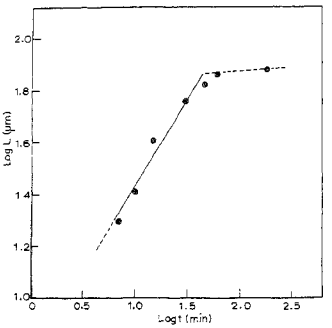

FIG 2 Relationship between ln L_{α} and ln t at 720° C

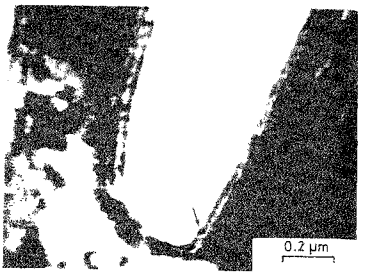

FIG 3 Ledges observed on the edges of α-plate

Table I
Growth exponent at three different temperatures

Temperature (° C)	*Growth exponent (n)*
700	0·8
720	0·7
740	0·60

A generalised growth behaviour ($l \alpha t^n$) has been used to calculate the growth exponent (n) Figure 2 shows a representative log–log plot of length *vs* time. The growth exponent has been calculated from such plots and shown in Table I The variation of growth exponent (n) with temperature cannot be explained either by Zener–Hillert's[4] or Trivedi's[5] model for the growth of plate-like precipitate or by Zener's[6] model for the growth of planar interface. The above models assume an incoherent interface between precipitate and matrix. The structure of the interface has been studied using electron microscopy which reveals the presence of ledges at the tip (Fig 3) of the precipitate The presence of ledges at the precipitate/matrix interface demonstrates that the interface is not disordered. There exist models to explain the ledge-controlled growth behaviour of the second phase. The growth models where ledges have been treated as an independent step cannot explain the experimental results. This may be due to the diffusional field interaction between ledges during growth. Doherty and Cantor[7] have shown the growth exponent changes depending on the ledge spacing (λ) at a fixed supersaturation after the critical time t^*. When λ is equal to ledge height (h), the growth exponent (n) falls to 0·5 whereas if $\lambda > h$ growth exponent increases gradually from 0·5 to 1. Enomoto[8] has given a model for the growth of finite train of steps He has shown that the growth exponent is between 0·5 and 1 up to certain range of time depending on the number of ledges at the interface. Ledge nucleation plays a vital role in controlling the growth of a ledged interface. Information about ledge nucleation is scanty in literature. Thus, it is worthwhile to study ledge nucleation, ledge spacings and height with respect to supersaturation and time to quantify the growth exponent properly

4. Conclusions

From the experimental results it is concluded that kinetics of α plates follows neither parabolic nor linear

growth law. The growth exponent obtained varies from 0·6 to 0·8. The structure of the precipitate matrix interface contains ledges at the interface and ledge mechanism plays an important role in controlling the lengthening kinetics of α-plates.

References

1. LAIRD, C. AND AARONSON, H. I. — The dislocation structures of the broad faces of Widmanstatten plates in an Al-15% Ag alloy, *Acta Met.*, 1967, **15**, 73–103.
2. SANKARAN, R. AND LAIRD, C. — Kinetics of growth of plate-like precipitates, *Acta Met.*, 1979, **22**, 957–969.
3. BHAGWAT, A. W. — *Phase transformation of Ti–7·9 at% Nb alloy*, M.Sc. Thesis, Indian Institute of Science, Bangalore 560 012, India, 1985
4. AARONSON, H. I. — *The proeutectoid ferrite and the proeuctoid cementite reactions. Decomposition of austenite by diffusional process* (V. F. Zackay and H. I. Aaronson, eds), 1962, pp 387–548.
5. TRIVEDI, R — The role of interfacial free energy and interface kinetics during growth of precipitate plates and needles, *Met. Trans.*, 1970, **1**, 921–927
6. ZENER, C. — Theory and growth of spherical precipitates from solid solution, *J. Appl. Phys*, 1949, **20**, 950–953.
7. DOHERTY, R. D. AND CANTOR, B. — Computer modelling of ledge growth kinetics, *Proc. Int. Conf. on Solid-Solid Phase Transformations* (eds, H. I. Aaronson *et al*), 1981, pp 547–553.
8. ENOMOTO, M. — Computer modelling of the growth kinetics of ledged interphase boundaries-II, *Acta Met.*, 1987, **35**, 947–956.